Mixing layers in open channel flow with abrupt bed roughness changes

David A. Vermaas

Wageningen University
M.Sc. student Hydrology and Quantitative Water Management

Supervisors:

Wim S.J. Uijttewaal

Delft University of Technology
Faculty of Civil Engineering and Geosciences
Environmental Fluid Mechanics section

Ton J.F. Hoitink

Wageningen University
Hydrology and Quantitative Water Management group

Content

Image front page: photo of flume with roughness in checkerboard configuration

Abstract

Hydraulic roughness is a key factor in modeling open channel flow. The frictional effects of roughness elements are generally parameterized by a roughness coefficient, representative for the roughness of a grid cell in a model. Bed roughness can be very heterogeneous in practical situations. Especially in floodplains, the roughness height can differ an order of magnitude over a small distance. This roughness heterogeneity impacts the shear stress distribution and the effective friction exerted on the flow. Previous research showed that the effective friction was 20% more than the theoretically weighted average value (Jarquín, 2007) in a flume with a parallel smooth-to-rough bed. Another calculation showed even 80% additional effective friction (Jarquín, 2007; Vermaas et al., 2007). New measurements and a detailed Large Eddy Simulation model described in this report were used to investigate the underlying mixing layer processes and the corresponding development length scales. This may provide the basis to parameterize roughness heterogeneity.

Measurements in a developed flow over a parallel smooth-to-rough bottom show a secondary circulation in vertical planes across the flow. This circulation causes a transverse momentum transport from the smooth to the rough side. The momentum transport by this mechanism has nearly the same order of magnitude as the transverse momentum exchange by turbulent mixing. The transverse momentum exchange enhances the effective friction. An example with a 2D model shows that this can not explain the entire increase in effective friction; additional friction is probably also caused by extra turbulence production near the smooth-to-rough interface, and bed shear stress in the spanwise direction.

In the transition from a uniform flow to a compound flow over parallel roughness lanes, transverse volume transport occurs mainly in the first 4 meter (twice the width of the flume), with a maximum velocity at the start of the parallel roughness section. The development length of the velocity profiles can be scaled to the depth of flow. The vertical profiles outside the mixing layer develop in about 25 times the water depth; the mixing layer at mid depth in about 50 water depths. The secondary circulation was estimated to be fully developed after 80 water depths, but has already a significant momentum transport at half of this distance. Furthermore, the depth averaged transverse mass transport causes a gradient in the advected longitudinal momentum and therefore the water level slope is even more increased above the start of a parallel rough bottom.

As a typical example of repetitive changing roughness, the flow over a roughness pattern resembling an elongated checkerboard pattern was tested. The flow appeared to develop much slower in each section than over a single parallel (infinitely long) roughness. The maximum velocity remains close to the smooth-to-rough interface and no secondary flow is observed in this configuration. Turbulent mixing is neither very effective since the vortices are changing direction not before 1 meter after a roughness change. Nevertheless, the effective friction is seriously increased by this configuration; about 30% additional friction is observed in comparison with a developed parallel flow without transverse interaction. This can be explained by the large adaptation length of the flow relative to the size of the checkerboard fields. The flow velocity is relatively large over the rough fields, and slow over the smooth fields, causing the additional drag.

Samenvatting

Bij het modeleren van oppervlaktewaterstroming is bodemruwheid een bepalende factor. De weerstand door ruwe bodem wordt geïmplementeerd door gebruik te maken van een parameter. Echter, bodemruwheid kan in de praktijk erg heterogeen zijn. Vooral in uiterwaarden kan de ruwheid gemakkelijk een orde van grootte verschillen op relatief korte afstand. Deze heterogeniteit heeft een uitwerking op de schuifspanningen en de effectieve bodemwrijving. Voorafgaand onderzoek toonde aan dat 20% extra bodemwrijving werd gemeten ten opzichte van een theoretisch berekende waarde voor een stroming over een parallel ruwe bodem (Jarquín, 2007). Andere berekeningen lieten zelfs een 80% verhoging zien (Jarquín,2007; Vermaas et al (2007). In dit verslag worden deze resultaten aangevuld met extra laboratoriummetingen en een simulatie (Large Eddy Simulation). Hiermee kan duidelijk worden verschaft over waarde voor de effectieve wrijving, de processen die daaraan ten grondslag liggen en de lengteschalen die gemoeid zijn met (parallelle) heterogene ruwheid.

Metingen in een ontwikkelde stroming over een parallelle ruwheid laat een secondaire stroming zien in een dwarsdoorsnede. Deze stroming brengt een zijdelings impulstransport met zich mee van de gladde naar de ruwe zijde. Dit impulstransport is in dezelfde orde van grootte (iets groter) dan het impulstransport bij directe turbulentie in de menglaag. Het zijdelingse impulstransport heeft weer een extra wrijving tot gevolg. Een simpel 2D model toont aan dit nog niet alle extra effectieve wrijving kan verklaren; waarschijnlijk wordt er nog extra wrijving gegenereerd door turbulentieproductie nabij de parallelle scheiding en door wrijving in transversale richting.

Na de overgang van uniforme naar parallel ruwheid, vind er in de eerste 4 meter (tweemaal de breedte van de goot) zijwaarts massatransport plaats. Dit is maximaal bij de start van de parallelle ruwheid. De lengteschalen behorend bij de aanpassing van de snelheidsprofielen zijn voornamelijk te schalen op de diepte van de stroming. Buiten de menglaag hebben deze profielen ongeveer 25 waterdieptes nodig voor aanpassing; in de menglaag is dit 50 waterdieptes. De secondaire stroming werd rond 80 waterdieptes op volle sterkte geschat, maar heeft halverwege al een significant effect op het zijdelings impulstransport. Daarnaast zorgt het (dieptegemiddeld) zijwaarts massatransport voor een verandering in de impuls die in de stroomrichting wordt geadvecteerd. Een extra verhoging van het verhang in het wateroppervlak is het gevolg.

Ook is de stroming bekeken over een ruwheid in een uitgerekt schaakbordpatroon, als een kenmerkend voorbeeld van herhalende ruwheidsveranderingen. De stroming blijkt zich in dit geval veel langzamer aan te passen (in een schakel) dan over een (oneindig lange) parallelle ruwheid. De maximale snelheid blijft dicht bij de parallelle ruwheidsscheiding en geen secondaire stroming is waargenomen. Het impulstransport door turbulente menging blijft ook zeer beperkt omdat de menglaagwervels pas 1 meter na de ruwheidsverandering van richting zijn veranderd. Desalniettemin is de effectieve wrijving met 30% verhoogd ten opzichte van een theoretische waarde gebaseerd op individuele ruwheden. De combinatie van seriële en parallelle ruwheidsveranderingen blijken daarmee een belangrijke invloed te hebben op de effectieve wrijving. Dit moet bij modelering van stromingen over heterogene ruwe bodems in aanmerking worden genomen.

Acknowledgement

For this research I am indebted to several people.

First of all, I want to thank the technical staff of the Fluid Mechanics Laboratory of the TU Delft. Especially the help of Sander de Vree, his tips and allowing me to work until the late afternoon, was greatly appreciated.

Furthermore, thanks Wim van Balen for the help with the Large Eddy Simulation and allowing me on this private computing cluster.

Next, the help of Arjan Sieben (acting in behalf of Rijkswaterstaat – RIZA) is kindly appreciated. His ideas and additions for the planning were useful and motivating. Next to that, I am greatly thankful for the financial support of Rijkswaterstaat.

Finally, I am very thankful to my supervisors, Wim Uijttewaal and Ton Hoitink, for their support and comments. The help and discussions with Wim were really motivating and made it a good time for me at the TU Delft.

Introduction

Estimating flood risks for rivers is a hot topic in densely populated areas such as the Netherlands. Due to a constantly changing urban landscape and limited measurements, the conveyance capacity (for a given water level) can only be modelled. In order to evaluate accurately river flood risks, the (effective) bed friction must be known. While pipe flows can be considered often as flow over a hydraulically smooth wall, open channel flow nearly always deals with rough bottoms. As a result, the flow is subject to increased bottom friction and (as the roughness elements are protruding the viscous sublayer) form drag. To apply the smooth wall theories (for example the law of the wall) for a rough environment, roughness parameter are introduced. Several parameters are in use; most common are the Chézy parameter (C), Nikuradse roughness height (k_s) and the Darcy friction factor (f).

Friction parameters for main channels can be inferred from velocity or water level data. Alternatively, when no detailed measurements are available (such as for floodplains), the friction parameters can be estimated based on the bed composition. However, the roughness elements differ in size and spacing and therefore the roughness must be considered to be heterogeneous. Especially floodplains feature large spatial differences in roughness elements and thus in friction parameters. The interactive effects between roughness patches are relatively unknown, but can be crucial for the effective bottom friction and thus the conveyance capacity. Also the shear stress distribution is strongly affected by the heterogeneity of the bottom roughness, which can be important for erosion and sedimentation in areas with heterogeneous bed roughness.

An idealised example of heterogeneous roughness is a bed with an abrupt serial or parallel roughness change. Preliminary research showed that parallel bed roughness caused a 20% increase in friction factor with respect to a weighted average value (Jarquín, 2007). The 20%-value was disputable since Jarquín also showed that the heterogeneous roughness caused 35-45% reduction of conveyance capacity, caused by an increase in the effective friction factor over over 80%. This was confirmed by Vermaas et al (2007). This study can give certainty about the effective friction factor for a parallel rough bed.

Besides quantitative results, more information about the physical processes in the mixing layer is needed. Earlier studies report observations of a secondary circulation due to heterogeneous roughness (e.g. Studerus, 1982; Hinze, 1967). However these studies were useful, some questions remain unanswered. The previous studies consider mostly equilibrium conditions; the length scales of adaptation to these conditions are not yet known. Furthermore, the dominant mechanism responsible for momentum exchange between rough and smooth parts is in discussion; i.e. whether a secondary circulation or horizontal vortices drive the exchange. To answer these questions, this study focuses on the region close to an abrupt roughness change.

The results of this study are particularly of great value for floodplain flow. Because of the patched vegetation, floodplains often consist of a highly irregular surface, resulting in a heterogeneous roughness field. Moreover, measurements in floodplains are sparse (as the shallowness makes boat measurements impossible), which makes this research extra useful for flow estimates in floodplains.

Problem definition

This study was initiated to investigate the effects of heterogeneous roughness. To achieve useful results within a limited time, this study was confined to the situation of parallel roughness changes (for developed as well undeveloped flow) and iteratively repeating parallel roughness sections. Three goals can be defined for this research:

- Further analysis on a representative value for an effective friction parameter in a parallel rough setting. Some indistinctness was found in the results for the effective friction factor (either 20% or over 80% increase due to heterogeneity). To determine a representative effective friction factor, an overview of the differences in calculation method and extra measurements (where needed) are required.

- Investigating the flow structures involved in the mixing layer. Very few flow mixing layer vortices were seen in the mixing layer during the former experiment and the transverse profiles of shear stress are different than seen in other mixing layers (for example Uijttewaal & Booij, 2000). Therefore the transverse momentum exchange in the mixing layer has special attention. A secondary circulation could play a role in this field.

- Determination of characteristic length scales in which the flow is adapting to a parallel bed roughness situation. These scales are already investigated in case of sudden roughness changes over the full width (i.e. serial roughness changes, for example by Nezu & Nakagawa, 1991), but are unclear in case of parallel roughness lanes. The investigation encloses development length scales for the velocity profiles within and out of the mixing layer, turbulent stresses and possibly the development of a secondary circulation.

To achieve these goals, new experimental data will be gathered to complement the present data of Jarquín (2007). For an understanding of the mixing layer processes, high resolution 3D velocity measurements are required in the mixing layer. Therefore the area of the (developing) mixing layer was most intensively measured.

Next to that, an imitation of this experiment by using a model can show even more spatial details. The descriptions of the experiments and this model can be found in chapter 2. The results of the three bed configurations can be found in chapters 3, 4 and 5. Chapter 6 finalizes this report with conclusions.

1) Theory

Bottom roughness

Bottom friction and the associated properties of the boundary layer are basic principles in fluid dynamics, actually caused by the adhesion of water to a fixed wall and the viscosity of water. One can also intuitively depict that rough and irregular bottoms cause more friction to a flow. The physical principle for this phenomenon is the enlarged contact surface and, more importantly, the bottom level perturbations.

Several empirical relationships have been proposed to describe the bottom friction by using the surface slope and one empirical parameter; for example the Chézy, Manning and Darcy-Weisbach equations, each with their own parameter. The Darcy-Weisbach equation reads (Douglas et al, p.517):

$$Q = A \cdot \sqrt{\frac{8 \cdot S \cdot R \cdot g}{f}}$$
(equation 1)

In which

> Q is the discharge
> A is the cross sectional area
> S is the water level slope
> R is the hydraulic radius
> g is the gravitational constant (9.8 m/s^2)
> f is the Darcy friction factor (= 4 · Fanning friction factor)

The most direct way to derive a value for the friction factor is by using water level and discharge data. Alternatively, the friction factor can be calculated based on the size of the roughness elements, expressed in a Nikuradse roughness height k_s. A common formula for this calculation is the Colebrook-White equation (Douglas et al, p.358), assuming a fully developed flow:

$$\frac{1}{\sqrt{f}} = -2 \cdot \log_{10}\left(\frac{k_s}{14.83 \cdot R} + \frac{2.52}{Re\sqrt{f}}\right)$$
(equation 2)

In which

> k_s is the Nikuradse roughness height
> Re is the Reynolds number (=velocity·length/kinematic viscosity)

The parameter k_s is an effective value since the grain size is never uniform in practice. The only issue remaining is that (heterogeneous) roughness elements must be translated into one value for the Nikuradse roughness height. Different relations were found in previous researches. Camanen et al (2006) reported (based on a series of previous researches) the relation $k_s = 2 \cdot d_{90}$ or alternatively $k_s = 2.5 \cdot d_{50}$ for a fixed bed, for grains up to 4 cm. The rough bed in this experiment can be considered to be fixed. Bray (1982) has listed more

results for gravel and sand beds; varying from $2 \cdot d_{90}$ to $3.5 \cdot d_{90}$. Initially, the k_s was set to twice the d_{90}-value. According to the distribution of the roughness elements used in this experiment (figure 1, $d_{90} = 8.8mm$), this leads to a value of $k_s = 0.019$. This value was initially used in the Large Eddy Simulation of the experiment.
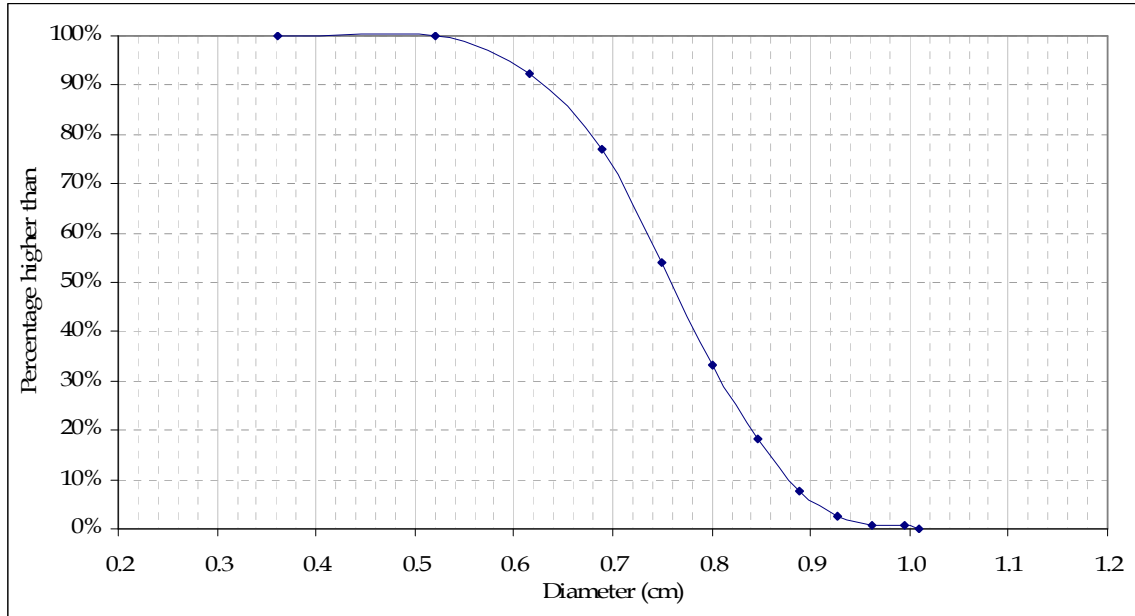

Figure 1: Roughness element grading curve, from Jarquín (2007). The same roughness elements were used in this research. From this curve reads $d_{50} = 7.6mm$, $d_{90} = 8.8mm$.

By using equations 1 or 2, an overall friction factor can be derived. The local friction can be described by the (local) bed shear stress. The bed shear stress, and thus a friction parameter, can be inferred from a vertical turbulent shear stress profile of a uniform flow. This reads according to the theory (Nieuwstadt, 1998, p.63):

$$\tau = \rho \cdot \overline{u'w'} = c_f \cdot \overline{U}^2 \cdot \left(1 - \frac{z}{h}\right)$$

(equation 3)

In which

τ is the local shear stress
ρ is the density of water
c_f is the friction coefficient, equal to $1/8 \cdot f$ for uniform flow
z is the vertical coordinate
h is the total water depth
$\overline{U}$ is the depth and time averaged horizontal velocity (in x-direction)
$\overline{u'w'}$ is the covariance of the velocities u and w

The bed shear stress can now be obtained by linearly extrapolating the shear stress profile to the bottom.

By definition, the x, y and z coordinates are defined respectively towards downstream, left and upward direction. The velocities corresponding to these directions are called respectively u, v and w.

Another possibility is to infer the bed shear stress from fitting a logarithmic vertical profile (Nieuwstadt, 1998, p.73) to the mean velocity data, resulting in a value for the friction velocity u*:

$$u = u * \cdot \left[\frac{1}{\kappa} \cdot \ln\left(\frac{z \cdot u *}{\nu} \right) + 5 \right] \qquad \text{(smooth walls, equation 4)}$$

$$u = u * \cdot \left[\frac{1}{\kappa} \cdot \ln\left(\frac{z}{k_s} \right) + 8.5 \right] \qquad \text{(rough walls, equation 5)}$$

In which

u is the horizontal velocity (in x-direction)
κ is the Von Kármán constant (=0.41)
ν is the kinematic viscosity

The friction velocity is again related by definition (Nieuwstadt, 1998, p.63) to the bed stress according to:

$$u* = \sqrt{\tau_b / \rho} \qquad \text{(equation 6)}$$

In which τ_b is the bed shear stress.

Serial roughness changes

A serial roughness change is defined here as an abrupt change in bed roughness in longitudinal direction, over the full width of the channel. Neglecting the effects due to adaptation to a new flow regime, the effective friction factor could be represented by a (arithmetic) average of the individual friction factors, i.e.:

$$f_{eff} = \frac{f_{smooth} + f_{rough}}{2} \qquad \text{(equation 7)}[1]$$

Several researches have been done for the flow with a serial roughness change, among others by Nezu & Nakagawa (1991), Antonia & Luxton (1971, 1972) and Jarquín (2007). A smooth-to-rough change causes an overshoot in bed shear stress due to the streamwise advection of water with a relative high velocity close to the bottom. A characteristic length scale to adapt to the rough bed is about 20 water depths (Nezu & Nakagawa, 1991; Antonia & Luxton, 1971) and even larger for the full development of the inner boundary layer height.

---

[1] The equivalent formula for the Chezy parameter C ($= \frac{8g}{f}$) reads: $\frac{2}{C_{eff}^2} = \frac{1}{C_{smooth}^2} + \frac{1}{C_{rough}^2}$

For the rough-to-smooth transition, studies are divided about the length scale for adjustment to the new surface conditions. For example, Bradley (1965, according to Antonia & Luxton (1972)) and Antonia & Luxton (1972) report a longer length of adaptation than in case of a smooth-to-rough change; but contrary to this results are those of Nezu & Nakagawa (1991) and Makita (1968, according to Antonia & Luxton (1972)), who claim a similar longitudinal distance as in the smooth-to-rough transition for the development of the linear shear stress profiles. More harmonizing is the sequence of under- and overshoots of bed shear stress after a rough-to-smooth transition; this results on average in a higher bed shear stress than in a self-preserving situation over a full smooth bed.

In conclusion, a serial change in bed roughness gives cause to extra friction in comparison to the arithmetic mean friction factor calculated by equation 7. This extra friction for an isolated serial roughness change will not be quantified since this was not among the highest priorities of this research. A combination of serial and parallel roughness changes is involved in the current experiment.

Parallel roughness changes

In channels with parallel roughness, most research was focused on compound channels. This situation has a practical application in the sense of a relative smooth main channel in combination with a relative rough floodplain. A large well known data set in this study field was obtained in the Flood Channel Facility (FCF), where among others the differences between smooth and rough floodplain banks were investigated (Knight & Brown, 2001; Myers et al, 2001). A secondary circulation can be observed in this compound channel flow, described by Tominaga & Nezu (1991a) and well modelled by Sofialidis & Prinos (1999); see figure *2*. This secondary circulation, in combination with turbulent stresses, has a momentum transfer from the main channel to the floodplain as a consequence. Research of Smart (1992) showed that the momentum exchange between main channel and floodplain resulted in a increase in water depth in the order of 15%.
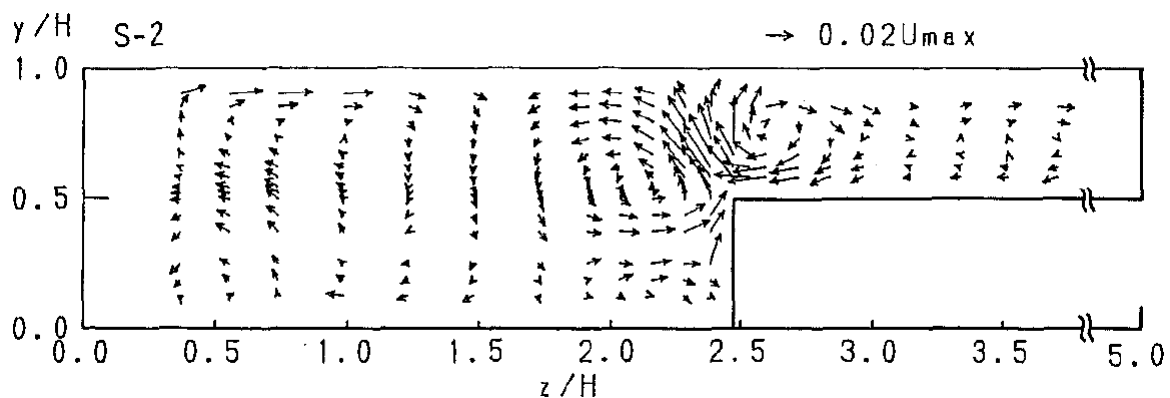

Figure 2: Velocity vectors in a cross sectional plane in a compound channel. From: Tominaga & Nezu (1991a).

These researches were very useful for improving modelling of flow in rivers with rougher floodplains aside. However, this is not applicable to the effect of heterogeneous roughness within a floodplain (where the depth of each section is about equal). The effect of heterogeneous roughness in flow with equally deep sections is much less well known.

Some studies to the net effect of parallel roughness in a flow with uniform depth are done by Taylor (1961), Studerus (1982) and Jarquín (2007), but questions still remain.

Taylor (1961) proposed a simple arithmetic mean of the individual friction factors to calculate the effective total friction factor; i.e. according to equation 7. One could easily see that this can not be valid for large roughness differences; the effective friction factor would become in that case, according to equation 7, half of the individual rough friction factor. This is not realistic. A more physical approach is to assume a parallel flow, i.e. the total discharge is composed of two individual discharges (figure 3, left panel). In that case, the effective friction factor could be calculated by (Jarquín, 2007; analogue to the parallel approach in Sieben, 2006):

$$\frac{2}{\sqrt{f_{eff}}} = \frac{1}{\sqrt{f_{rough}}} + \frac{1}{\sqrt{f_{smooth}}}$$

(equation 8)[2]

An important assumption for this equation is neglecting momentum exchange between the flow over respectively smooth and rough sections. Momentum exchange is inevitable in reality, and results in a smooth transverse profile of the longitudinal velocity. The area under influence of this transverse momentum exchange is referred as the mixing layer. Figure 3 (right panel) shows a possible mixing layer proposed by Jarquín (2007). The net effect on the bed friction, just as the development length of the mixing layer, has a practical interest and is a main topic of this study.

A special property of flow over parallel roughness is investigated much more intensive: secondary circulation (e.g. Studerus, 1982; Tominaga & Nezu, 1991b; Wang & Cheng, 2006). A secondary circulation appears to play a role in the momentum exchange between a parallel smooth and rough section. The next paragraph is dedicated to this subject.
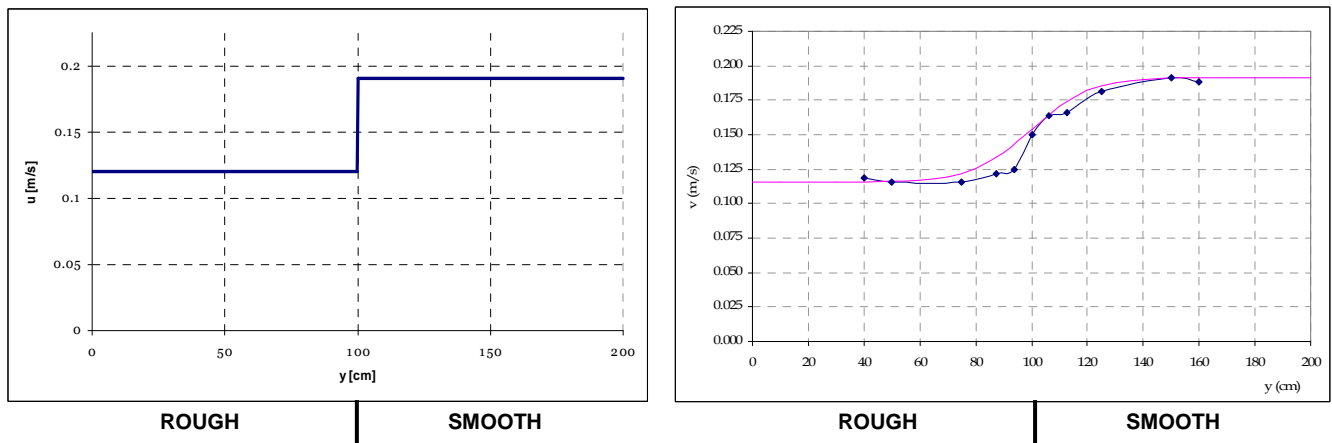

Figure 3: Transverse profiles of longitudinal velocity over a parallel rough bed. Left panel: step profile, apparent if no momentum is exchanged in transverse direction. Right panel: profile as measured by Jarquín (2007), with a fitted tanh-function.

---

[2] The equivalent formula for the Chezy parameter C ($= 8g/f$) reads: $C_{eff} = \left(C_{smooth} + C_{rough}\right)/2$

Secondary circulation

Secondary currents are currents perpendicular to the main flow, such that they do not contribute to (depth averaged) net horizontal transport. A well-known secondary flow occurs in curved channels due to the centrifugal forces and bed friction. These currents are known as the secondary currents of Prandtl's first kind (Nezu & Nakagawa, 1993, p.85). Next to that, secondary circulation can occur due to heterogeneity and anisotropy of turbulence. This circulation is referred as secondary currents of Prandtl's second kind (Nezu & Nakagawa, 1993, p.85).

As already mentioned, a secondary circulation above a parallel rough bottom is observed in several studies, first described in detail by Studerus (1982). Figure 4 shows velocity fields in a cross section of a straight flow, found by Studerus (1982) and by Wang & Cheng (2006). This circulation appears to have a downward component above the rough side and an upward component above the smooth side. A consequence of this circulation is that momentum is transported from the smooth to the rough side, assuming an increasing longitudinal velocity with height. Studerus (1982) suggests that this advection of streamwise momentum is more efficient than turbulent mixing and has a stronger contribution in a higher relative roughness. However, no measurements validate this hypothesis.
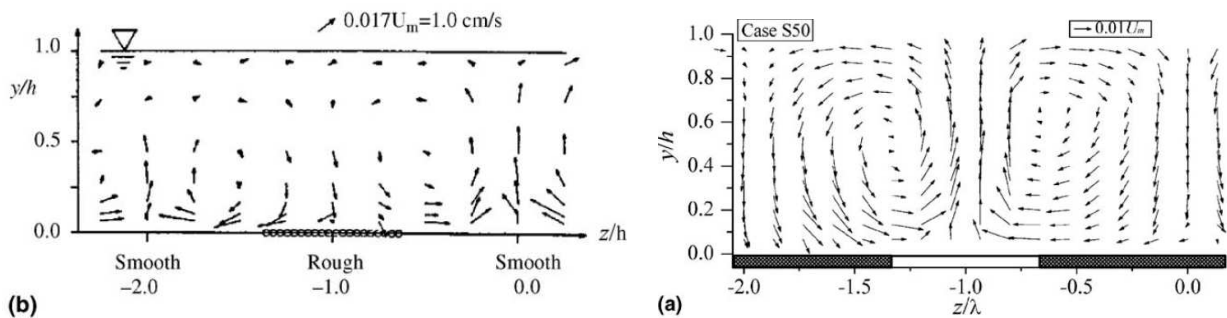

Figure 4: Secondary circulation due to parallel roughness heterogeneity as observed by Studerus (1982) in the left panel and by Wang & Cheng (2006) at the right panel.

The generation of the secondary circulation is often linked to a balance equation for streamwise vorticity, assuming uniformity in longitudinal direction (Nezu & Nakagawa, 1993). Anisotropy in turbulence would lead, according to this equation, to an advection of vorticity. However, once the circulation is developed, no advection of vorticity is apparent anymore. Furthermore, for the start of a parallel rough flow, this equation can not be used since the flow is not uniform in longitudinal direction.

A better way to describe the secondary currents of Prandtl's second kind is to analyze the turbulence energy balance (Hinze, 1967). The local, steady-state balance of the turbulent kinetic energy (TKE) budgets can be considered as:

advection + diffusion =

       production - direct viscous dissipation - transfer through the energy cascade

Measurements in pipe flows (Laufer (1954) according to Hinze (1967)) showed that the terms concerning diffusive TKE transport and direct viscous dissipation are relatively

small and can therefore be neglected. Secondly, since a fully developed mixing layer is uniform in x-direction, the $\partial/\partial x$ terms can also be neglected. These assumptions lead to a simplified equation of this turbulence energy budget:

$$\overline{v} \cdot \frac{\partial k}{\partial y} + \overline{w} \cdot \frac{\partial k}{\partial z} = -\overline{u' \cdot v'} \frac{\partial \overline{u}}{\partial y} - \overline{u' \cdot w'} \frac{\partial \overline{u}}{\partial z} - \varepsilon \qquad \text{(equation 9)}$$

in which ε is the energy dissipation through the energy cascade and k is the turbulent kinetic energy, defined as:

$$k = \frac{1}{2} \cdot \left(\overline{u'^2} + \overline{v'^2} + \overline{w'^2} \right) \qquad \text{(equation 10)}$$

The left-hand side of equation 9 represents the advection of TKE; the right-hand side shows the difference between production and dissipation of turbulent energy. At the rough side of a parallel smooth-rough interface, turbulence production exceeds the dissipation; resulting in a positive value at the right hand side of equation 9. By making some additional obvious assumptions, the direction of the secondary circulation can be inferred.

First it can be assumed that in general:

$$\left| \frac{\partial k}{\partial z} \right| >> \left| \frac{\partial k}{\partial y} \right|$$

Moreover $\overline{v}$ and $\overline{w}$ are of the same order of magnitude, then it follows that

$$\overline{w} \cdot \frac{\partial k}{\partial z} > 0$$

Then, since the free surface dampens turbulence, it can be concluded that

$$\frac{\partial k}{\partial z} < 0$$

Combining these last two statements, it implies that $\overline{w} < 0$ above the rough side of the interface and in a similar way $\overline{w} > 0$ above the smooth side. This is qualitatively in accordance with the secondary circulation as shown in figure 4.

Provided that the secondary circulations have small amplitudes and develop slowly (like boundary layers do), long distances can be expected for a fully developed flow. The length scales for developing the secondary circulation are unknown so far. A dense grid in cross sections at several streamwise positions is required to investigate the development of the secondary circulation.

2)   Experimental setup

To achieve the research goals as explained in the problem definition, laboratory experiments are executed. To isolate the effects of roughness changes, the bed should be divided into two regions with a distinct composition (resp. smooth and rough), using an abrupt change.

A requirement to the flume for a developed flow situation is a large flume length with uniform conditions in streamwise direction. Furthermore, the width of the flume must be large in order to obtain a flow situation without influence of the mixing layer or side walls. Both lengths are expected to be scaled on the depth of the flow.

Velocity and water level measurements are needed for deriving effective friction and mixing layer processes. General requirements for the associated instruments are a high precision and mobility. Several gauges were used for the water level measurements, amongst others an electronic gauge. An Acoustic Doppler Velocimeter (ADV) was mainly used for the velocity measurements, since this instrument meets the requirement of fairly accurate, high frequent and 3D sampling. Since the ADV was not able to measure the upper 4 cm of the water column, Particle Tracking Velocimetry (PTV) was supplemented to measure the velocity at the water surface. Combining these velocity measurements and using a fine measurement grid, the processes in the (developing) mixing layer can be analysed. For an even more detailed velocity field, a high-grade model would be a useful tool. A Large Eddy Simulation (LES) is used for this purpose, by mimicking the experimental conditions.

All these experimental tools and settings will be described below.

Flume geometry

The flume used for the laboratory experiments counts 2 meters in width and almost 30 meter in length. The inlet is provided with straight pipes and a foam plate to homogenise the flow and reduce waves.

In the first configuration, the bottom of the flume is initially smooth (by using wooden plates) and after several meters split in two parallel sections; the right side is covered with stones (to represent a rough part) and the left side is covered by a 6 mm wooden plate (polished, to act hydraulically smooth). Figure 5 illustrates the used configuration. The start of the rough part was moved once (referred as configuration 1a and 1b in figure 5) to cover a larger measurement range since the measurement carriage could only move over 10 meters.
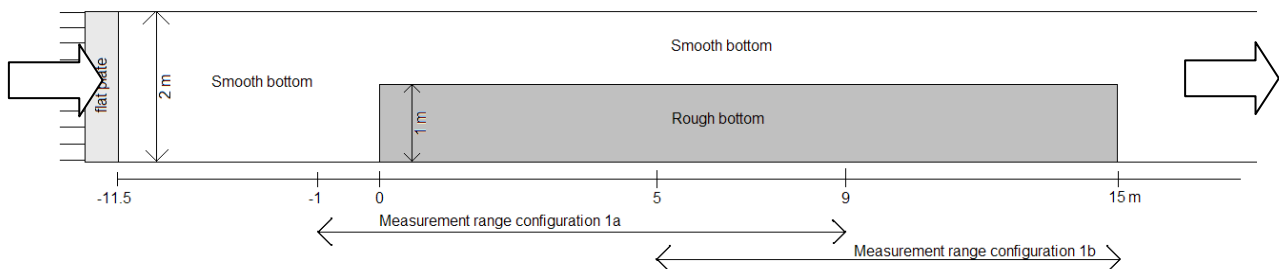

Figure 5: Top view of experiment setup in first configuration. As the instrument could not move along the whole flume length, the bottom setup was moved once over the length of the flume. The resulting measurement ranges are indicated by respectively configurations 1a and 1b.

10

In the second configuration, the rough bed is established alternately at the right and left side of the flume; i.e. the smooth and rough patches form an elongated checkerboard. The length of each patch was 4 meter. See figure 6 for the illustration. The sections were chosen 4 meter long because the flow (in cases of 8cm and deeper) appeared to be only partly developed at this length in the first configuration and the LES model. Therefore the flow in this configuration is dependent on (at least) two previous checkerboard sections, which distinguishes this flow from a developing parallel flow.
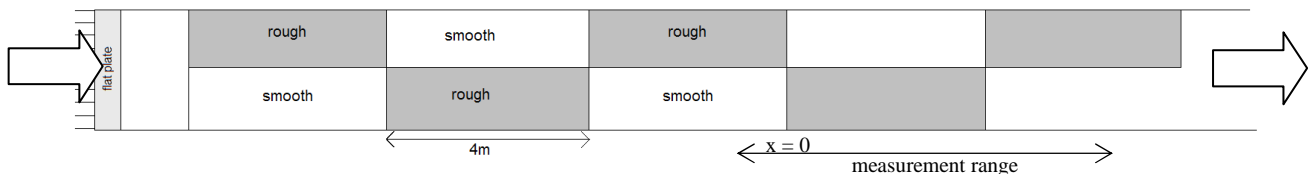
Figure 6: top view of experiment setup in checkerboard configuration.

The side walls at the measurement range are made from Perspex and can be considered hydraulically smooth. The seams are filled with glue; just as the seams in between the wooden plates. The flume ends with a sediment trap and an adjustable weir.

The following instruments were used for the measurements:

- Acoustic Doppler Velocimeter (ADV)
- Particle tracking velocity method (PTV)
- Electronic gauge
- Manual gauge
- Acoustic discharge measurement device

The use of these instruments will be briefly explained.

Water level gauges

Two types of gauges are used: manual gauges and an electronic gauge.

The manual gauges were installed at the mobile carriage and a fixed one at the beginning of the smooth-rough lanes. The manual gauge can be read to 0.1 mm accurate and are used, next to the electronic gauge, for measuring the water level slopes.

The electronic gauge measures the water level based on the conductivity between two vertical rods; the higher the water level, the higher the conductivity. This method is insensitive to water adhesion (as it measures the water level in between the rods) and because the data is saved digital, (non-standing) waves can be filtered out easily by averaging.

The electronic gauge was installed at the same mobile carriage as the ADV was installed, above the rough lane, 25 cm from the wall. The type of electronic gauge was a GHM Wave Height Meter from WL Delft, used in combination with an amplifier (+/- 10V) and A/D converter. The data was saved in DasyLab at 50 Hz.

The water level measurements were done in streamwise direction over 9 meters. One measurement series is done in transverse direction (over 1.5 m). All water level measurements are taken with respect to the movable carriage and afterwards corrected for the level course of the carriage itself. This correction was made based on the water levels of still water. The correction magnitude is in the order of 0.2 mm.

All measurements are done at least twice, in opposite directions, to cancel out possible small, long term fluctuations (see later on). The difference between the duplo measurements is about 0.10mm for the manual gauge and usually 0.025mm for the electronic gauge; some smaller for the still water measurements and some larger for the 100lps cases (ca. 0.15mm for the manual and 0.08mm for the electronic gauge). Because the electronic gauge has more consequent values, these results are mainly used in this report. The slopes of the manual gauge are very similar.

Acoustic discharge measurement device

The discharge was measured by an acoustic device mounted at the inlet pipe. The device measures the velocity in between two rings mounted around the pipe by sending a sound to and fro. Knowing the pipe area, the discharge can be calculated. The instrument has (according to the manufacturer) a 1% systematic error, but the error was increased by small portions of air left in the pipe (resulting in 3% extra discharge compared to another acoustic device, this one in a vertical pipe). Therefore the absolute discharge may have a 3% overestimation, but since the same device is used for all measurements, this is not inconvenient.

Acoustic Doppler Velocimeter (ADV)

An ADV makes use of the Doppler effect to measure a flow velocity in a small volume. A central transmitter emits a short sound pulse, which is scattered by particles in the water and receives by receivers (called beams) in four different directions, see figure 7. Three beams are actually enough to calculate the velocity in three dimensions; the fourth one can be used as a validation for the velocity data. Using four beams, the velocities in a Cartesian coordinate system relative to the instrument can be calculated by:

$$v_x = \frac{v_1 - v_2}{2 \cdot \sin(\theta/2)} \qquad v_z = \frac{v_1 + v_2}{2 \cdot \cos(\theta/2)}$$

$$v_y = \frac{v_3 - v_4}{2 \cdot \sin(\theta/2)} \qquad v_{error} = \frac{(v_3 + v_4) - (v_1 + v_2)}{4 \cdot \cos(\theta/2)}$$

(equation 11)

In which

v_x, v_y and v_z are velocities in Cartesian coordinates relative to the ADV,
v_{error} is a measure to validate the velocity data (should be close to 0),
θ is the geometrical beam angle,
v_1, v_2, v_3 and v_4 are beam velocities (of resp. beam 1,2,3 and 4)
This can be done in a vector calculation, using the transformation matrix M, by:

$$
\begin{bmatrix} v_x \\ v_y \\ v_z \\ v_{error} \end{bmatrix} = M \cdot \begin{bmatrix} v_1 \\ v_2 \\ v_3 \\ v_4 \end{bmatrix}
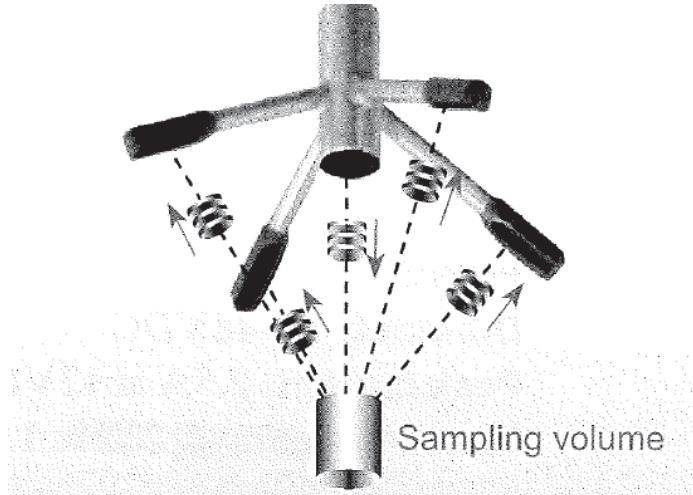\qquad\qquad \text{(equation 12)}
$$

Figure 7: working of an ADV. A pulse is emitted from the centre, reflects to scatterers in the sampling volume and is received in four directions. The measured velocity is in the direction of half the geometrical beam angle (i.e. 15º for a 30º beam angle). Velocities in a Cartesian coordinate system can be obtained by combining the beam velocities.

The ADV used in this experiment was manufactured by Nortek, type Vectrino, with a flexible stem. The ADV was mounted ca. 30º to the vertical axis (figure 10, left panel). This angle was chosen as a compromise between a large depth range and a low side lobe distortion. For a large angle to the vertical, the ADV can measure closer to the surface but the signal is harmed in a larger depth range by reflections of side lobes to the bottom. These reflections cannot be distinguished from the true signal as the echo time can be exactly the same as to the measurement volume, see figure 8.
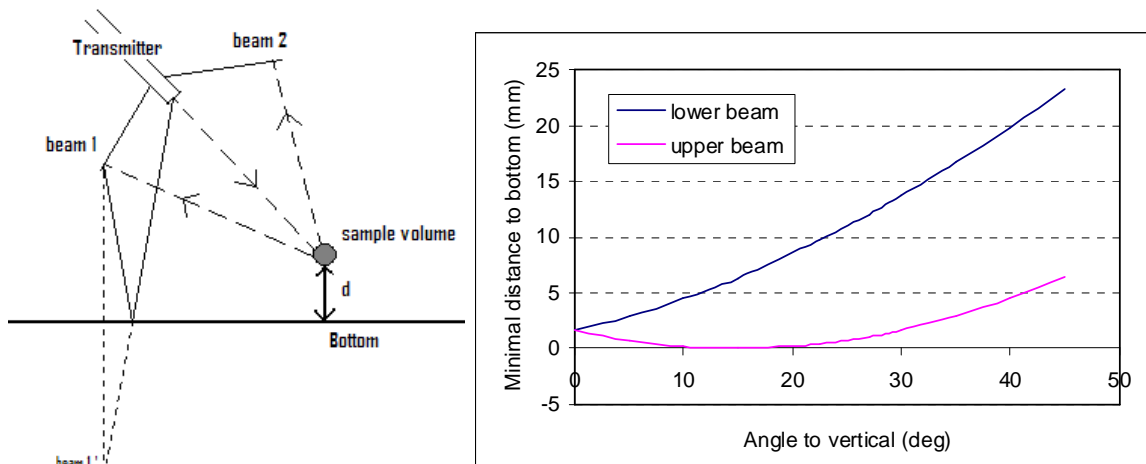

Figure 8, left: Reflection of side lobe signal to the bottom. Close to the bottom, this track can be exact as long as for the echo of the sample volume and thus can't be distinguished by the ADV.

13

Right: range from the bottom for which side lobe reflection can occur, as functions of the vertical ADV angle. By twisting the ADV 45 degrees around its own axis, this critical range is smaller.

Apart from the vertical angle, the ADV probe was twisted around its axis for ca. 45 degrees to increase the measurable depth range (figure 10, right panel). The probe was mounted in a construction movable in transverse and vertical direction. To minimize the orientation angle differences between measurements, handscrews were used to fix this construction to a horizontal bar (figure 9). This was mounted again on a carriage which could be moved over length of the flume.
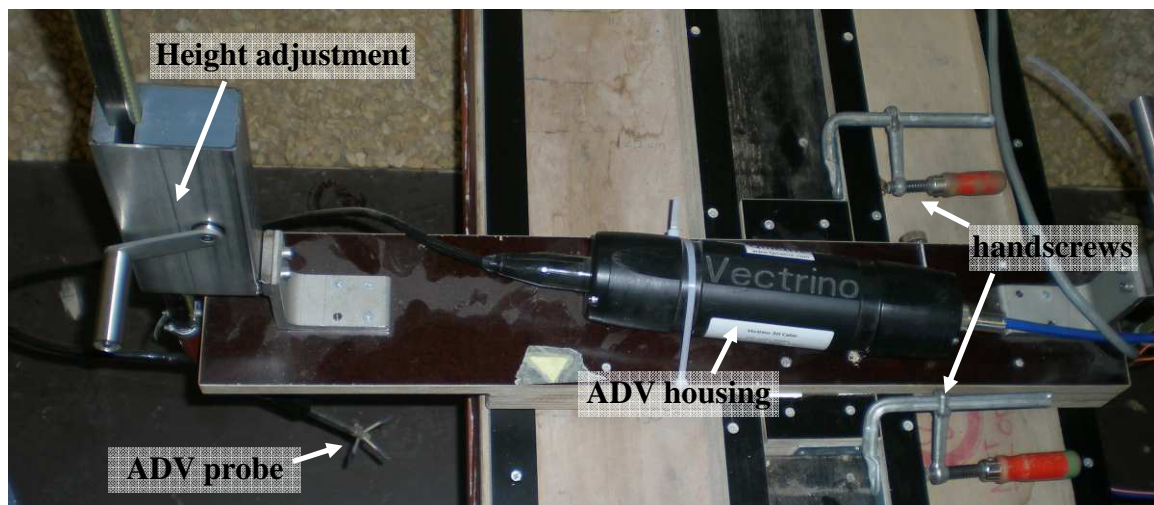
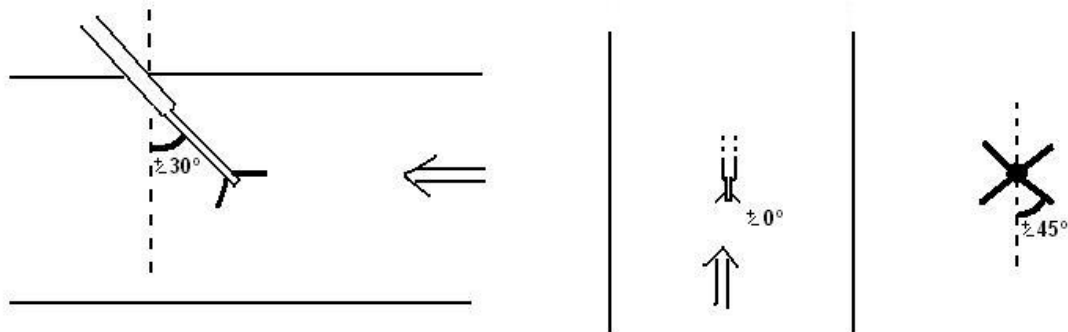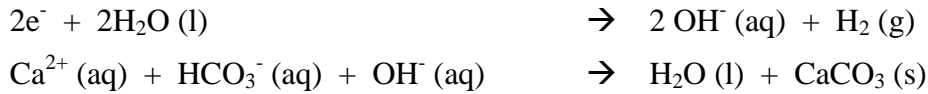*Figure 9: image of mounting construction for ADV*

Figure 10: orientation and mounting of the ADV. Left: side view, middle: top view, right: front view.

A key assumption in using acoustic velocimetry is that the scattering particles in the water have the same velocity as the water itself. For small particles, this is a reasonable assumption. Furthermore, there must be enough particles in the water to have an accurate measurement. This is solved in this experiment by using an electrolyser 70 cm ahead from the ADV. The electrolyser produces very small water bubbles (small enough to neglect to extra upward velocity) which strongly improve the ADV signal. By using this electrolyser, the resulting signal-to-noise ratios (SNR) exceed 20 and correlations of the received ADV signal are 90-98%.

An unwanted result of the electrolysing is the formation of chalk at the electrolyser:

$$2e^- + 2H_2O\ (l) \qquad\qquad \rightarrow \quad 2\ OH^-\ (aq)\ +\ H_2\ (g)$$

$$Ca^{2+}\ (aq)\ +\ HCO_3^-\ (aq)\ +\ OH^-\ (aq) \quad \rightarrow \quad H_2O\ (l)\ +\ CaCO_3\ (s)$$

The chalk reduces the water bubbles density and eventually the data quality. Therefore, the electrolyser was cleaned at least within 3 hours running.

The ADV was configured to measure at 25 Hz, using a sampling volume of 4.0 mm and a transmit length of 1.8 mm. Data was gathered by using the delivered program of Nortek (Vectrino 1.06) and was stored in beam coordinates, to be able to filter data with insufficient quality. For more details about the ADV used, see Nortek AS (2004). Initially series of 6 minutes were recorded; this was changed to 3 minutes series after performing a time scale analysis on the first data (see next paragraph).

Time scales

For a good choice of the length of the measurement, a brief time scale analysis is done for velocity and water level data. Figure 11 shows a representative example of a power density spectrum for the water levels, using the variance preserving plot method (power density multiplied with frequency; then the area under the graph equals the variance contribution). The peaks in the low-frequency range of this spectrum can be explained by the reflection of shallow waves to the flume boundaries, using a wave group velocity of $\sqrt{g \cdot h}$, the average flow velocity and the flume sizes. The spectrum shows that motions over more than 100 seconds have hardly any influence on the water level.
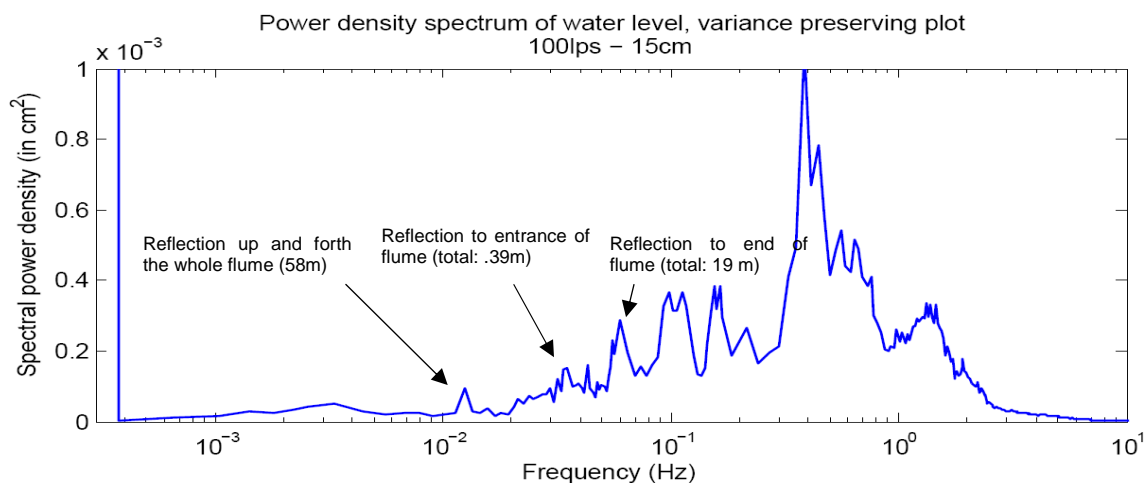

Figure 11: Power density spectrum, in variance preserving plot, of water level data. The data, measured by the electronic gauge, originates from the 100lps – 15cm case and spans over 4 hours. Data was windowed in 1.46-hour parts, 50% overlap and a Hamming window function. The spectrum for high frequencies is smoothed. The peaks that can be explained by reflection of shallow waves to the flume boundaries are indicated.

Despite to this analysis, it appears that very long data series of the water level show a small trend in the water level, outside the frequency range of figure 11. Figure 12 shows a

15

data series in which this effect is most pronounced. Although the flow had already half an hour before the start of this series to reach equilibrium, the water level is slowly increasing with ca. 0.5 mm. This trend is probably caused by a slight movement of the weir due to the weight of the water. The effect is assumed negligible on the velocity (the discharge did neither have such a long term trend), and to ensure that this also has no effect on the water level slopes, the water level measurements have been done at least in duplo, back and forth.
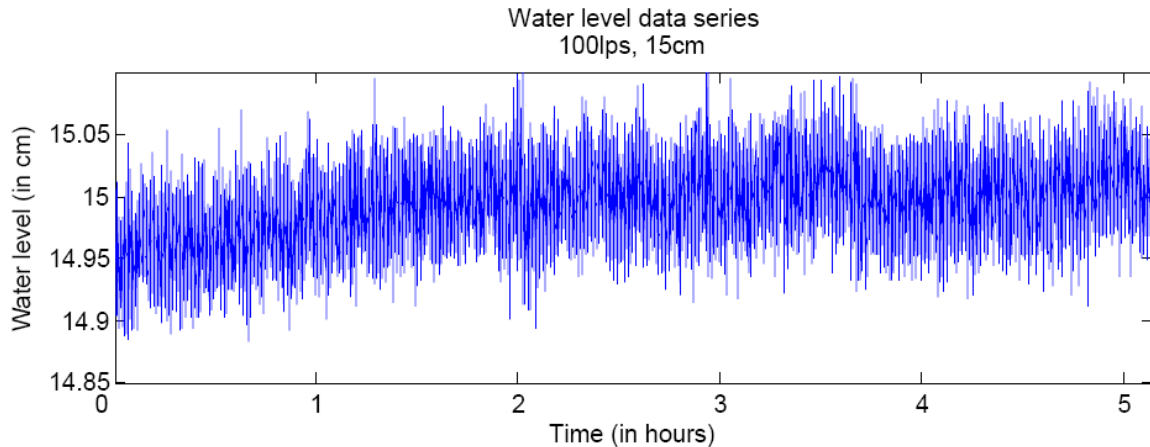

Figure 12: Example of a water level data series, from the 100lps – 15cm case, measured by the electronic gauge. Most other data series are much less trended.

The spectra of velocity data series are much more varying than the water level spectra, dependent on discharge and depth. Figure 13 shows two spectra (again in a variance preserving plot), one based on a single 30-minute data series and one based on all velocity data (6 minutes each) of the 40lps – 11cm case and the 100lps – 15 cm case. Both spectra show that frequencies below 0.03Hz have a minor contribution to the variance and thus to turbulence.
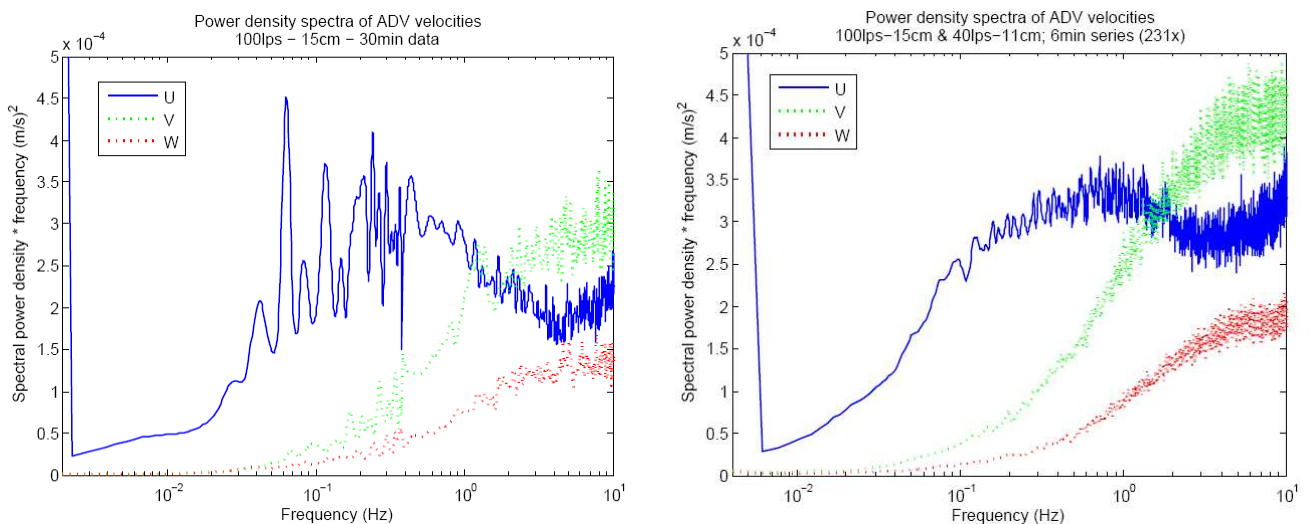

Figure 13: Power density spectra, in variance preserving plot, of ADV velocity data. Left: spectra of a 30-minute series at 100lps, 15cm depth, at y=88cm (smooth), z=5cm. Right: spectra based on all 6-minute series, measured at 100lps – 15cm and 40lps – 11cm, above smooth as well rough. All spectra are full-size windowed (Hamming window function) and smoothed especially at higher frequencies.

Based on the spectra showed above, a 3-minute measurement interval appears to be sufficient to cover all variations of importance in velocity and water level. Therefore, the ADV-data and water level slope measurements are spanning over at least a 3-minute interval.

Temperature and viscosity

The water temperature has a decreasing trend in the winter period, as a consequence of the decreasing temperature in the laboratory. Therefore, the viscosity was changed about 15% over the total measurement set; see figure 14. However, because the viscosity is only used in calculations of the Reynolds number, no correction is made for this change. The average value of $1.08 \cdot 10^{-6}$ m^2/s is used for the kinematic viscosity in all calculations.
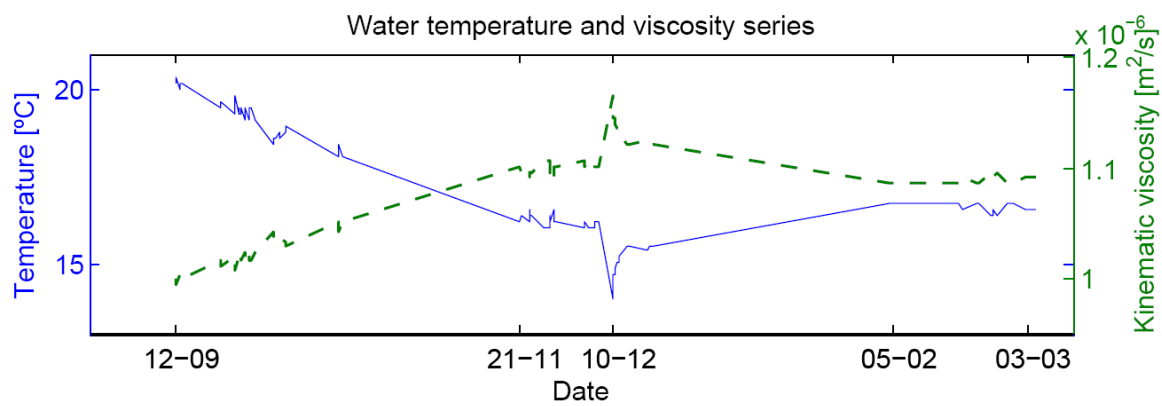

Figure 14: Temperature (solid line) and kinematic viscosity (dashed line) of the water in the flume. The temperature was measured by the ADV probe, the viscosity calculated by an exponential model.

Particle tracking velocimetry (PTV)

By the particle tracking velocity method, two images taken shortly after each other are compared to detect particle movements by using a correlation in space. Black particles, having a density just smaller than water, were used to track. To improve the contrast of the particles, the bottom was painted white and 12 TL-lamps were used (4 at each side, 2 in front and behind the image area). See figure 15 for the camera and lamps setup. The particle tracking velocity method reveals in relatively few time a 2D velocity field. This measurement technique is restricted to the upper layer as the particles float in the upper layer. Furthermore, small local vortices are some underestimated as the particles can turn around their own axis. The average flow field is without dubiety untouched by this effect and is very useful.
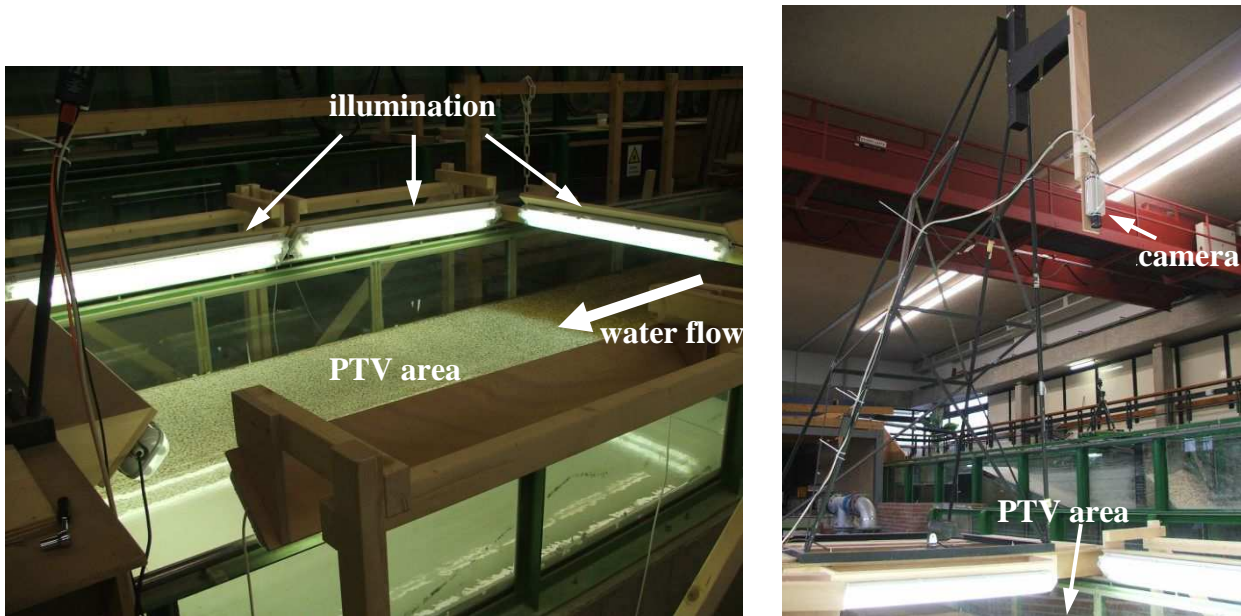
Figure 15: Experiment setup for PTV method. Left image: TL-lamps illuminating the PTV area. Right image: PTV-camera, fixed 2 meter above the water surface.

In case of a flow with secondary circulation, one can expect zones of accumulation and depletion of particles across the flume. By counting the particles as function of the width, a rough measure of the cumulative cross flow upstream is determined. For this reason, the camera was mounted at only circa 2 meter above the water surface for the first configuration. In the end, the particle counting appeared to be unreliable since the particle dispensing was not completely homogeneous. Therefore, the camera was placed at circa 3 meter above the water surface for the last (checkerboard) configuration to cover a larger measurement area.

The camera used for PTV measurements was a MegaPlus ES 1.0, at a resolution of 1008*1018 (1.0 megapixel), with an adjustable frequency pulser. The images were saved by Savant 4.0 software and afterwards processed in MatLab.

Pre-processing ADV-data

Outliers in ADV data, however sparse, are sometimes created as the scattered sound is not always strong enough to be correctly measured. Especially close to the boundaries, some data was corrupted. Therefore, the ADV data was filtered for:

- low correlation
- low signal to noise ratio (SNR)
- large deviation in signal amplitude
- large deviation in velocity
- large difference in velocity in subsequent samples

Beside from the data of beam 3, more than 99% of the data passed the filtering. Beam 3 has a systematic higher signal-to-noise ratio (SNR), quite some time even below 0. Therefore, the data from this receiver is regarded unreliable and a three beam solution will be used (as three beams give also enough data for all velocity components). In order to obtain an accurate result, the calibrated transformation matrix is used; in this matrix the

real beam velocity angles are used in stead of the estimated 15 degrees. By rewriting equation 11 and the 4-beam transformation matrix, the exact angles can be solved. Table 1 shows the beam signal angles and the corresponding three beam transformation matrix of the used ADV.

Table 1: ADV signal angles (i.e. half of the geometric beam angles) solved from calibration matrix. The shown transformation matrix is used for a three beam solution without using beam 3.

ADV signal angles [º]		Transformation matrix				
			V_1	V_2	V_3	V_4
beam 1	14.07	V_x	4.1130	-2.1253	0	-1.9850
beam 2	13.47	V_y	0	2.0649	0	-2.0737
beam 3	14.37	V_z	0	0.5327	0	0.4976
beam 4	14.44		0	0	0	0

This transformation matrix gives the output in coordinates with respect to the instrument. To transform to a coordinate system of the water flow (streamwise, spanwise and vertical), a rotation matrix is required. This matrix has three variables: the angle to the vertical (around 30º), the angle due to a skew instrument fixation (around 0º) and a rotation in the instrument fixation (around 45º); see figure 10 for an illustration. Calibrating these angles such that the plane averaged cross and vertical velocities are minimized, these angles are found to be respectively 31.9º, 0.0º and 51.1º. The last two values are sensitive to initial values (there appears to be several local minima); these values are physically most reasonable.

A small disadvantage of using this three beam solution is that the instrument noise is not equal in the x and y instrument direction. This is not really inconvenient as the ADV is twisted around 45º, so this effect will be equal in the streamwise and spanwise directions.

Pre-processing PTV-data

The images for the PTV method are read and processed by MatLab scripts. For detecting the particles for PTV, the background has to be subtracted from all images. The background images are made before the particles were introduced in the water. Because TL-lamps were used for a homogeneous light distribution, the frequency of the electricity supply (50Hz) gave a slowly varying interference with the sampling frequency (10, 20 or 25Hz). To deal with this effect, the background images and the measurement images are both sorted based on light intensity and hence the best corresponding background is subtracted.

Next, the contrast is increased by regarding local minima and maxima. This filter was used to avoid the spatial intensity variations caused by differences in lamp radiation. After this step, particles are labelled and finally velocity vectors can be calculated (based on the greyscale image). This is done in again in two steps; one rough estimate based on a Fast Fourier Transformation (FFT) and a finer calculation by a search to the (interpolated) cross-correlation peak. A last check for consistency in the velocity field ensures that all resulting velocity vectors are trustworthy.

Table 2: Depth and discharge situations for which measurements were executed

Nr	1	2	3	4	5
Q [L/s]	7.5	40	40	100	100
D [cm]	3.5	8	11	15	22
k_s/D	0.54	0.24	0.17	0.13	0.09
Fr_{smooth}	0.21	0.33	0.20	0.32	0.18
Re_{smooth}	4.0 E+3	2.1 E+4	2.1 E+4	5.3 E+4	5.3 E+4

Experimental parameters

All measurements were done in four situations, differing in depth and discharge. For a fifth situation, with the smallest depth involved, only PTV and water level measurements were done. Table 2 lists the examined depth and discharge situations. The different settings were chosen to investigate the effect of differences in relative roughness and length/depth ratio. The choices were limited by the Froude number (<0.5 to ensure a smooth water level), the minimum level of the weir (in case of the lower two situations) and the ADV measurement range (between 1 cm above bottom and 4 cm below water surface). This makes that the heterogeneous floodplains with very large bushes or trees involved cannot be represented by these experiments since the relative roughness in the experiments is 0.54 at maximum. Heterogeneous rough floodplains with smaller vegetation (grasses to small bushes) have a relative roughness that fits in the range of the relative roughness in these experiments.

Measurement locations

The grid spacing between the ADV measurements was chosen smallest in the region were the mixing layer was expected. A few measurements are located in the (expected) outer field, in a coarser grid. Figure 16 shows the horizontal positions of the ADV and PTV measurements. For the developed situation (x = 12.5 m), vertical profiles with at least 6 sample points were measured; most other locations were covered by less measurements in the vertical. The locations in figure 16 are subject to measurements for the four deepest depth situations; extra measurement positions, done in only some depth situations, are not projected.

The camera used for the PTV was located at approximately 2 meter above the water surface for the first configurations and ca. 3 meter above the water surface for the checkerboard configuration. Subsequently, the area covered in the PTV-measurements is larger for the checkerboard configuration, whereas higher detail is available for the first configurations (for an attempt to apply particle counting in the developed configuration).
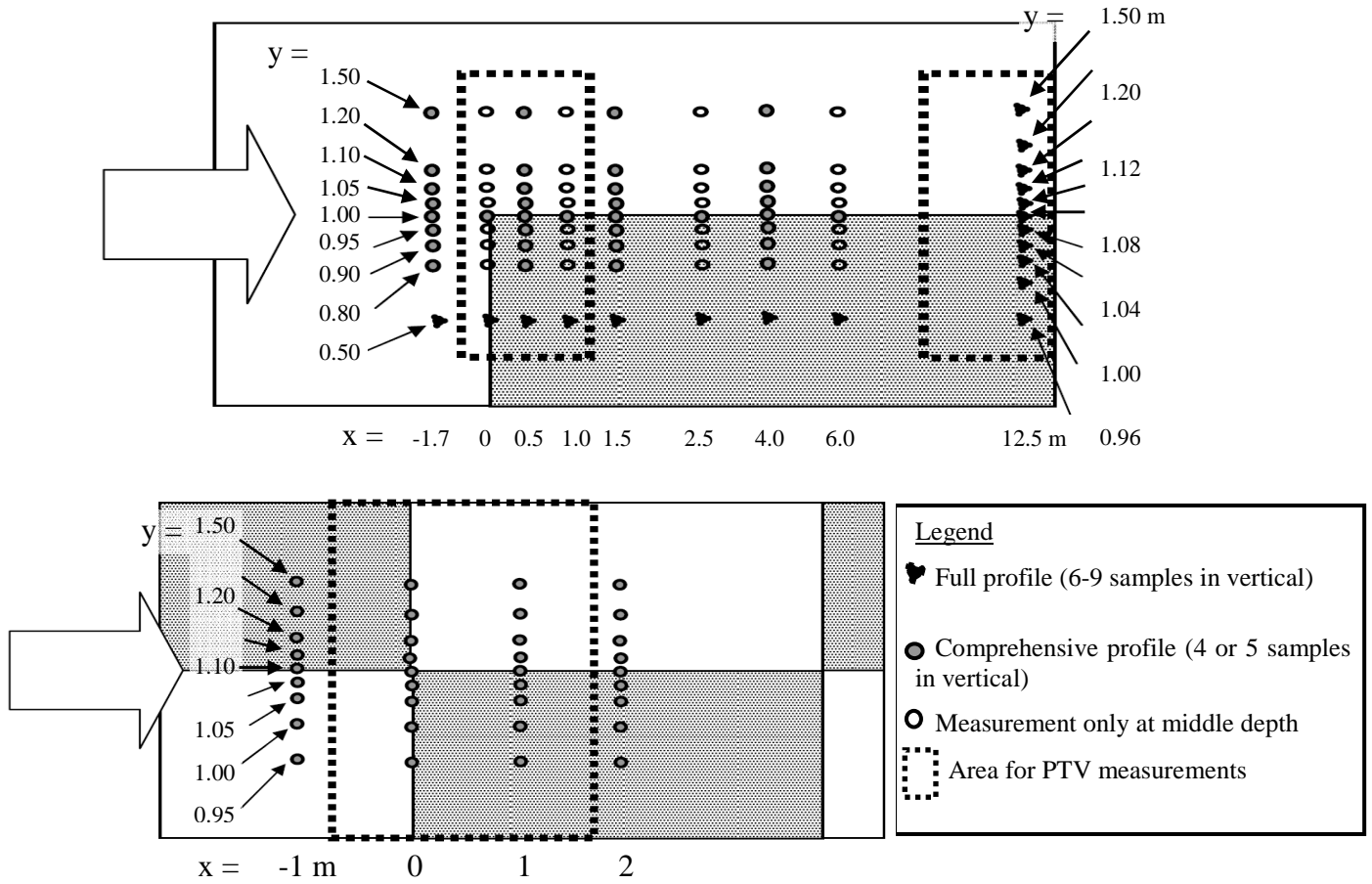
Figure 16: Position (in top view) of ADV and PTV measurements. The upper panel shows the measurement locations of the first configurations (resp. configuration 1a and 1b), the lower panel shows the measurement locations in the checkerboard configuration.

Large Eddy Simulation (LES)

In the laboratory experiments, the number of measurements and the measurement precision are restricted due to the instrument range and available time. A detailed simulation is a useful tool in this case for extending the understanding of the experiments. Large Eddy Simulations (LES) can give a good representation of the actual turbulent open water flow; rather than Reynolds averaged models (Pope, 2000, p.558) A LES resolves the large motions directly by using the spatially filtered Navier-Stokes equations; small motions (eddies) are solved by using a sub-grid scale model. The Smagorinsky sub-grid scale model (Pope, 2000, p.587) is prevailing in LES applications and also used in this case. This model accounts for the small eddies by adding a turbulent viscosity to the molecular viscosity. The division between large and small eddies is equal to the grid size. So all motions larger than the grid size are solved by applying the Navier-Stokes equations, all smaller motions are handled by the Smagorinsky model.

For this experiment, two situations have been calculated by using LES:

- fully developed flow subjected to parallel bottom roughness (configuration 1b)

- flow over roughness in a checkerboard pattern (configuration 2)

21

The LES algorithm used for these cases was adapted from Wim van Balen. An introduction to this algorithm is given by Boersma (internet, 2007). This model has a staggered grid and makes use of a constant pressure gradient, with a correction for pressure deviations afterwards. The effect of the bottom (and side wall) boundaries are modelled by making use of the logarithmic law of the wall; the friction velocity is calculated by applying this law on the lowest grid cell. This might introduce an error for non-uniform flow, since the logarithmic law is not valid in that case. Due to the limiting available time, this error is accepted.

The grid cell size used in the simulation varied from 0.175 to 1 cm, dependent on the case. The Smagorinsky constant was set to 0.1. The roughness height (k_s) was by default set to 19mm for the rough parts and hydraulically smooth for the smooth part. At the interface between the smooth and rough section, an intermediate roughness height (respectively 1/3 and 2/3 of 19mm) was assigned to the two grid cells to avoid unrealistic gradients. At least 400000 time steps were calculated in order to obtain representative statistics for a steady flow.

3) *Results of developed parallel flow*

Longitudinal velocity

A mixing layer evolves around the interface of the parallel smooth and rough sections. The measured longitudinal velocity does not obey the tangent hyperbolic mixing layer profile as proposed by Van Prooijen (2004). Figure 17 shows transverse profiles of the streamwise velocity (u) resulting from ADV measurements, split out for several heights. Those transverse profiles have an asymmetrical shape, especially closer to the bottom. Above the smooth lane, equilibrium in longitudinal velocity (i.e. $\partial u/\partial y \approx 0$) is reached at a transversal distance of ca. 2–4 times the water depth away from the interface, whereas above the rough lane the equilibrium is reached at a distance of 1-2 times the water depth. Results from the LES are in accordance to the measurements; see figure 18. Apparently, the momentum exchange occurs over a longer width above the smooth side than above the rough side. In the following paragraphs, the two mechanisms for momentum exchange (mixing layer shear stresses and secondary circulation) are investigated.
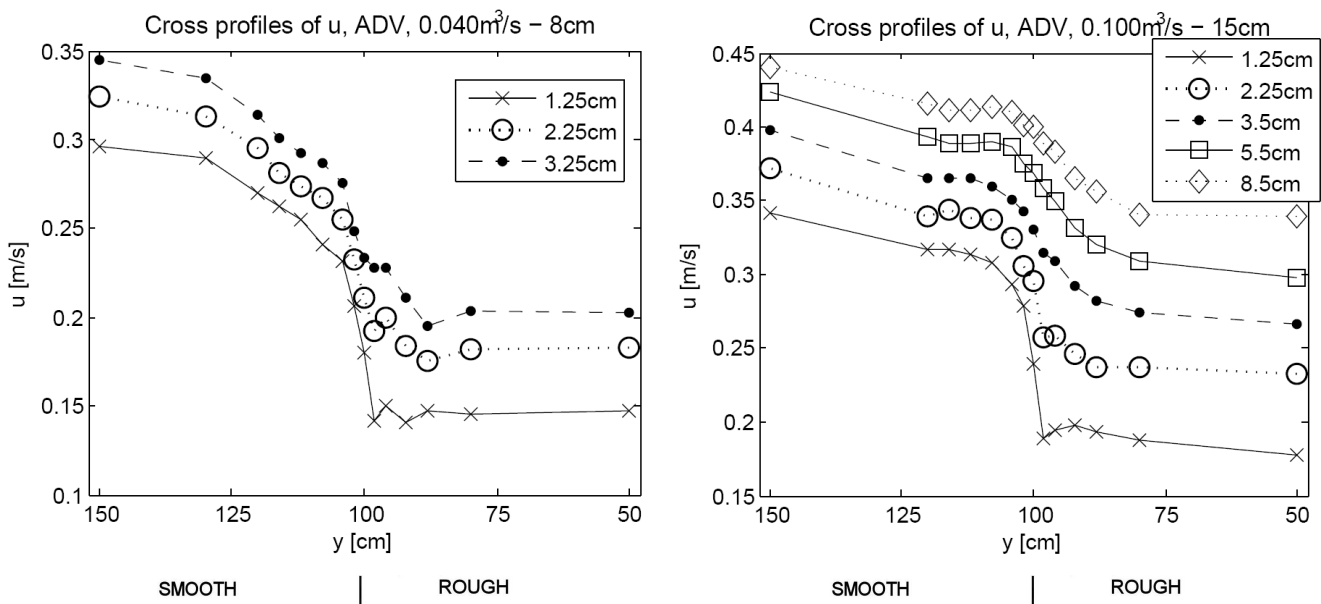

Figure 17: Transverse profiles of mean longitudinal velocity, at several depths, measured by using the ADV. Left: data from the 8cm case; right: 15cm case.
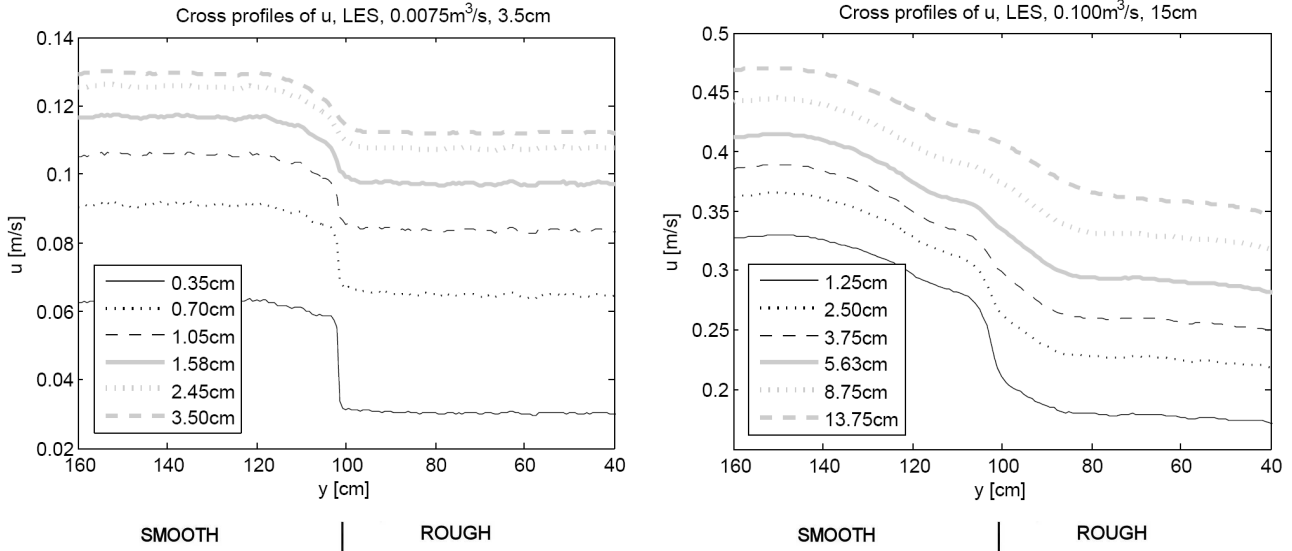
23

Figure 18: Transverse profiles of longitudinal velocity, at several depths, resulting from the LES. Left: 3.5cm case; right: 15cm case.

Some bulges in the data of figure 17 can be seen compared to a smooth profile. Most consequent are the dip at y = 98 cm for the profiles closest to the bottom and a subtle positive bulge at all depths at y = 108 cm. The momentum exchange (see later in this chapter) gives more clarity about these effects. The latter of the deviations with respect to a smooth profile are most likely the result of an error in the vertical position of the ADV. The velocity at the surface seems to be smoother and more symmetrical; see figure 19 for surface velocities from PTV measurements.

This figure also shows that the velocity difference between the smooth and rough side is relatively larger for small depths, a logical consequence of the higher relative roughness. Not only the surface velocity, but also the depth averaged data or fixed level data (by ADV) agrees in this observation. Theoretically, the ratio in velocity outside the influence of the mixing layer should be inversely proportional to the square root of the friction coefficients c_f. This follows from the equation of motion by assuming equilibrium and no transverse momentum exchange:

$$c_f \cdot U^2 - g \cdot h \cdot S = 0 \qquad \text{(equation 13)}$$

Since S is equal at both the rough and smooth side, there can be stated:

$$c_{f,smooth} \cdot U_{smooth}{}^2 = c_{f,rough} \cdot U_{rough}{}^2 \qquad \text{(equation 14)}$$

$$\frac{U_{smooth}}{U_{rough}} = \frac{\sqrt{c_{f,rough}}}{\sqrt{c_{f,smooth}}} \qquad \text{(equation 15)}$$

Furthermore, the surface velocity profiles in figure 19 show that the highest velocity of the 22cm case is very close to the smooth-rough interface, which points out that the mixing layer is not yet developed at the surface. The ADV data showed a more distinct mixing layer for this case, indicating that the mixing layer is more developed at lower depths. The development lengths will be further discussed in chapter 4.
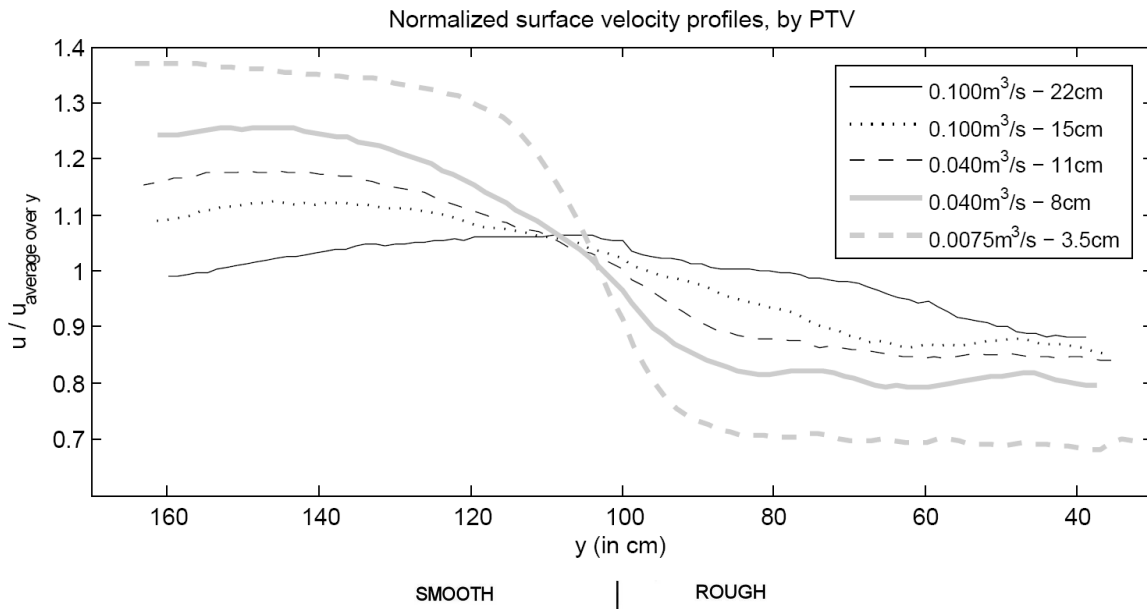

Figure 19: Surface velocity measured by PTV, normalized on the width-averaged surface velocity.

Secondary circulation

ADV measurements are done on a dense grid in a cross sectional plane for the developed parallel roughness flow in order to get certainty for a secondary circulation. Thanks to this fine detail, a secondary circulation can be recognized in all cases; see figure 20.

Figure 20 shows that low velocity magnitudes are involved in the secondary circulation; only 1 to 2% of the velocity in streamwise direction. Local effects or a very small deviation in the ADV angle has a major effect for the velocities in this cross plane. For that reason, some vectors (close to the bottom) in figure 20 are inconsistent. Nevertheless, most vectors clearly show a clockwise circulation with the centre of rotation above the smooth bed side. The total horizontal size of the circulation cell appears to be about twice the water depth; the horizontal distance from the centre of rotation to the smooth-rough interface is almost equal to the water depth. This shift of the centre of rotation wasn't visible in preliminary research to similar circulations (Studerus, 1983; Wang & Cheng, 2006) since the parallel sections in these experiments were too narrow. Something that was mentioned in there, in agreement with these results, is the vertical position of this centre of rotation: somewhat below the middle depth.
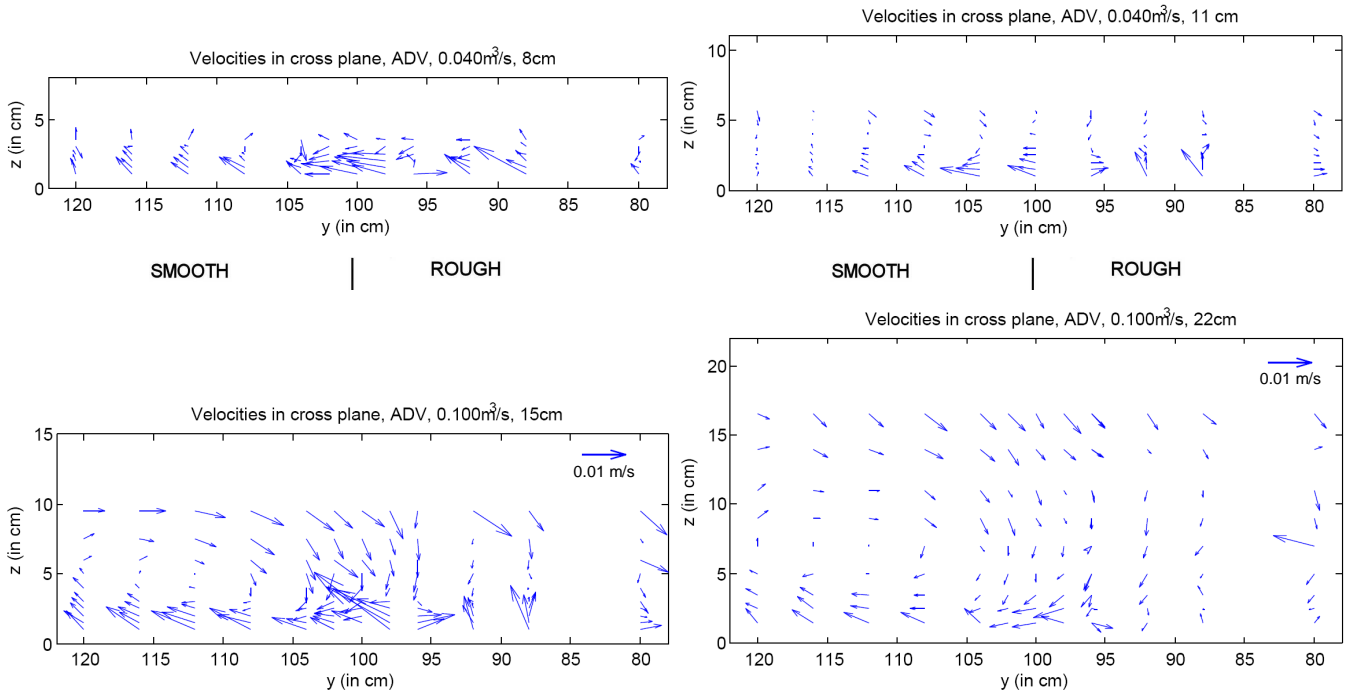
Figure 20: Velocity vectors in a vertical cross plane (view in flow direction) for developed flow, for all cases measured by ADV. All axes and all vectors are equally scaled.

The LES produces similar secondary flows for the same depth situations (figure 21, left panel), only with the centre of rotation slightly higher located. For the shallowest depth (3.5cm), the flow structure is somewhat distorted and the secondary circulation cell seems to split into two cells. Either the circulation cell gets a too large width/depth ratio; either the secondary circulation is not fixed at one position.
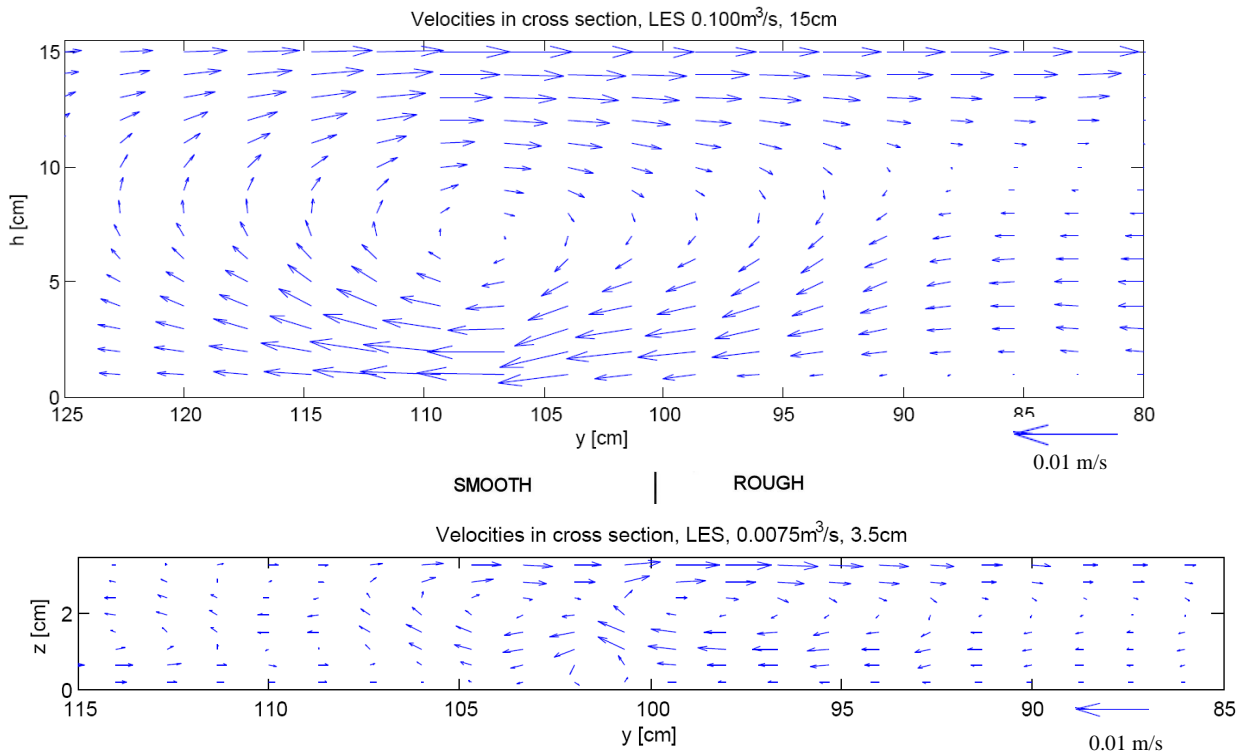
Figure 21: Velocity vectors in a vertical cross plane (view in flow direction) for developed flow, for a 3.5cm depth case (upper panel) and for a 15cm case (lower panel)

In order to explain the horizontal location of the centre of the secondary circulation, the distribution of TKE production in the LES results is analysed in detail. Figure 23 shows the individual production terms from equation 9 and the sum of those. The bottom-shear TKE production term, $-\overline{u'\cdot w'}\cdot \partial\overline{u}/\partial z$, is shown to be largest. The maximum values are found just above the rough side of the interface and are much more pronounced than the dip at the smooth side. This is explained by the non-linear dependency of turbulence production on the velocity (gradient). An increase in velocity above the rough side of the interface (compared to the velocity in the middle of the rough lane) has quantitatively more effect on the turbulence production than the decrease of velocity (compared to the velocity in the middle of the smooth section) above the smooth side of the interface. Figure 22 illustrates this situation.
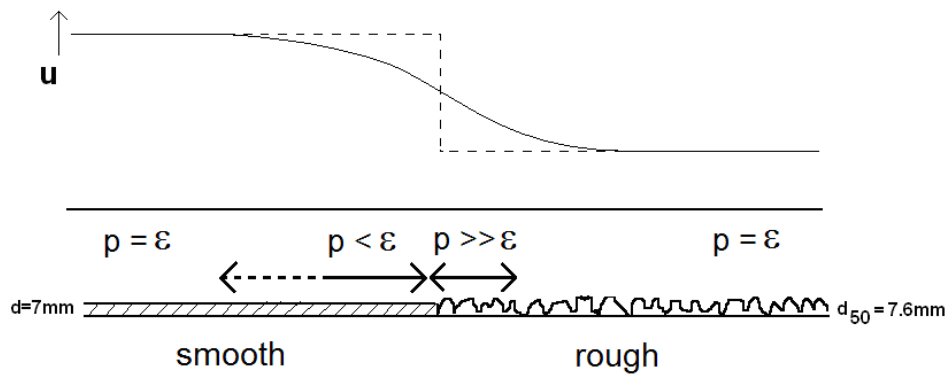

Figure 22: Illustration of balance between production and dissipation along the width. Above: schematic profile of longitudinal velocity

The other production term, $-\overline{u'\cdot v'}\cdot \partial\overline{u}/\partial y$, is representing for the mixing layer turbulence and causes a slight shift of the total TKE production maximum towards the smooth side. Due to this shift and the non-linearity in the first TKE production terms, the maximum in total TKE production is located very close to the smooth-to-rough interface. This maximum (thus a local TKE production excess) is much more pronounced than the minimum above the smooth lane. Hence the region of dissipation excess is spread out over a larger area above the smooth side (figure 23). Therefore, the local excess of turbulence production nearby the interface is, following equation 9, the main driver for the observed secondary circulation. This local turbulence excess causes downwelling around y=95-100 cm whereas the remainder of the circulation is required to satisfy continuity. In conclusion, equation 9 explains the existence of the secondary circulation and also helps understanding the asymmetry of the secondary circulation cell as observed in figure 20.

One might argue that these results could not explain the origin of the secondary circulation since they are obtained from a flow situation in which a secondary circulation was already present. However, the phenomena that explain the results in figure 23 (the non-linearity in TKE production and the mixing layer turbulence production) are even expected in the absence of a secondary circulation cell.
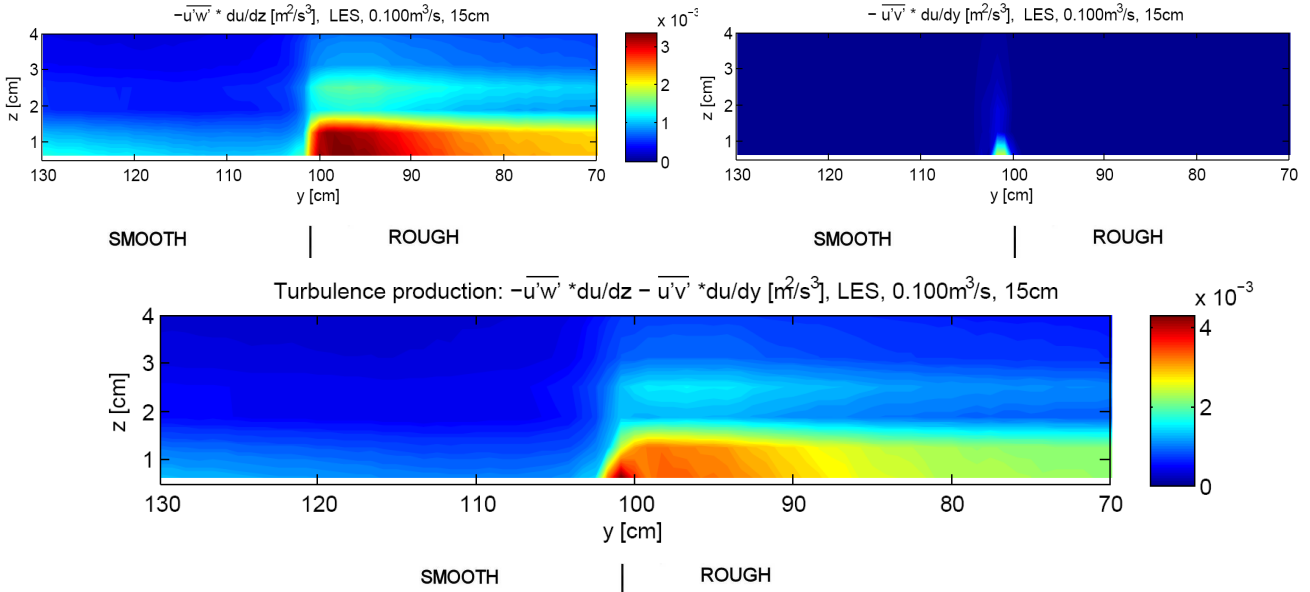
Figure 23: Turbulence production (in m^2/s^3) computed by using a LES. Top left: contribution of $-\overline{u'\cdot w'}\cdot\partial\overline{u}/\partial z$. Top right: contribution of $-\overline{u'\cdot w'}\cdot\partial\overline{u}/\partial z$. Lower panel: sum of both turbulence production terms

Shear stresses

The turbulent shear stresses determine the flow structure and are therefore very important for a good understanding of the flow over heterogeneous beds. The turbulent shear stress $-\rho\cdot\overline{u'v'}$ is important for direct momentum transport between the rough and smooth section. The other turbulent shear stresses, involving $\overline{u'w'}$ and $\overline{v'w'}$, are induced by bottom friction. The bed shear stress is determined by extrapolating the $\overline{u'w'}$ profiles to the bed (ADV measured, figure 24) and using equation 3; see figure 25. This figure clearly shows a maximum in bed shear stress at the rough side of the smooth-rough interface (y=98cm). At the smooth side near the interface hardly or no reduction in bed shear stress is visible, in agreement with figure 23. A note to the values in figure 25 is that the bed shear stress is probably overestimated at y=102 and 104 cm, while underestimated at y=92-100 cm. This is deduced from the convex vertical profiles of $\overline{u'w'}$ at y=102-104 cm and the concave profiles at y=92-100 cm (figure 24).
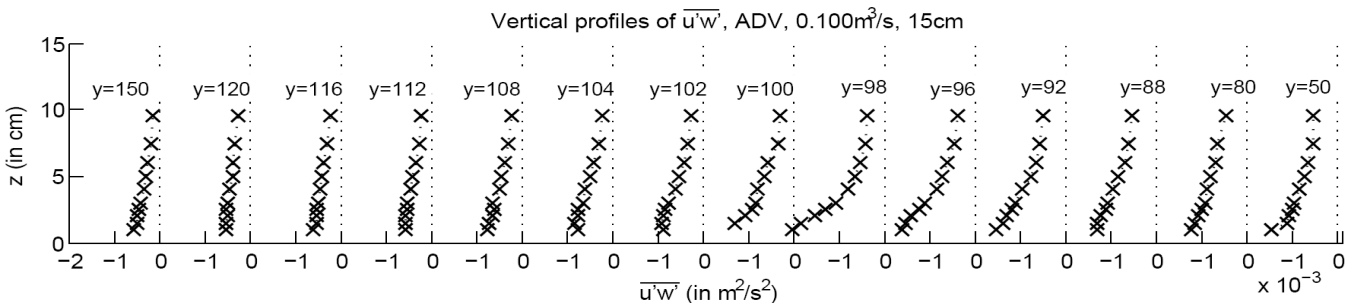

Figure 24: Vertical profiles of covariance $\overline{u'\cdot w'}$, measured by ADV, case 0.100m^3/s, 15 cm depth. The width coordinate is labelled to each profile, profiles are shifted 0.002 $m^2 s^2$.
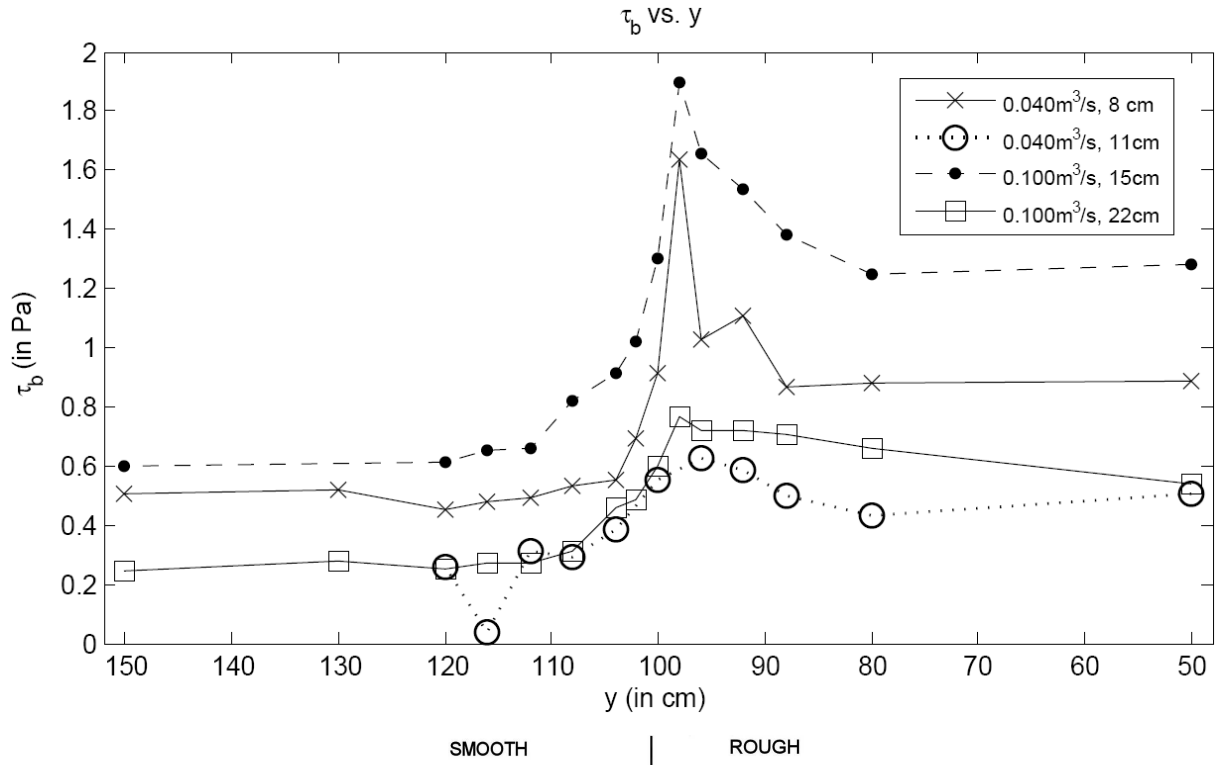
Figure 25: Bed shear stress versus width, derived from $\overline{u' \cdot w'}$-profiles, measured by using an ADV, for several depth-cases.

Figure 25 also shows that the bed shear stress at y=50 is somewhat higher than at y=150 cm. This indicates that there is still net transverse momentum exchange at 50 cm from the interface. After all, an equal pressure gradient at both sides means an equal bed shear stress at both sides. This is also shown in the next paragraph. Apparently the flume is somewhat too narrow for the presence of a region outside the influence of the mixing layer or side wall.

The covariance term $\overline{u'v'}$ is especially important for momentum exchange in the mixing layer. The next paragraph will address that topic. Figure 26 shows that this term is at maximum close to the bottom and near the smooth-rough interface. Moreover, this figure illustrates that at higher levels the maximum in $\overline{u'v'}$ can be found above the rough side. This can be understood in combination with the velocity profiles from figure 17 and figure 18; the maximum velocity gradient (i.e. $\partial u/\partial y$) at higher levels can be found above the rough side.
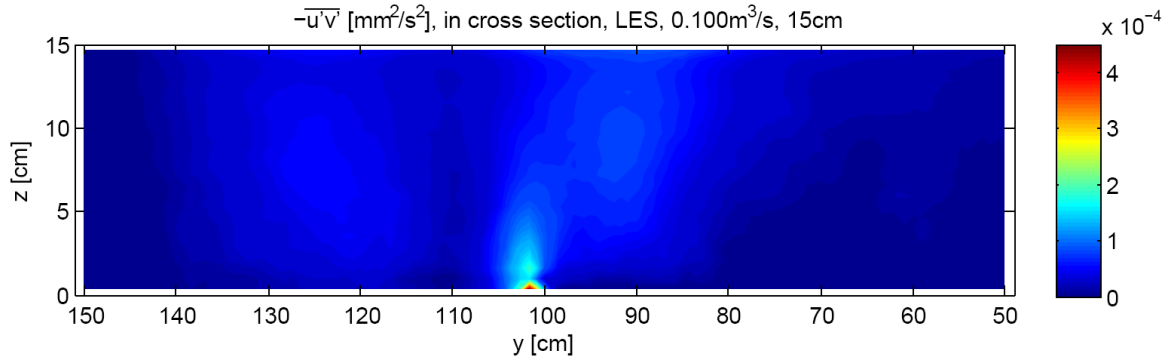

29
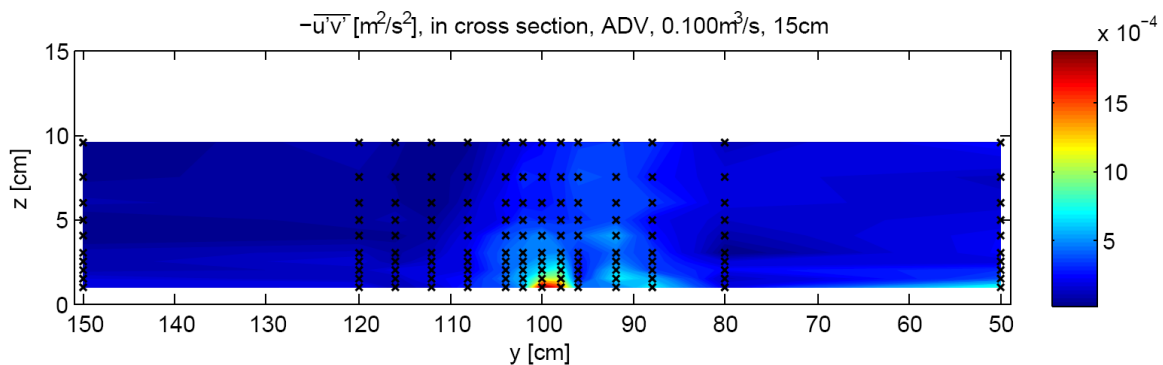
Figure 26: Velocity covariance - $\overline{u' \cdot v'}$, resulting from ADV-measurements (upper panel, measurement locations indicated) and LES (lower panel) for the case of 15cm depth.

A remark on the shear stresses as depicted in figure 26 is that the turbulent stresses from the LES, are systematically lower; $\overline{u'v'}$ is ca. 4x smaller in the LES results, $\overline{u'w'}$ about 3x smaller and $\overline{v'w'}$ about 10x. In appendix B, where the local friction coefficients are compared to the overall friction factors, it seems that the effect is due to both results: stresses measured by using the ADV are too high and the stresses resulting from the LES are underestimated. Reasons for this hypothesis are:

- ADV turbulence results are biased due to aliasing and receiver-dependent noise. The aliasing is shown by the cross spectral density (Appendix B). A bias due to noise is enhanced due to the use of only 3 ADV receivers (the fourth one had unacceptable high signal-to-noise ratios). By using all four receivers, the shear stresses become approximately 30% smaller (not shown).

- Too low stresses in the LES can be due to the non-physical (parameterised) implementation of roughness in models. One must realise that form drag and roughness effects near the bottom are not implemented physically in a flow model. Form drag can be parameterized by the k_s for representing average flow properties, except for two effects:

  o form drag is dependent of the velocity, so k_s is also dependent of the velocity

  o increased spatial flow fluctuations at the parallel smooth-to-rough interface due to the irregularity of the interface. The roughness elements result in an irregular interface in stead of a very strict line. That causes the flow just above the interface to meander, with consequently extra turbulence and bed shear stress.

As a consequence of the underestimated shear stress in the LES, the pressure gradient was too small. Nevertheless, the patterns of distribution of shear stress and turbulence from LES and ADV-measurements are in rather good agreement. This is explained in appendix B.

The roughness parameters in the LES were increased to $k_s = 80$mm for the rough side and $k_s = 0.55$mm for the smooth side to better approach the measurements. Unfortunately, this had a negative effect on the agreement in time-averaged velocities. In a follow-up research, the calculation of the bed friction (now based on a log-law for the lowest velocity grid cell) must be revised. The results presented for the developed parallel flow are obtained with the original roughness parameters (resp. $k_{s, rough} = 19$mm and hydraulically smooth).

Momentum exchange

For the contribution to effective friction, the momentum transfer over the smooth-rough boundary is of particular interest. The depth-averaged momentum exchange between the smooth and rough sides of the flume can be established by advection due to secondary circulation and by turbulent mixing (vortices with a vertical axis). The transverse momentum exchange associated to these mechanisms can be quantified respectively by the terms in respectively equation 16 and 17:

$$T_{adv} = \frac{1}{h}\int_0^h \left(-\overline{u} \cdot \left(\overline{v} - \frac{1}{h}\int_0^h \overline{v}dz \right) \right)dz$$

(advective momentum transport, equation 16)

and

$$T_{mix} = \frac{1}{h}\int_0^h \left(-\overline{u' \cdot v'} \right)dz$$

(turbulent momentum transport, equation 17)

The advection of momentum across the smooth-to-rough interface can only be calculated in a depth averaged way, since water is advected towards the rough side in the upper layer and towards the smooth side near the bottom. Multiplication of the transverse velocity profile with the longitudinal velocity profile leads for a depth averaged approach to a net momentum transport from the smooth to the rough side. This is applied to ADV data in figure 27 (third panel). The most right panel of figure 27 shows that the transverse momentum exchange by turbulent mixing is positive at all depths and is strongest close to the bottom.

In equation 16 a correction is made for depth-averaged transverse mass transport. In theory, this mass transport should not be apparent (since the flow is developed). Though, the measurements showed a very small depth-averaged transverse mass transport, which can be due to a limiting development or a subtle misalignment of the ADV. This very small mass transport would result in a significant influence in momentum exchange, while this is not realistic. Therefore a correction is made in equation 16. The momentum exchange by depth-averaged mass transport is treated in chapter 4.
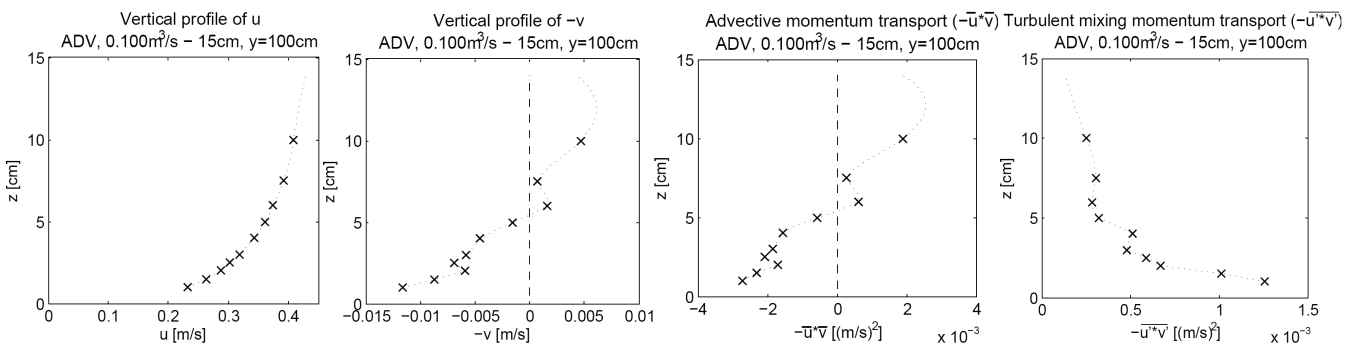

Figure 27: vertical profiles of longitudinal velocity (most left), transverse velocity (second left), momentum exchange by advection (third left) and momentum exchange by turbulent mixing (most right); all measured were taken with an ADV in 0.100m³/s - 15cm. Data is extrapolated using a cubic extrapolation up to the water surface.

31

Figure 28 compares the transverse momentum exchange for both mechanisms as a function of the lateral position. First of all, these results show that the contribution to the momentum exchange is for both mechanisms in the same order of magnitude. Secondly, the advection of momentum slightly dominates above the smooth side of the flume; whereas the momentum exchange by turbulent mixing peaks right above the interface and is therefore the dominant mechanism above the rough side.
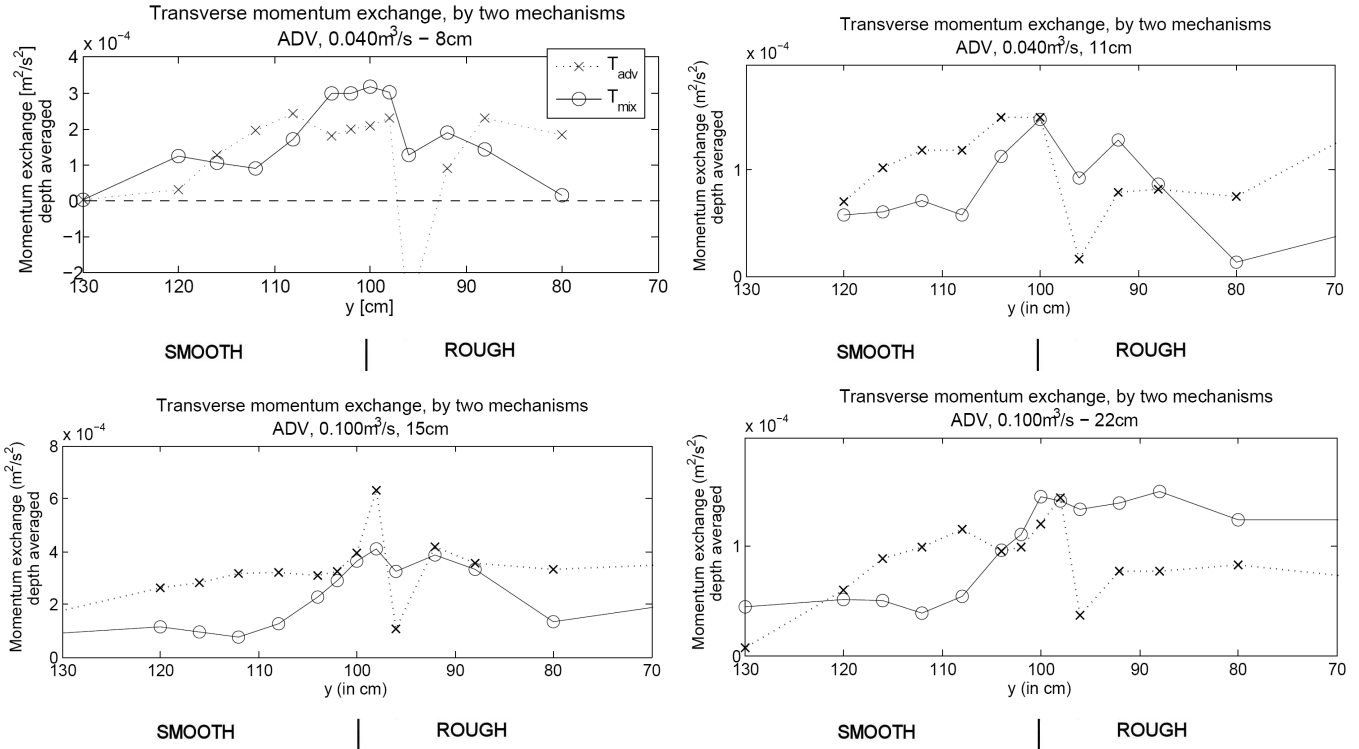

Figure 28: Momentum exchange by advection vs. shear stress, based on ADV measurements. Data was extrapolated to the surface and corrected to obtain continuity (according to equation 16).

All momentum exchange over the smooth-to-rough interface supports extra effective friction of the flow as a whole. Considering the momentum exchange at y=100 cm, the advection appears to become more important at scenarios using larger depths, with a maximum around 15 cm depth ($h/k_s = 8$). This relation is illustrated in the left panel of figure 29.

This ADV data suggests that for a depth of 22 cm the relative contribution of advective transport decreases again. However, it is very well possible that the flow was not completely developed for this case (explained in the discussion) and it is therefore expected that this advective momentum exchange is underestimated. Based on theory, an increasing contribution can be expected since turbulent mixing is at maximum close to the bottom (Nezu & Nakagawa, 1993 and figure 26). Results from the LES (with much longer development length) give ground for this explanation (figure 29, right panel); the relative importance of advective momentum exchange is largest at a 22 cm situation according to the LES results.

The overall higher ratio in figure 29 in the LES results compared to the ADV results is partly caused by the not fully developed flow situation in the flume experiment. Besides that, the direct shear stress is systematically lower in LES compared to the ADV-measurements. As said, this is due to two factors; the $\overline{u'v'}$ is measured too high by using

the ADV and underestimated in the LES. Consequently, the advective transport has a smaller contribution in momentum exchange based on the ADV-measurements than based on the LES. The actual situation will be in between these results.

In conclusion it can be said that the transverse momentum transport by advection is generally somewhat larger (but in the same order of magnitude) as by turbulent mixing ($\overline{u'v'}$). Figure 29 suggest an increased relative importance of transverse momentum transport by advection for larger depths (i.e. smaller relative roughness) and smaller velocity (gradients). This is in contrast with a hypothesis stated by Studerus (1982).
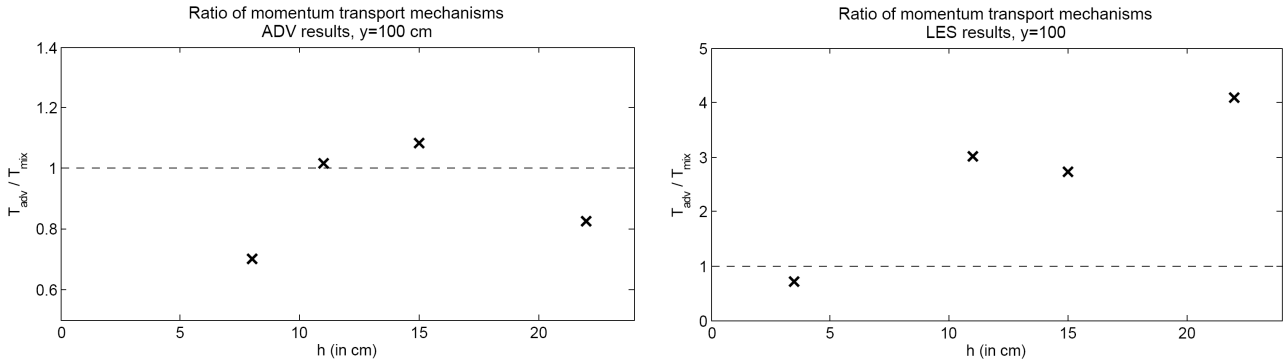

Figure 29: Ratio of advective momentum exchange with respect to turbulent shear stress momentum exchange, as measured by using the ADV at the smooth-to-rough interface.

Effective friction

Effective friction is important for the implementation of bed friction in case of heterogeneous roughness (such as in floodplains). To test the approach of equation 8, the actual effective friction is calculated based on the water level slope.

Figure 30 shows the water level profiles for all scenarios. The water level is decreasing fairly linearly, only the most downstream measurements (about 10 meters before the weir) is increasing in some cases, probably influenced by a backwater effect. This was also observed in earlier research in the same experiment flume (Jarquín, 2007). For the slope calculation, done by linear regression, the measurements after 8 meters are not taken into account.

Table 3 shows the slopes of the fitted lines as in figure 30. The estimated errors of the fitted slopes are quite small, as the 95% confidence range is small compared with the slopes itself. Using the average slopes, the average velocity and the hydraulic radius, the effective friction factors are calculated according to the Darcy-Weisbach equation (equation 1); see table 3.

Table 3: Water level slopes and corresponding friction factor for all parallel measured setups.

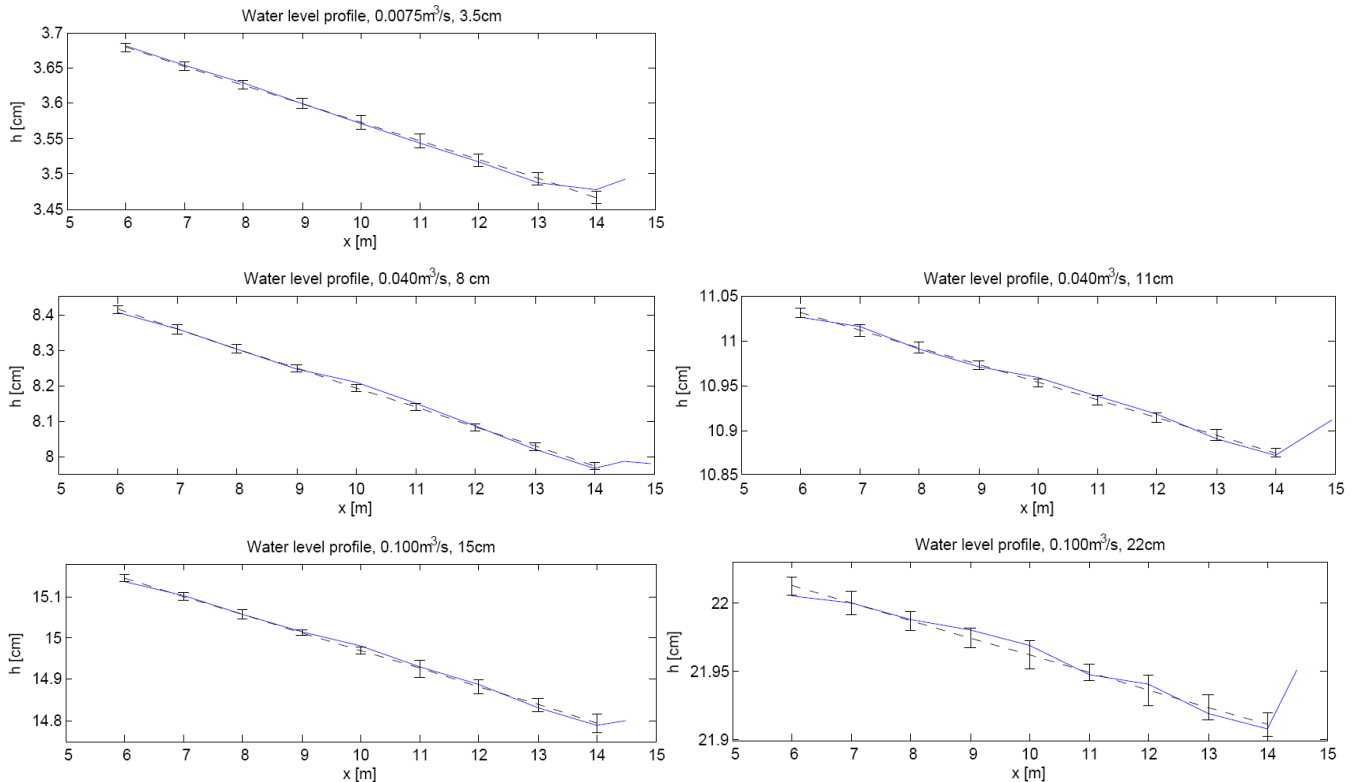| Q (m^3/s)	h (cm, at x=3 m)	$\overline{u}$ (m/s)	$\overline{S}$ (mm/m)	95% confidence range (mm/m)	Re	$f_{eff, meas}$	$k_{s, measured}$
0.0075	3.5	0.110	0.266	0.015	3436	0.056	0.0017
0.040	8.2	0.244	0.549	0.029	17514	0.055	0.0063
0.040	11.0	0.182	0.197	0.014	17072	0.046	0.0049
0.100	15.1	0.331	0.437	0.021	41160	0.041	0.0051
0.100	22.1	0.219	0.126	0.018	38579	0.038	0.0055

Figure 30: Water level profiles as measured with the electronic gauge for all scenarios for a developed parallel flow (x = 0m at the start of the parallel split). The solid line represent measurements, the broken line is a linear fit. The error bars, added to the fitted water level profiles, are composed of standard deviations in the duplo measurements, those in the duplo's of the correction measurements and the estimated error of the fit.

An assumption for the effective roughness calculation is that the slopes are equal at the rough and smooth part (in the full developed region). The electronic gauge was measuring the water level above the rough part; the manual gauge above the smooth part. These slopes were similar, but to further check that no transverse slopes exist, this slope is measured by using the manual gauge. Figure 31 shows the corrected result. There's no clear pattern and the changes are within the measurement accuracy (0.1mm). So, with a measurement uncertainty of 0.1mm it is concluded that no significant transverse slope is apparent.
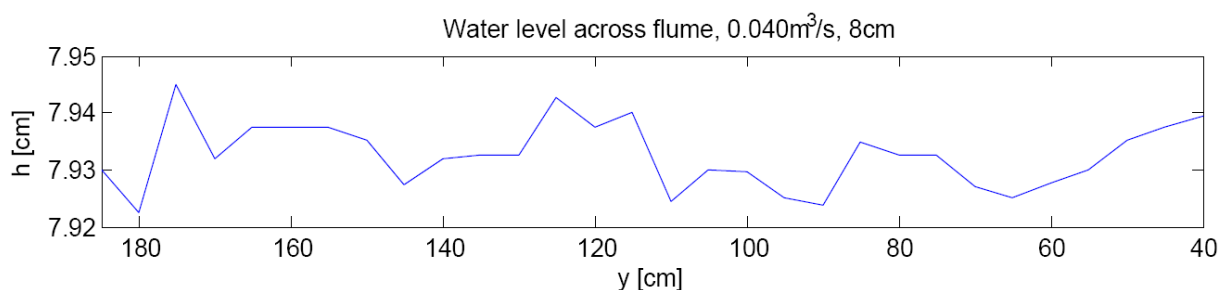

Figure 31: Water level across the flume, measured by a manual gauge at the carriage, for 40lps – 8cm depth, in a developed flow (x=12.5m). The reference profile for the gauge is based on still water.

34

The theoretical effective friction factor can be calculated by using equation 8 based on the individual friction factors for the rough and smooth part. To anticipate several discharge and depth situations, the individual friction factors were derived by using the Nikuradse roughness height (k_s) for the individual bed compositions. The values for k_s were in turn determined by using homogeneous cases with several depths. Measurements of Jarquín (2007) were used for the calculation of k_s of the rough part; the smooth part was assumed hydraulically smooth. Appendix C shows the calculation and values for k_s. In this calculation a correction was applied for the reference level of the carriage, which enhances the outcome for k_s. This correction was not applied by Jarquín (2007).

Hence, table 4 shows the theoretical effective friction factor in comparison with the measured effective friction factor. These values show that the actual effective friction factor is 16-29% higher than its theoretical equivalent, except for the very shallow (3.5cm) case. The absence of a pronounced secondary circulation in this shallowest case (and hence less momentum exchange) explains that the actual friction is relatively lower than in the other cases. However, it is unexpected that the actual friction is even lower than the theoretical. This phenomenon could be explained by an overestimating of k_s, which is only plausible for this shallow case since the homogeneous rough measurements were all executed in water depths of at least 13.5cm. Hence the individual value for k_s is a strong extrapolation for the case of 3.5cm depth and therefore less reliable than for the other depth situations.

Except for the shallowest case, the increase in effective friction is not significant related to the depth and the Reynolds number (and hence also not clearly dependent on the relative roughness and friction factor itself).

Table 4: comparison of friction factors based on roughness properties of individual sections ($f_{eq, theory}$) and measured equivalents ($f_{eq, measured}$)

Q (m^3/s)	h (cm, at x=8m)	Theoretical values, based on individual sections				$f_{eff measured}$	$f_{eff, measured}$ / $f_{eff, theory}$
		$k_{s, rough}$	f_{rough}	f_{smooth}	$f_{eff, theory}$		
0.0075	3.5	0.018	0.139	0.042	0.070	0.056	0.88
0.040	8.2	0.015	0.078	0.027	0.043	0.055	1.29
0.040	11.0	0.014	0.066	0.027	0.040	0.046	1.16
0.100	15.1	0.011	0.054	0.022	0.033	0.041	1.26
0.100	22.4	0.008	0.041	0.022	0.029	0.038	1.23

The LES results show also a larger effective friction than its theoretical equivalent, but only in a 8% difference (in case of 0.100m^3/s, 15cm depth). This discrepancy can have three reasons:

- *Overestimating the friction coefficient in the laboratory experiment due to acceleration of the flow.* The bottom of the experimental flume is horizontal whereas the water level is slightly decreasing. Therefore the flow accelerates and enhances the water level slope even more. To establish the importance of this effect, the equation of motion is studied. For cross-section integrated, steady conditions, this equation reads:

$$g \cdot \frac{\partial h}{\partial x} - \frac{\tau_b}{\rho \cdot h} + u \cdot \frac{\partial u}{\partial x} = 0 \qquad \text{(equation 18)}$$

In which the last term (on the LHS) represents the acceleration. For small changes in depth, this term can be rewritten (due to continuity of mass):

$$g \cdot \frac{\partial h}{\partial x} - \frac{\tau_b}{\rho \cdot h} + u \cdot \frac{-u}{h} \frac{\partial h}{\partial x} = 0 \qquad \text{(equation 19)}$$

This demonstrates that the water level slope is increased due to the acceleration term. The relative importance of the acceleration term with respect to the pressure gradient term can be expressed as:

$$\frac{\left(\frac{u^2}{h} \cdot \frac{\partial h}{\partial x} \right)}{\left(g \cdot \frac{\partial h}{\partial x} \right)} = \frac{u^2}{g \cdot h} \equiv Fr^2 \qquad \text{(equation 20)}$$

Using the overall Froude numbers of each case, the acceleration effect increases the water level slope about 3% (for the 3.5cm, 11cm and 22cm cases) up to 8% (for the 8cm and 15cm cases).

On the other hand, the effect of acceleration also occurred during the measurement of the individual friction factors (in the homogeneous situations). Therefore the effect is expected to be very small, probably negligible on the average ratio between the measured and theoretical effective friction factor. So, this can not explain the difference between the average increase of effective friction in the measurements (over 20%) and the equivalent results from the LES (8%). However, this effect can be recognized in the individual cases: the cases with the highest Froude number (8cm and 15cm) have the largest increase in effective friction.

- *Underestimating the transverse momentum exchange and transverse bed friction in the LES very close to the bottom.* The turbulent transverse momentum exchange (T_{mix}) is much smaller than measured in the experiments, partly due to the underestimation of the shear stresses in the LES-results (see appendix B). Also the shear stress in transverse direction ($-\rho \cdot \overline{v'w'}$) is highly underestimated in the LES since the roughness effect on the turbulence profiles are not properly incorporated in the LES. Therefore the effective friction factor in a flow over a parallel rough bottom can be underestimated in the LES.

- *Measurement errors in the laboratory experiments.* All measurements are subject to some measurement errors. The errors in the water level slopes for the parallel cases are rather small; table 3 shows that the 95% confidence interval is reached at ca. 5% deviation of S. The measurement error in the individual friction factor for the rough section are probably larger (a smaller measurement section was used),

but is reduced again by taking an average value of 6 cases. Finally, the smooth section could be locally rough (at the seams) and could therefore have a higher friction factor than calculated. This effect is considered largest of all measurement errors; using k_s=0.00055m (average value from literature for wood) in stead of k_s=0 the theoretical effective friction factor is increased by 5-10%.

In conclusion: small errors, in the measured as well as in the modelled results, provide an explanation for the discrepancy between the measured and modelled effective friction factor. The actual values for the increase in effective friction due to the mixing layer are in between the results from ADV and LES. Therefore, the best estimate will be that the mixing layer in the case with parallel roughness is responsible for an increase in effective friction of 15-20%.

Based on the uncorrected data of Jarquín even higher actual effective friction was reported (20-80% by Jarquín, 2007; 80% by Vermaas et al, 2008). These preliminary outcomes can be qualified now to be less reliable due to uncorrected measurement errors in the water level slopes.

Recommendations for 1D and 2D modelling

The LES mimics the laboratory experiments reasonably well. For a practical situation of a large scale river, it would be impossible to simulate the flow with such detail; both by computational limits as well by unknown boundary conditions. Therefore, the effects of heterogeneous roughness must be parameterized and implemented in 1D and 2D models.

For a 1D model, the most straightforward method to account for heterogeneous roughness is to increase the effective friction factor by 15-20% in comparison to the value expected based on the individual friction factors. The laboratory experiments were consistent in these results for k_s/h ratios between 0.09 and 0.24 (following a constant k_s = 19mm). This relation is unclear for very large k_s/h ratio, but it seems that no significant increase in effective friction with respect to equation 8 occurs for this situation.

A horizontal 2D (xy) model (such as WAQUA) could represent the depth averaged velocity profile in transverse direction. As an example, a simple model, initiated by Bram van Prooijen, was used to iteratively calculate the cross velocity profile using a distinct bed roughness and using a turbulent viscosity for the transverse momentum exchange. Figure 33 schematizes the algorithm for this calculation. Initially, an abrupt change (step profile) in roughness was set by means of the friction coefficient (c_f) [3]. The turbulent viscosity was calculated by an approximation as suggested Van Prooijen (2004), based on a bottom turbulence part (Nezu & Nakagawa, 1993, p90) and a contribution due to transverse shear:

$$\nu_{turb} = \frac{\kappa}{6} \cdot \sqrt{c_f} \cdot U \cdot h + \beta^2 \cdot \delta^2 \cdot \left| \frac{\partial U}{\partial y} \right| \qquad \text{(equation 21)}$$

---

[3] The friction coefficient can be converted to a Darcy and Chezy friction parameter by: $c_f = f/8 = g/C^2$

In which β is a constant (chosen to be 0.10 for this case) and δ is the mixing layer width, defined as twice the width between the 75%- and 25%-values of the longitudinal velocity in the mixing layer; see figure 32.
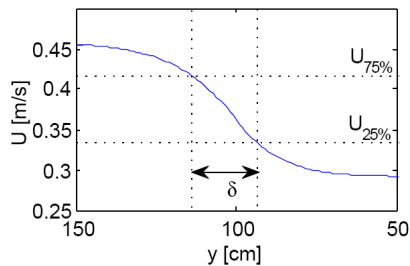

Figure 32: Definition of mixing layer width based on the 75% and 25% values in the longitudinal velocity profile. The mixing layer is defined twice the lateral distance between the intersections of $U_{75\%}$ and $U_{25\%}$: $\delta = 2 \cdot \left(y_{75\%} - y_{25\%} \right)$

The values for c_f and water slope gradient are copied from the measurements of the 15cm case. The depth was adjusted such that to result in an initial discharge of 0.100m³/s (therefore slightly different from 15cm since the hydraulic radius was used in the Colebrook-White equation).
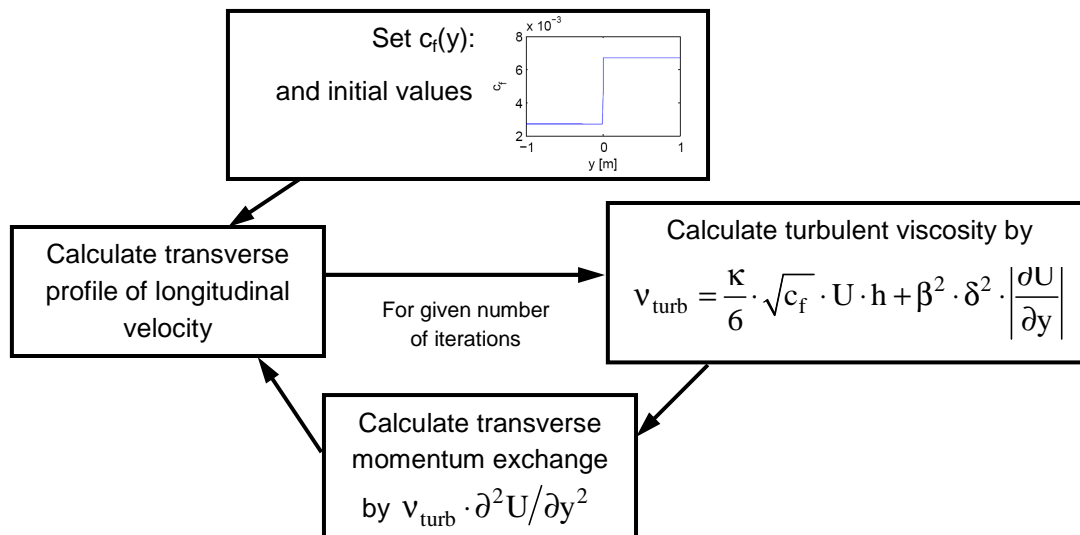
Figure 33: algorithm for calculating a depth averaged velocity profile in flow over parallel roughness

Figure 34 shows the results. In the first time step, no transverse momentum exchange has occurred. In this case, the effective roughness is given by equation 8. After sufficient time steps, a mixing layer has been established and the discharge is reduced due to transverse momentum exchange. The velocity profile is in rather good agreement with the profiles deduced from the measurements. However, figure 34 shows that the reduction of discharge after transverse momentum exchange is only about 0.8%, i.e. much milder than shown by the experiments (9.5% decrease in discharge at 20% extra friction). One could increase the values for the turbulent viscosity for a stronger decrease in the discharge after iterations, but to reduce the discharge with 9.5%, the turbulent viscosity must be strongly increased. Consequently, this would lead to incorrect velocity profiles. Therefore, to understand the deficiency of this model, the functions for the friction coefficient and turbulent viscosity must be revised.

Figure 35 shows the profiles for c_f as derived from the ADV-data and modelled by the LES. It appears that especially the experimental friction coefficient is slightly larger around the smooth-rough interface with respect to a step profile. This is implemented in the depth averaged model by adding a Gaussian function to the step profile, such that the pattern of the c_f derived from ADV-results are well represented.

Figure 36 shows values for the viscosity that parameterizes the transverse momentum transport. First of all, these values are an order of magnitude larger than estimated by equation 21. Secondly, the viscosity as shown by figure 36 has minimum values at the interface (y=100cm) and higher values 10-20 cm next to the interface. The secondary circulation can explain the higher turbulent viscosity at the smooth side; the length scale involved in this secondary circulation is larger than that in turbulent mixing layer vortices. As consequence, the effective turbulent viscosity is increased at the smooth side of the interface. The high effective turbulent viscosity at the other side can be caused by a dispersion of mixing layer vortices, which would also contribute to the observed minimum above the interface. The new turbulent viscosity profile (pattern and values) can be enforced in the depth averaged model.
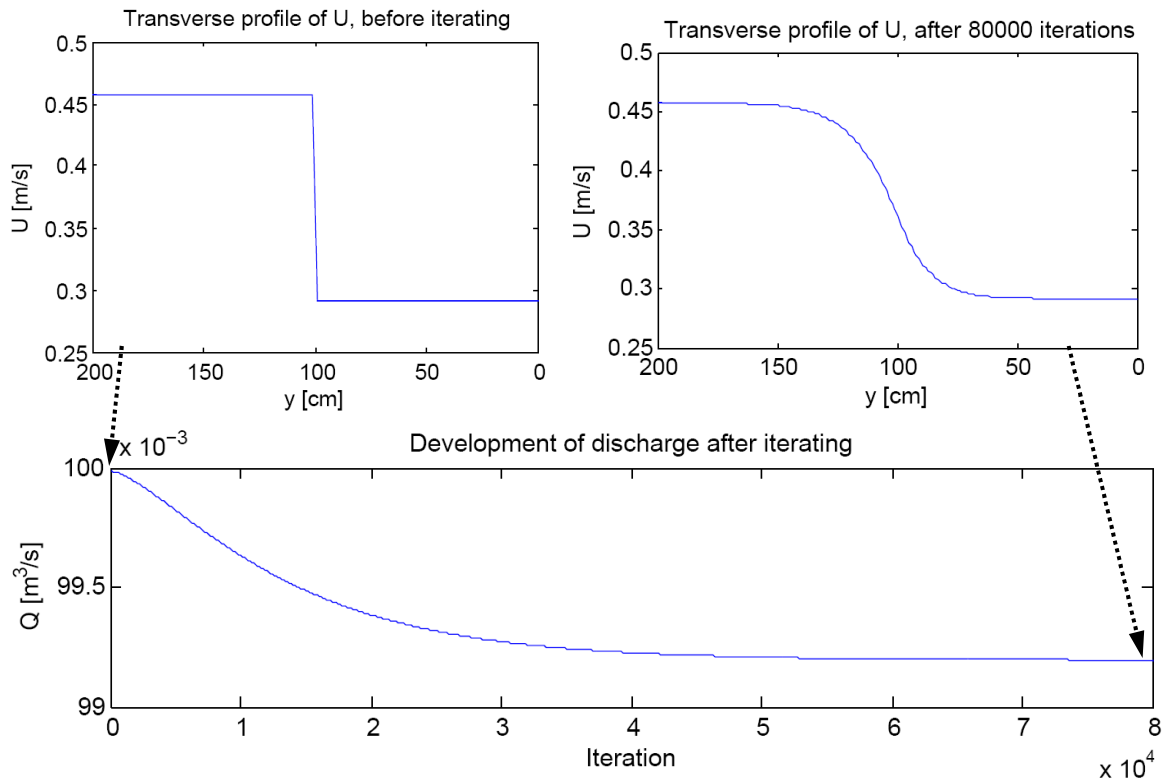

Figure 34: Resulting velocity profiles (upper panels) before and after iterating. The lower panel shows the discharge as function of the number of iterations, approaching an equilibrium value.
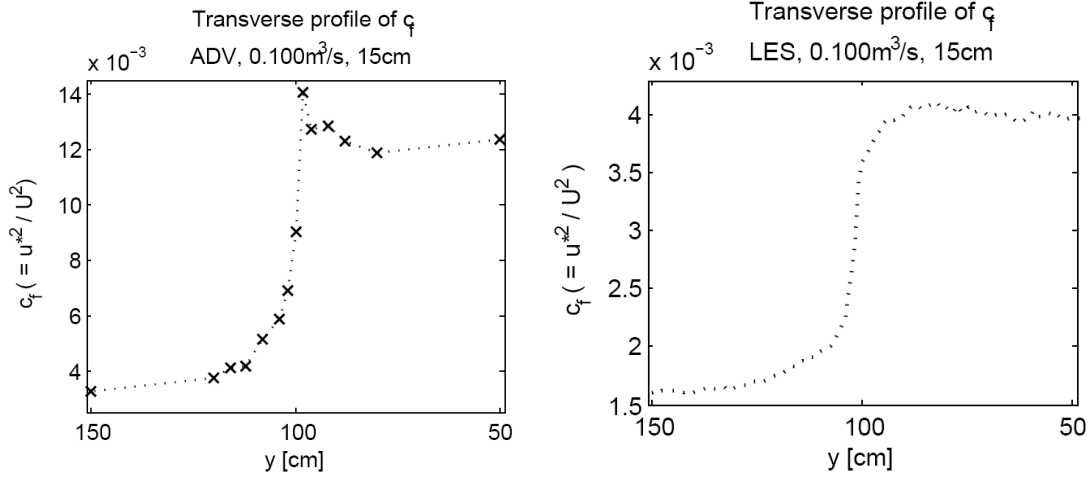
Figure 35: Transverse profiles of friction coefficient, for ADV-measurements (left) and LES-results (right). Both derived from data of in the 15cm-case.
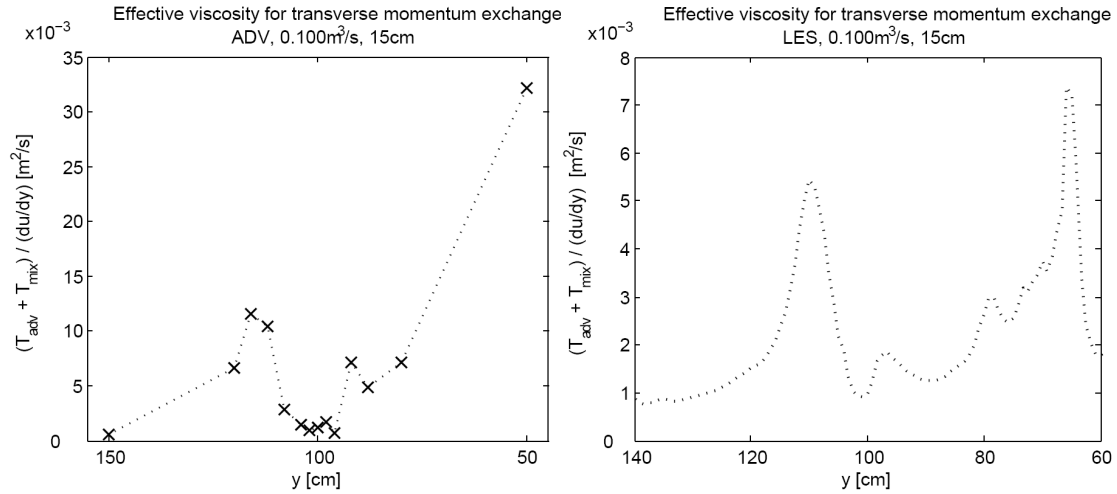

Figure 36: effective viscosity for transverse momentum exchange, derived by dividing the total transverse momentum transport by the shear $\partial U / \partial y$. This shear was slightly smoothened by a linear loess filter to avoid extreme values in viscosity. The left panel shows the ADV-results, the right panel the LES-results, both from the 15cm-case.

Figure 37 shows the results with new functions for c_f and v_{turb}. Both profiles are fixed, so the iterative calculation of v_{turb} can be skipped. Although the discharge is more reduced (almost 5%) in comparison with the initial calculation, it is still less than in the experimental result. Moreover, the mixing layer in the resulting velocity profile is too wide compared to the measurements. Apparently another mechanism is left out of consideration in the depth averaging. For instance, the secondary circulation and extra turbulence production at the interface produces bed shear stress in transverse direction and thus extra effective friction. This extra transverse bed shear stress was not apparent in the homogeneous case since no secondary circulation and parallel interface was involved in that case.
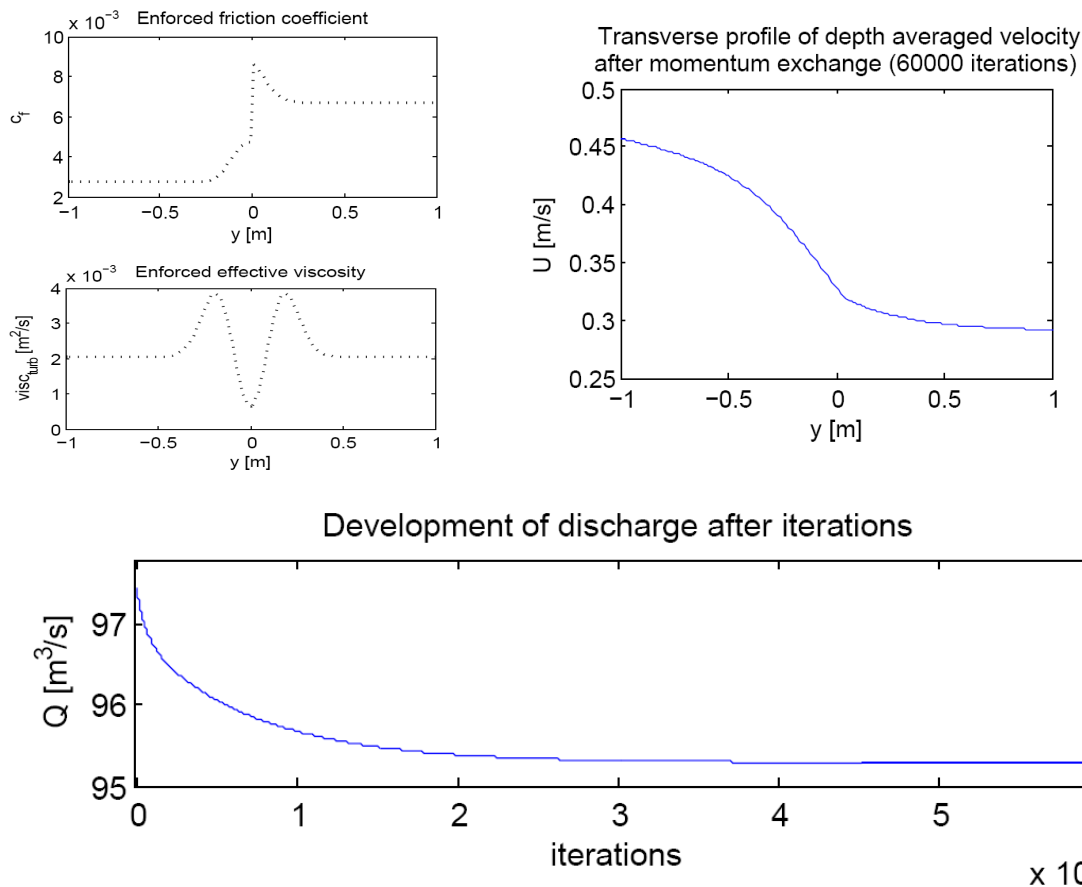
Figure 37: Left upper panels: enforced functions for c_f and ν_{turb}. Upper right panel: resulting velocity profile after iterating. The lower panel shows the discharge as function of the number of iterations, approaching an equilibrium value. The pressure gradient was kept equal to the first situation, so the discharge was eventually reduced by almost 5% compared to the initial block velocity profile.

The only conclusion suitable after this analysis is that the depth averaged velocity can not represent the velocity profile as well the discharge without adding extra stress to the flow. So, the best way to model a flow over parallel rough bottoms in a 2D (xy) model is to increase the values for the friction coefficient (with 10-15%) on top of the existing function for c_f. This extra stress will reduce the total discharge and gives a better agreement with the actual situation.

In conclusion, this analysis leads to the following three recommendations for 2D modelling:

- For the pattern of the bed friction parameter: in addition to a step function, the friction parameter must be increased around the parallel interface.

- The overall magnitude of the friction parameter should be increased by 10-15%.

- The effective turbulent viscosity is an order of magnitude larger than calculated by equation 21 and must have a maximum at about 1 water depth next the parallel interface. If no spatial function for the turbulent viscosity can be enforced (as in WAQUA), an average value for the effective turbulent viscosity is acceptable.

41

4)   Results of developing parallel flow

In the last chapter it was shown that a developed flow over a parallel rough bed has distinct characteristics from a uniform flow. It was also shown that at the deepest situation (22cm), the flow was not fully developed yet. In practical situations, parallel roughness sections are not infinitely long. An undeveloped flow over a parallel rough bed is probably more usual than its developed situation and is therefore of great importance. In this chapter, the length scales of development, for the time-averaged flow and shear stresses are investigated. This case is not modelled by the LES; only flume measurements are performed.

Development of velocity profiles

In the change from a uniform to a parallel bed roughness, three processes can be distinguished:

- the volume transport from the rough to the smooth side

- the adaptation of the vertical profiles of velocity and stress to the new bed roughness (i.e. a serial bed roughness change)

- the development of a mixing layer and its accompanying secondary circulation around the smooth-rough interface (a parallel bed roughness change)

These three processes are of course related to each other, but will be treated individual in three paragraphs below.

Transverse volume transport

The transverse velocity over the interface can be primarily scaled on the width of the flume, not on the depth. This is because the transported volume is linearly increasing with the width of the smooth and rough section. Indirectly the depth plays a role since a lower depth gives a higher relative roughness, with a larger difference in longitudinal velocity as a consequence. It follows from this effect that an increasing depth has even a consequential slightly decreasing length scale for the transverse volume transport.

Figure 38 shows the depth averaged transverse velocity (=V) as function of x, in which it can be seen that the transverse flow is indeed only weakly dependent on the depth (and strongest at shallowest depth). The transverse volume transport has already a maximum at the start of the parallel rough setting. At x=4m, i.e. twice the width, most of the water appears to be redistributed over the smooth and rough section.
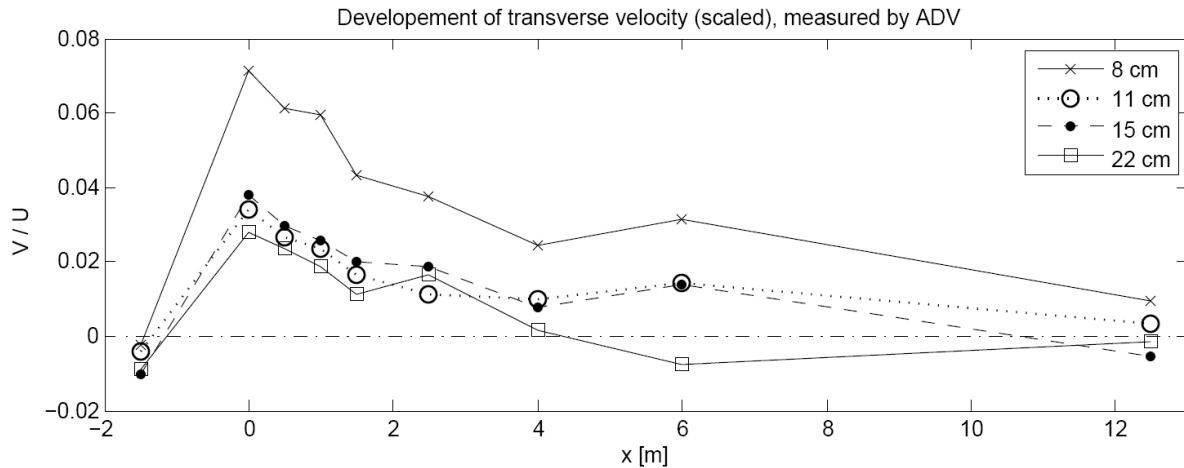
Figure 38: Development of V, scaled on the average longitudinal velocity U. Data was gathered by using the ADV (measuring 4 points in vertical) and linear extrapolated towards the surface.

A two-dimensional (xy) image of the transverse velocities confirms this observation (figure 39): The bulk of the water is transported transversally within 4 meters. This figure also shows again that the transverse volume transport is larger for shallow depth cases.

The transverse transport has a maximum at the start of the parallel smooth-rough configuration. One could conclude that a transverse water level slope must be present at the start of the parallel bed. This effect is confined to less than 1 flume width in upstream direction, since no transverse transport was measured at x=-1.5m.
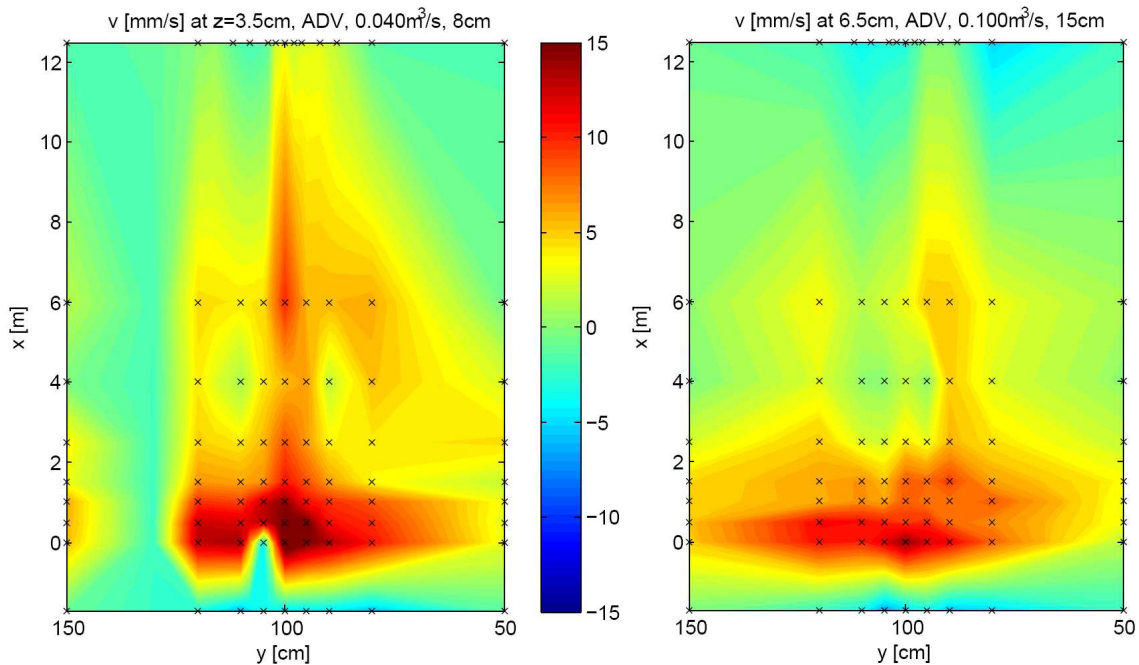

Figure 39: Transverse velocities (v) around middle depth for two cases. The crosses indicate the ADV-measurement locations. Linear interpolation used.

43

Velocity profile development outside mixing layer

At the start of the parallel rough bed, the flow at the rough side of the flume is subject to an increased friction. A serial roughness change over the full width is thoroughly investigated, but in this case the bed roughness is only changed for one side of the flume. The arising volume transport as explained above causes the discharge to be redistributed over the width. The depth averaged velocity above the smooth side is accelerated; above the rough side decelerated. This might have an effect on the development length scale for the velocity compared to a serial roughness change over the full width.

The direct influence of the mixing layer is left out of consideration in this paragraph; only the streamwise development of the flow properties above the rough side is studied. To give a good indication of the development length scale, vertical profiles of velocity as well as the turbulent shear stress at y=50cm are examined. This length scale concerns the measurement range of the ADV; the velocity at the surface will require a longer development length.

Figure 40 shows the turbulent shear stress profiles above the rough section. The shear stress profiles become fairly linear after about 25 times the water depth. The profile might have deviations again further downstream, but that can be due to local irregularities. This length scale is very similar to cases with a sudden roughness change over the full width (e.g. Nezu & Nakagawa, 1991).
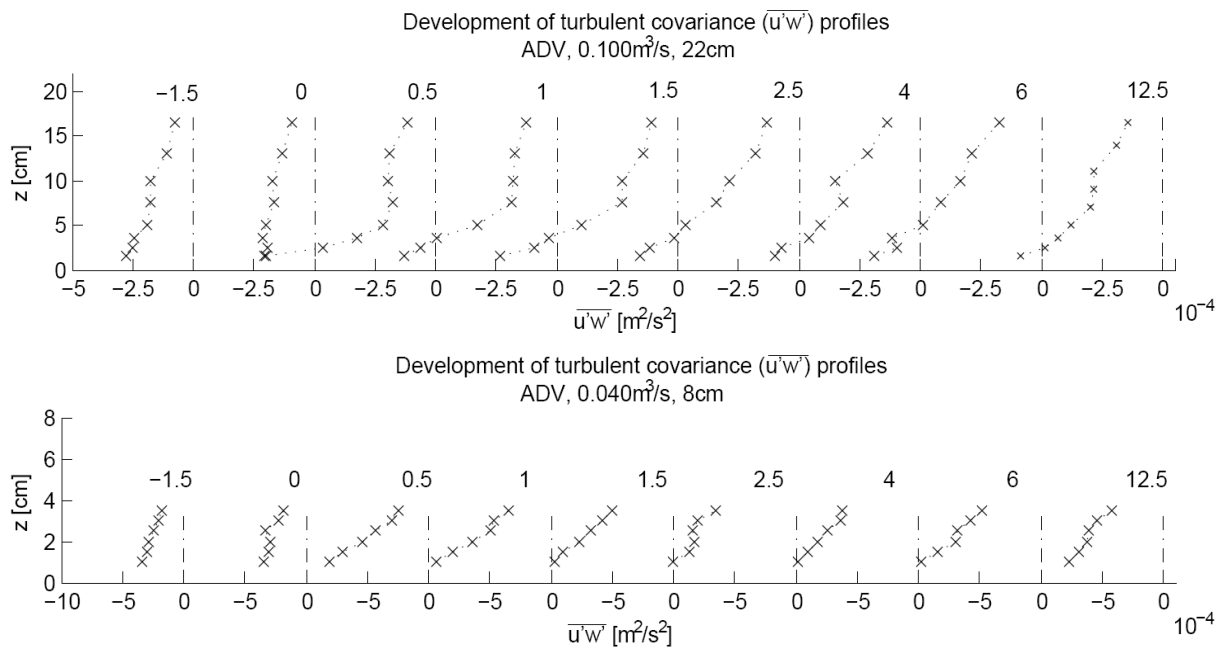

Figure 40: Vertical profiles of turbulent covariance at y=50cm, ADV measurements of two cases are shown. Corresponding labels refer to the x-coordinate [m]. Profiles are shifted $5 \cdot 10^{-4}$ (upper panel) and $10 \cdot 10^{-4}$ m^2/s^2 (lower panel) to each other. The profiles for the 8cm case (lower panel) become fairly linear at x=1.5m, for the 22cm case not earlier than at x=6m.

When studying the time-averaged velocity profiles, this length scale can be confirmed. All profiles above the rough bed are found to be logarithmic (with $R^2>0.98$), see figure 41. Only a slight deformation is visible in the profiles, shifting slowly to the surface with increasing x. As an objective measure for the development length the parameters for the logarithmic profile are studied as function of x. Figure 42 shows these functions. The

characteristic parameters (z_0 and u*) increase just after the start of the rough section to subsequently meet a lower and more or less stable value. It appears that the length scale for development is not clearly dependent of the water depth. The scaling on the depth might be cancelled out by the fact that the relative roughness change is smaller for larger water depths (Townsend, 1966). The parameter values point out that the best estimate for a length scale of adaptation is 4-6 meter (15-40 water depths), i.e. 200-300 times k_s.
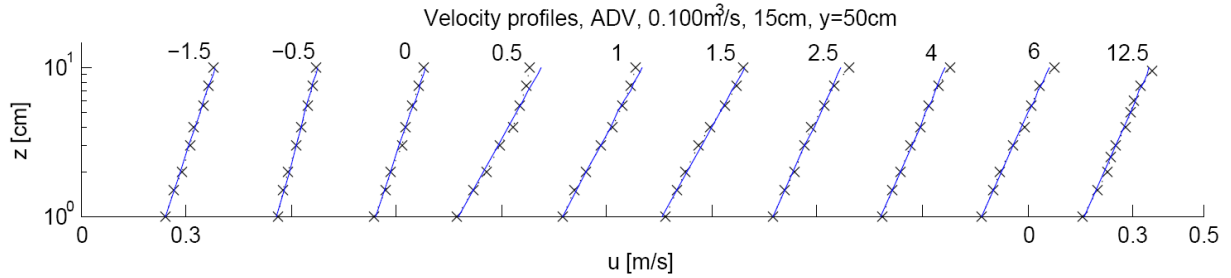
Figure 41: Vertical profiles of longitudinal velocity, above rough side (y=50cm), measured by using the ADV (crosses) and fitted to the law of the wall (solid line). The labels refer to the x-coordinate [m]. Logarithmic scale in vertical; consecutive profiles are shifted 0.3m/s.
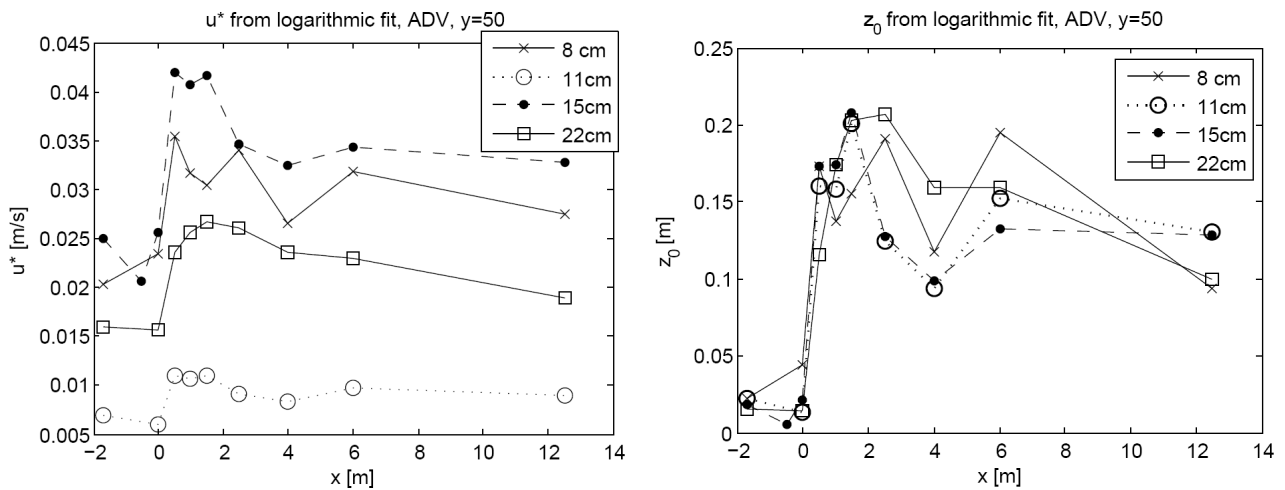

Figure 42: Parameter values from the logarithmic fit, measured by using the ADV, above the rough side (y=50cm). The parallel bed roughness starts at x=0m.

In addition to the former analysis, the turbulent kinetic energy k can be analyzed. Figure 43 shows the distribution of k above the rough undeveloped side. This figure clearly illustrates the growth of the boundary layer corresponding to the rough bed. After 4 meter, the turbulent kinetic energy profile is in balance with the rough bed up to the measurement range (10cm).

45

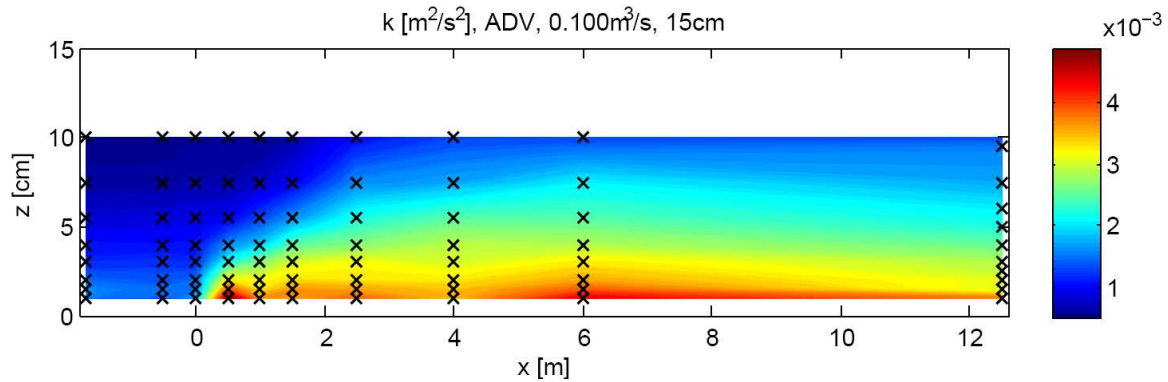*Figure 43: Development of turbulent kinetic energy at y=50cm, based on ADV-measurements, positioned at locations of black crosses.*

Mixing layer development

The development of the mixing layer starts as soon as a velocity difference is apparent between the rough and the smooth section (i.e. even before the start of the parallel roughness), but keeps adjusting as long as the discharge redistributes over the smooth and rough section. The length scale for the fully developed mixing layer must be longer than the length scale for the transverse volume transport. The length scale for the mixing layer development is strongly dependent on the depth; figure 19 already showed that a larger depth causes a less well developed mixing layer. Van Prooijen (2004) showed that the development of mixing layers as a result of an initial velocity difference can be scaled on h/f. The width of such mixing layers was also scaled on h/f (Van Prooijen, 2004, p.30).
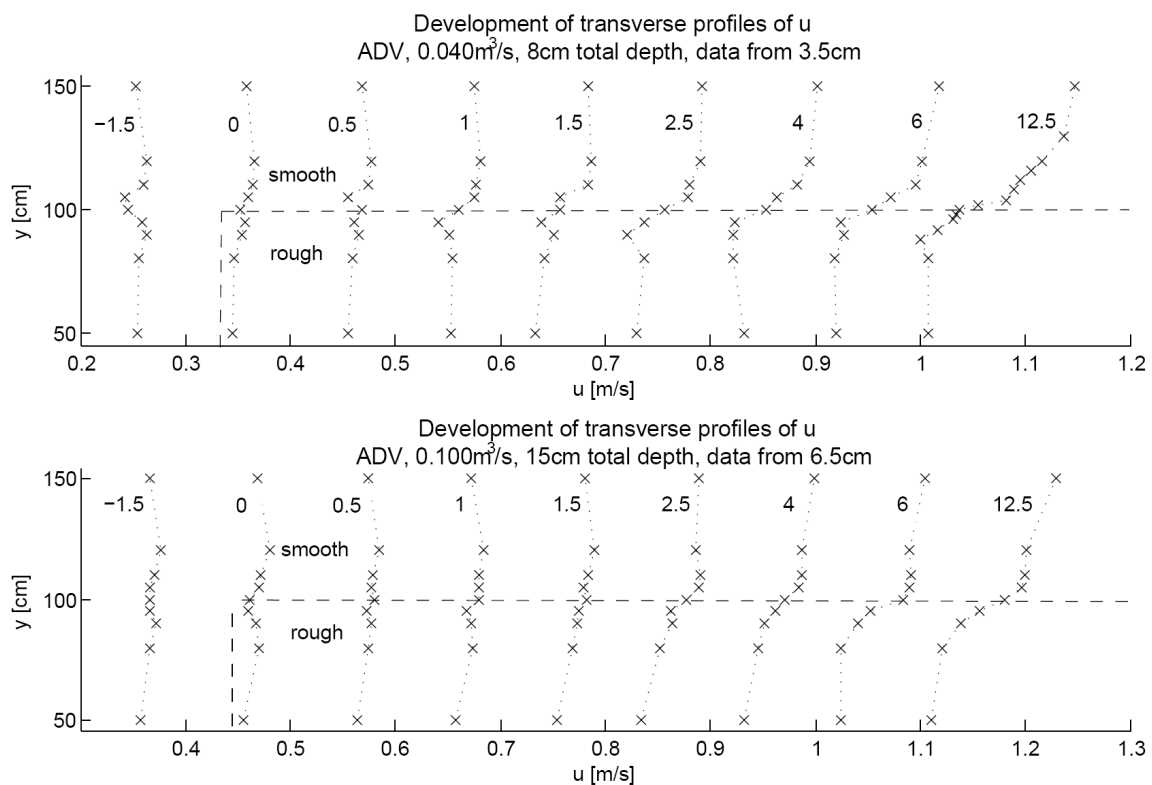

Figure 44: Development of u in transverse profiles, ADV measurement of 2 cases shown. Data from only 1 depth is used since the development is not equal at all depths. The labels refer to the x-coordinate [m]. Subsequent profiles are shifted 0.1 m/s.

46

Figure 44 shows consecutive transverse profiles of longitudinal velocity, measured by using an ADV. Despite the formation of a distinct mixing layer at x=4m, the profiles at x=6 and x=12.5m are still significantly different in absolute values for all cases. It is hard to define a strict length scale for development; a rough estimate would be that after 50 water depths from the start (e.g. 4 m for 8cm depth, 6m for 11cm) the mixing layer is reasonably well developed.

For another check on the development length of the mixing layer, the bed shear stress development is shown in figure 45. The peak in bed shear stress seams to be larger in the developed profile, but at this y-coordinate was no data available for the other profiles. The comparable data points show that the bed shear stress at x=4m is similar to the developed situation (x=12.5m). This seems to be rather independent of the total depth, however too few cross sections are made to prove this statement.

Physically it would make sense that the flow in vicinity of the bottom adapts rather independent of the total depth. The length scale for developing the mixing layer consists of a width dependent part (due to the transverse volume transport) and a depth dependent part (for adopting velocity to new roughness). Since the flow is first adapted to this new roughness near the bottom, the depth dependent part is relatively small close to the bottom. The velocity at higher levels will have a larger depth dependency, as for instance shown in figure 19.
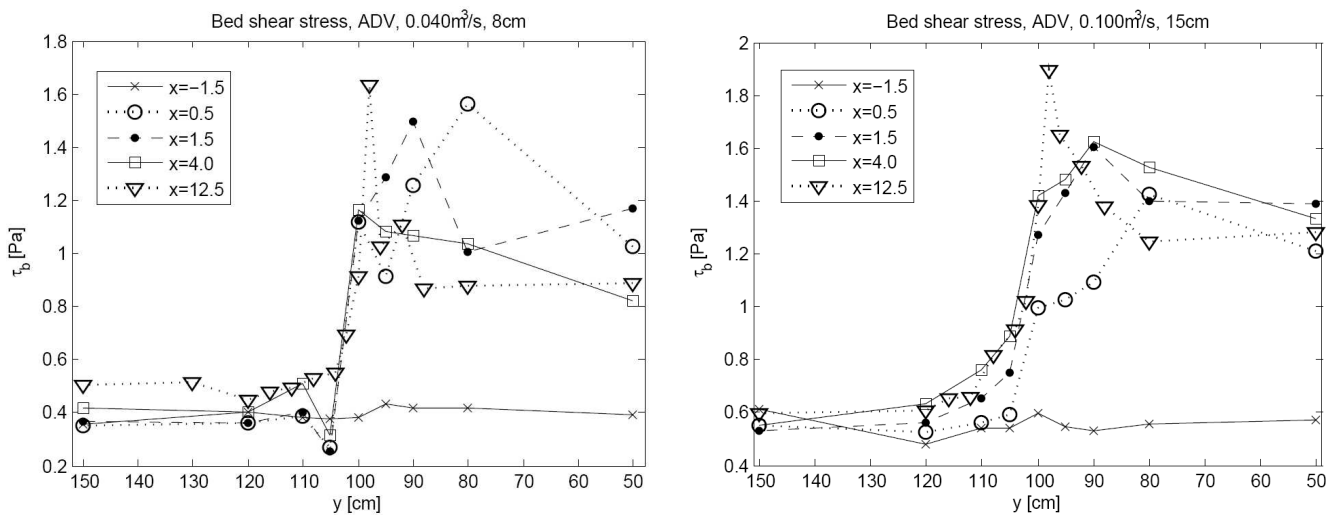

Figure 45: Bed shear stress in consecutive cross sections, measured by using an ADV for two cases. The bed shear stress was determined by linearly fitting vertical profiles of $u'\cdot w'$.

This also has its resemblance in the development of the secondary circulation. Figure 46 shows two cross sections at x=4m as measured by using the ADV; a (weak) secondary circulation is already present in these quiver plots. At x=1.5m the transverse volume transport is by far dominant over the secondary circulation. After subtracting the average transverse flow, some very weak traces of a secondary circulation could be seen even at this stage (not shown).

Although the secondary circulation is already present at x=4m, the circulation is not fully developed yet. Figure 47 shows the transverse velocity at the smooth-rough interface. The contour lines of equal velocity (isotachs) are not yet horizontally at between x=6 and x=12.5m, which indicates that the transverse volume transport still occurs and therefore

the secondary circulation is still developing between 6 and 12.5 meter. Moreover, as mentioned before, the secondary circulation is probably not at full strength at x=12.5m in the case of 22cm depth. By supposing the secondary circulation in the 15cm case as fully developed after 12.5 meter (based on figure 29 and figure 19) the secondary circulation requires about 80 times the water depth for a full development, counting from the start of the parallel bed.
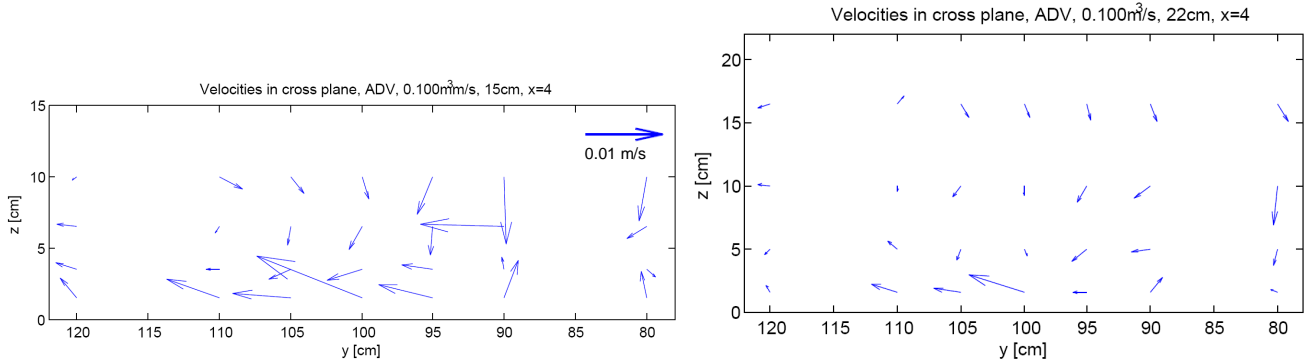

Figure 46: Velocity vectors in a cross section (view in flow direction) at x =4m for two cases.
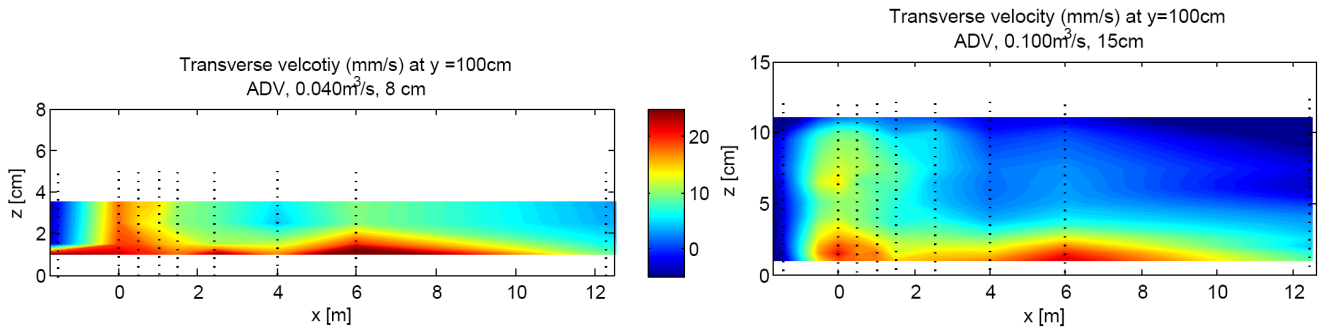

Figure 47: Transverse velocity at smooth-rough interface (y=100cm) for two cases. The dotted lines indicate the measurement positions. Linear interpolation used.

Development of momentum exchange

In the developed case, at x=12.5m, the turbulent mixing ($\overline{u'v'}$) appeared to account for about half of the net momentum exchange in the mixing layer. The secondary circulation was responsible for the other half of the momentum exchange. In a undeveloped situation, a third mechanism can be distinguished: momentum exchange by depth-averaged transverse mass transport. This momentum flux can be quantified by considering two control volumes, one covering the left (smooth) side and one at the right side of the flume; see figure 48. A momentum balance for both of these control volumes can be made. The momentum that is advected (per unit of time) in longitudinal direction by depth-averaged mass transport can now be quantified by the transported mass times its velocity. For an uniform flow, this can be written as:

$$M_{damt} = m \cdot \vec{v} = \rho \cdot A \cdot U \cdot U = \rho \cdot A \cdot U^2 \qquad \text{(equation 22)}$$

in which

M_{damt} is the momentum flux in x-direction caused by **d**epth **a**veraged **m**ass **t**ransport
m is the mass of the depth-averaged transport
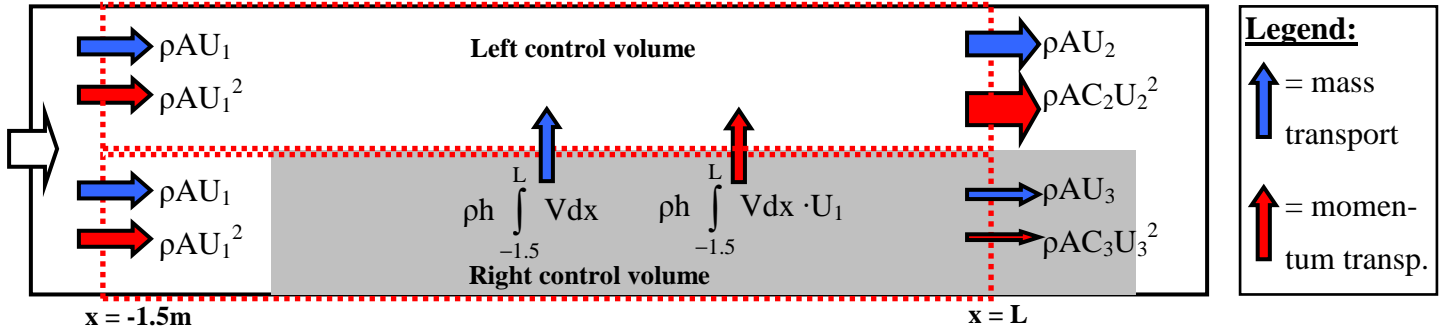$\vec{v}$ is the velocity vector

Figure 48:Definition of two control volumes (dashed lined) in top view. The corresponding mass and momentum fluxes are assigned. The parameters C_2 and C_3 account for the non-uniform velocity in the mixing layer. See appendix D for more details.

Since the velocity is squared in equation 22, it is obvious that M_{damt} changes when a uniform flow is divided into two sections with a velocity difference. The fluxes of M_{damt} in figure 48 could be derived from measurements, but since the number of measurement points in a cross sectional plane is limited, the outgoing velocities (U_2 and U_3) are not known accurate enough for calculating a reliable value for the change in momentum flux.

A theoretical analysis is more successful, based on a mass balance and the measured transverse velocities. Since the incoming and outgoing mass must give a balance in the control volume, the outgoing velocities U_2 and U_3 can be derived from U_1 and V. Furthermore, the profile of the transverse velocity V can be scaled on U_1: $V(x) = U_1 \cdot \widetilde{V}(x)$. Measurements of this normalised velocity were already shown in figure 38. Hence, the net momentum deficit at the smooth side can be derived. This elaboration is done in appendix D and shows that the imbalance of momentum due to the depth-averaged transverse mass transport equals:

$$\Delta M_{left} = \rho \cdot h \cdot U_1^2 \cdot \left(C_2 \cdot K^2 - K \right) \qquad \text{(equation 23)}$$

with

$$K = 1 + \int_{-1.5}^{L} \widetilde{V} dx \qquad \text{(equation 24)}$$

The parameter C_2 accounts for the non-uniformity of the velocity profile in the mixing layer and has a value of approximately 1.01. Note that this approach assumes that the advected momentum is not influenced by changes in side wall friction or changes in the vertical velocity profile.

A similar derivation can be made for the control volume at the right side of the flume, with the only difference that a minus-sign replaces the plus-sign in equation 24. Hence, the gradient in total advected momentum, due to depth averaged transverse mass transport, can be approximated by (see appendix D for the derivation):

$$T_{damt} = 2\rho \cdot h \cdot \overline{U_1}^2 \cdot \widetilde{V} \cdot \left(C_3 - C_2 - \left(C_2 + C_3 \right) \cdot \int_{-1.5}^{L} \widetilde{V} dx \right) \qquad \text{(equation 25)}$$

Since $T_{damt} < 0$, a momentum deficit occurs at the transition from a uniform flow to a flow over a parallel rough bottom. As a result, the pressure gradient is increased to realise the required balance of momentum. The transition to a uniform flow again would cause an equal momentum excess, which reduces the pressure gradient.

Figure 49 shows the gradients in advected momentum for the flume as a whole (T_{damt}). See appendix D for the individual control volumes ($T_{damt, left}$ and $T_{damt, right}$).
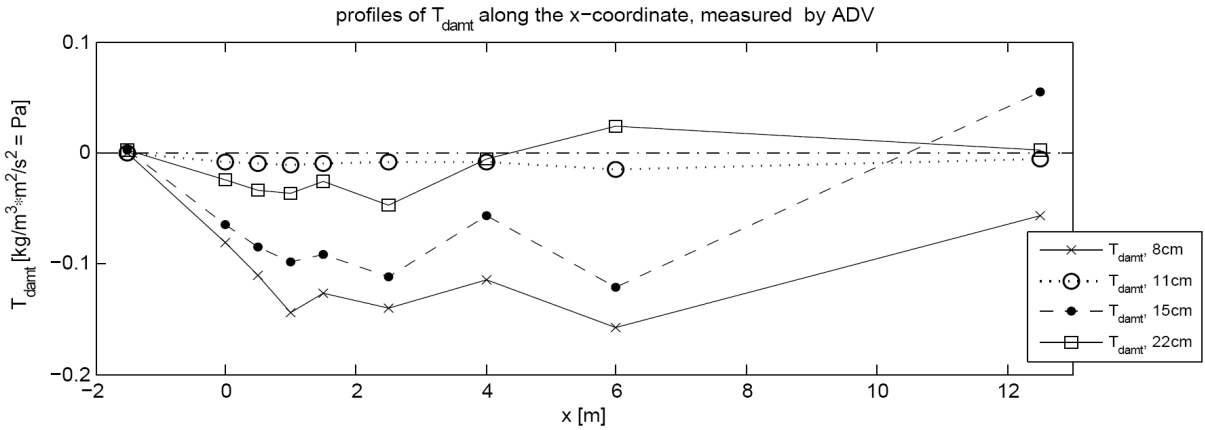

Figure 49: T_{damt} versus the longitudinal distance. T_{damt} represents the gradient in advected momentum (sum of both sides, i.e. for the flume as a whole). For these graphs, a depth-averaged approach is used. Differences in side wall friction and vertical profile shapes are neglected.

The other mechanisms of momentum exchange (T_{adv} and T_{mix}) can be calculated in the same way as for the developed situation (equations 16 and 17). One might expect the turbulent mixing to be dominant over secondary circulation in an undeveloped situation since the secondary circulation needs about 80 times the water depth to develop. To test this surmise, the development of the turbulent mixing layer vortices is shown first.

Figure 50 shows the shear stress at mid-depth for two cases, measured by using the ADV. It appears that this shear stress requires a longitudinal distance of about 30 water depths for an effect at mid-depth. This length scale is larger at the surface, motivated by an absence of mixing layer vortices in PTV measurements (not shown) within the first 2 meters, even for the shallow case of 3.5cm.
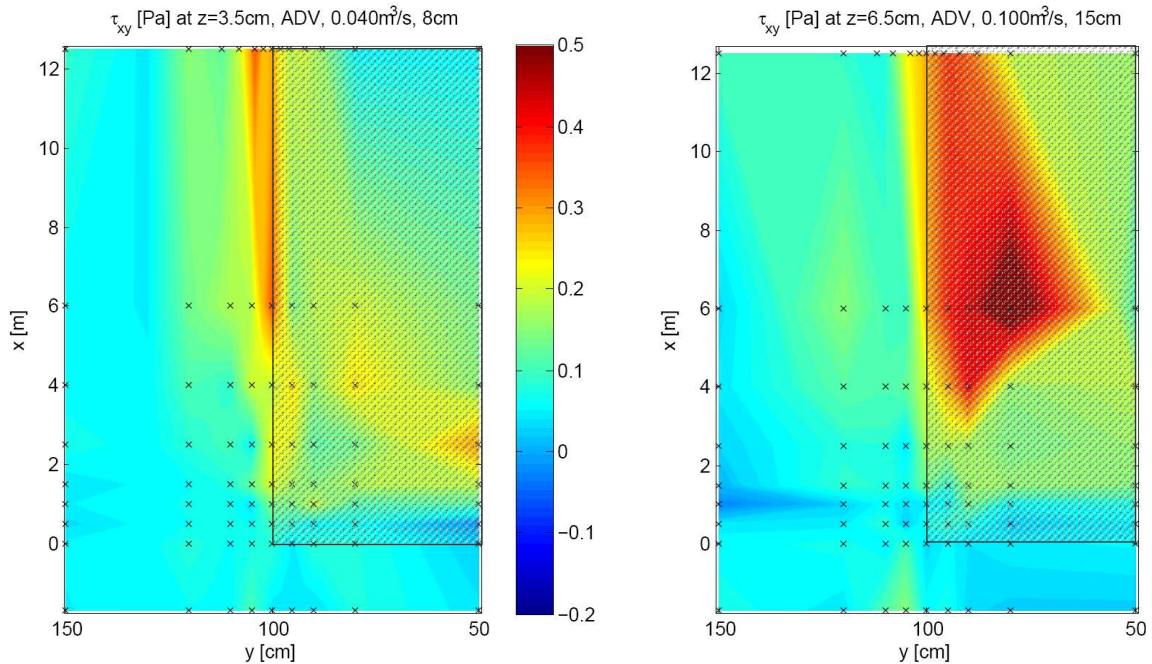

Figure 50: Shear stress in horizontal plane (i.e. $\tau_{xy} = -\rho \cdot \overline{u'v'}$) around mid-depth for two cases. The crosses indicate locations of ADV-measurements. Linear interpolation used.

According to figure 50, the highest shear stresses can be found initially above the rough side of the flume. Further downstream, this area is confined to the (rough side of) the mixing layer. One might postulate that the 'overshoot' in shear stress in case of 15cm depth at x=6m is due to insufficient momentum exchange by the not yet developed secondary circulation at this point (causing a larger $\partial u/\partial y$ and hence higher $\overline{u'v'}$). However, the measured transverse gradients of longitudinal velocity ($\partial u/\partial y$) are not notably larger at this location than at x=12.5m (see figure 44), so this maximum in shear stress is probably just a local effect.

The profile of momentum exchange at the parallel smooth-rough boundary (y=100cm) is shown in figure 51 for the deepest cases. The shallower cases show more irregular results. Figure 51 suggests that the transverse momentum exchange by secondary circulation is already larger than the momentum exchange by turbulent mixing from the start on. However, this does not match with the physical interpretation. Before x=4m hardly any secondary circulation was observed and the transverse volume transport dominates the transverse velocity profile. Figure 47 already showed that the transverse volume transport is largest close to the bottom, due to the simple fact that the longitudinal velocities are lower and hence the transverse pressure gradient has more time to act on the water parcels close to the bottom. For the calculation of the momentum exchange due to secondary circulation, the depth averaged transverse transport is subtracted (see equation 16). This contributes erroneously to the momentum transport of secondary circulation. Therefore, T_{adv} is overestimated at x<4m. Nevertheless figure 51 shows that the momentum exchange by advection from the start of the secondary circulation (around x=4m) is of the same order of magnitude or slightly larger than the exchange by turbulent mixing.
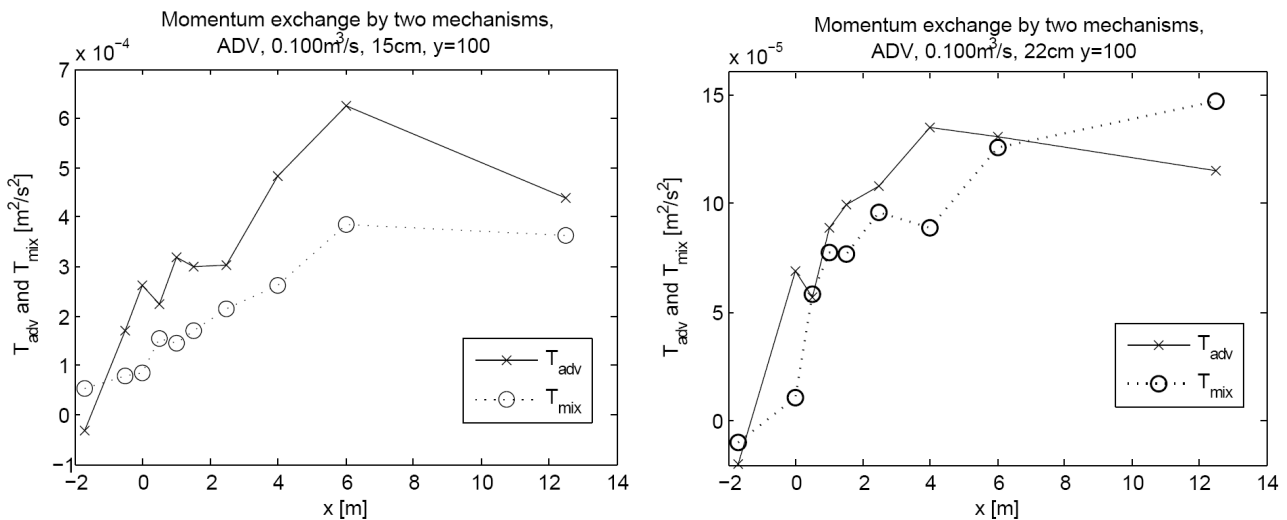

Figure 51: Transverse momentum exchange by advection and turbulent mixing, as function of longitudinal distance, measured by using the ADV. Values for T_{adv} at low x-values are overestimated due to transverse volume transport near the bottom. as explained in the text.

The gradient in advected momentum (figure 49), as well as the momentum exchange by turbulent mixing and advection due to secondary circulation (figure 51), contribute to the shear stress exerting on the water and must be balanced by an increase in pressure gradient. The shear stress corresponding to these three mechanisms is in the order of magnitude of

10^{-1} Pa. Hence, the effect on the water level slope is in the order of 10^{-4} (divided by $\rho \cdot g \cdot h$). Therefore these contributions are all significant since the measured water level slopes are in the order of 10^{-4} - 10^{-3}.

Water level profiles

The water level profiles are measured again by an electronic and manual gauge. The results of both instruments can be found in figure 52. The data from the electronic gauge show a local elevation at x=0m since the electronic gauge was installed at y=30 (i.e. above the rough side). Above the smooth side, where the manual gauge was installed, the water level is always lower at x=0m. This explains why the transverse volume transport is already at maximum around x=0m. The local elevation in the water level extends up to ca. 1 meter upstream. The water level becomes fairly linear again after 2.5 meter from the start of the parallel bed roughness.

Since the water level profile is locally affected by the change to a parallel rough bottom, the result of the undeveloped flow on the effective friction can not be deduced from the water level slopes. The bed shear stresses showed that the friction outside the mixing layer is higher for an undeveloped flow than for the developed flow. This is obvious since the velocity is initially larger. As a consequence the effective friction of an undeveloped flow over a parallel rough bottom is somewhat higher than in a developed flow.
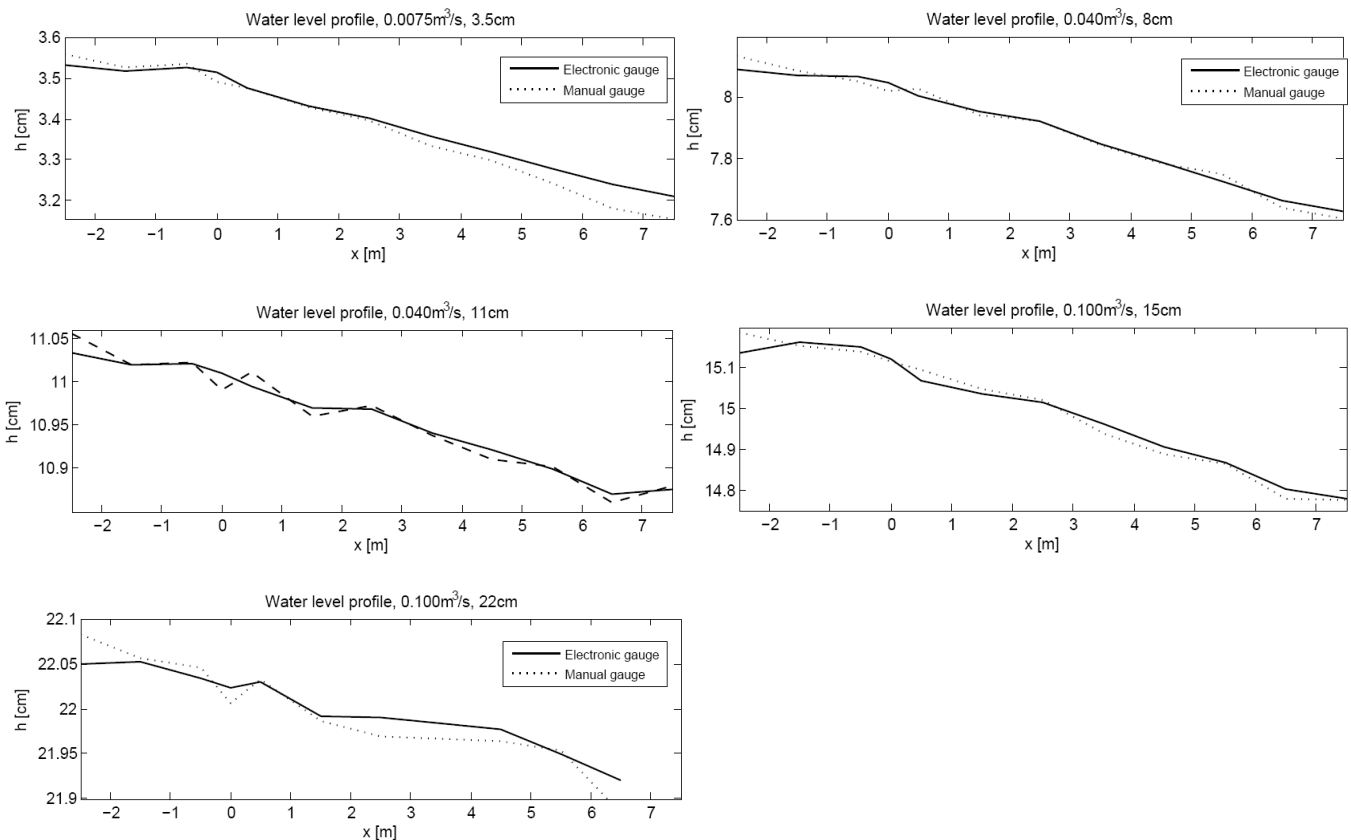

Figure 52: Water level profiles for all cases, measured by using an electronic gauge (mounted at the rough side) and a manual gauge (mounted at the smooth side). The measurements are corrected for the carriage reference by using a still water measurement

5)   Results for checkerboard configuration

The checkerboard configuration was measured intensively; measurements in four cross sectional planes were required to study the flow in three dimensions. Next to that these experimental measurements, LES results are available.

The results from the checkerboard configuration are presented in the following five properties:

- Consecutive transverse profiles of longitudinal velocity
- Transverse volume transport
- Transverse momentum exchange in the mixing layer
- Consecutive profiles of bed shear stress
- Effective friction

Each of these aspects will be treated in a paragraph below.

Longitudinal velocity

Whereas the parallel roughness evolves in a parallel flow situation with an intermediate mixing layer, the longitudinal velocity profiles are very different over a roughness pattern in checkerboard configuration. Figure 53 shows a sequence of longitudinal velocity in transverse profiles at two different depths, from ADV-measurements. In contrast to the parallel flow situation, the maximum longitudinal velocity can be found very close to the parallel smooth-rough interface. At lower depths, the profile tends to develop somewhat more towards the profiles known from the parallel situation but the profiles at middle depth are hardly changed over a 4-meter long checkerboard section. This is remarkable since figure 44 showed a more developed velocity profile at mid-depth in this case. Apparently the length scale of adaptation to the new roughness situation requires more than 50 water depths (as was found in the parallel flow situation) in case the upstream condition is non-uniform.
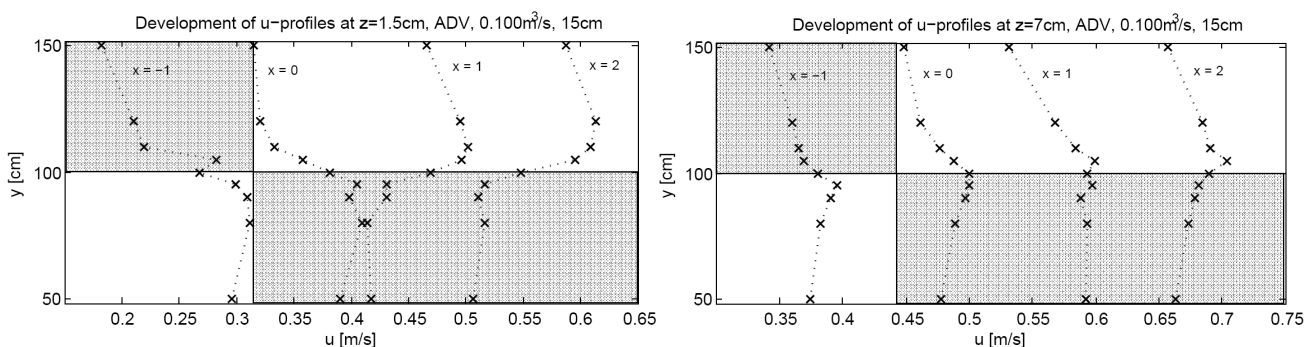

Figure 53: Consecutive transverse profiles of longitudinal velocity, close to the bottom (left panel) and around middle depth (right panel). Both are measured by using an ADV in the 15cm-case. Profiles are shifted 0.1 m/s to each other.

For a more general overview, figure 54 shows sequence of depth averaged velocity profiles for ADV-measurements. This sequence shows that the maximum (depth averaged) velocity is measured always at 5 or 10 cm from the interface. At the start of a new section

(x=0m), the maximum velocity is still at the side of the upstream smooth section. After 1 meter, the maximum has switched side. Again 1 meter downstream (x=2m), the maximum in depth averaged velocity is shifted little more towards the new smooth side. Furthermore, the difference in velocity between both sides is more amplified with respect to one meter upstream. One meter before the start of a new section (x=-1m), the picture is similar to that at x=2, except that the velocities are overall somewhat lower. The total discharge should be equal at all sections, so this velocity offset is probably due to a level offset in the ADV carriage. The carriage level could be a few mm lower at this section, such that the ADV measurements are taken closer to the bottom, yielding a systematically lower velocity.
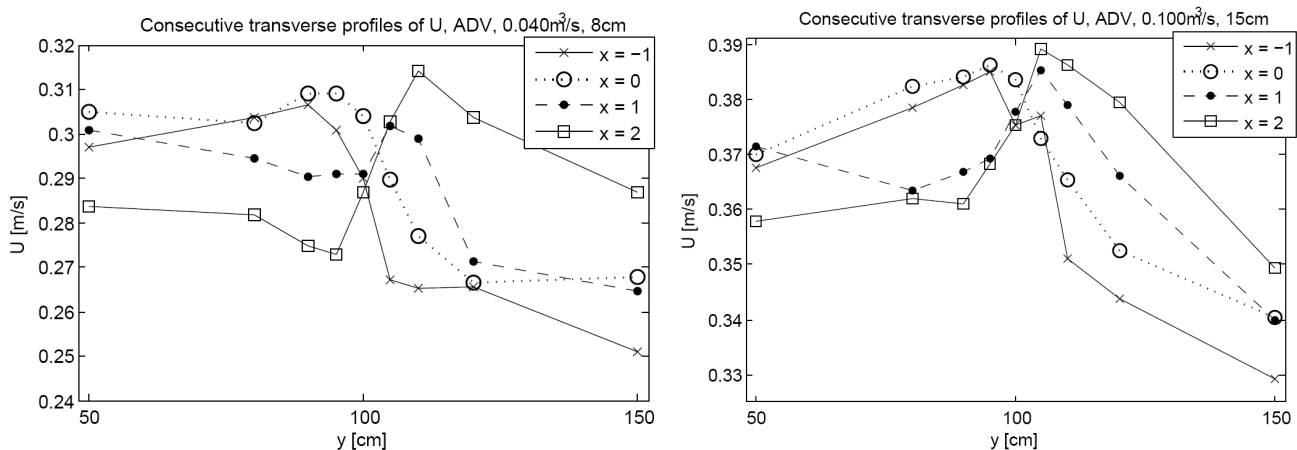

Figure 54: Consecutive transverse profiles of depth averaged longitudinal velocities, based on ADV-measurements for two cases. Data was extrapolated to the surface before depth averaging.

The cumulative effect of a full checkerboard repetition (so 8 meter length) on the velocity can be shown by averaging the velocity data in longitudinal direction. Figure 55 shows those sectional averaged velocities for ADV data, as function of the width coordinate. This illustrates the net result of bed roughness in a checkerboard pattern: the maximum velocity is located above the parallel smooth-rough interface. In the largest depth case (22cm), the sectional averaged velocity above the interface is almost 6% higher than the average velocity; this maximum becomes less distinct as the depth decreases. This is obvious since the maximum longitudinal velocity moves further from the parallel interface at shallow depths (see for example figure 53).

The very shallow case of 3.5cm seems to be more developed (at the surface) towards a parallel flow. Figure 56 shows the longitudinal velocity at the surface in two cases, from PTV measurements. The 8cm-case shows the maximum velocity before the switch at y=90cm, while this is at y=75cm for the 3.5cm case. Reminding the surface velocities in the developed parallel flow (figure 19), the 3.5cm case is already better developed than the 22cm case in a parallel flow after 12.5m, but is still not completely developed (the velocity ratio between the smooth and rough side is significant smaller than that in figure 19). From this comparison, one could roughly state that for the roughness under consideration the development of longitudinal velocities (at middle depth) to a new parallel roughness in a checkerboard configuration takes about 100 water depths.

54

At the roughness reversion, the velocity at the surface at the right side (where the bed is changing from smooth to rough) becomes even higher. This can be understood from the notion that the water is decelerated close to the bottom and needs to be accelerated (due to continuity) at the surface.

The transverse velocity at the surface around x=0m is higher at the 3.5cm-case than for the 8cm-case while the longitudinal velocity are larger in the 8cm-case. This is due to the higher relative roughness in the shallowest case. Consequently, water particles are faster transversely advected and hence the maximum longitudinal velocities (or the isotachs) at the surface are much more inclined at the shallow 3.5cm-case than at the 8cm case.
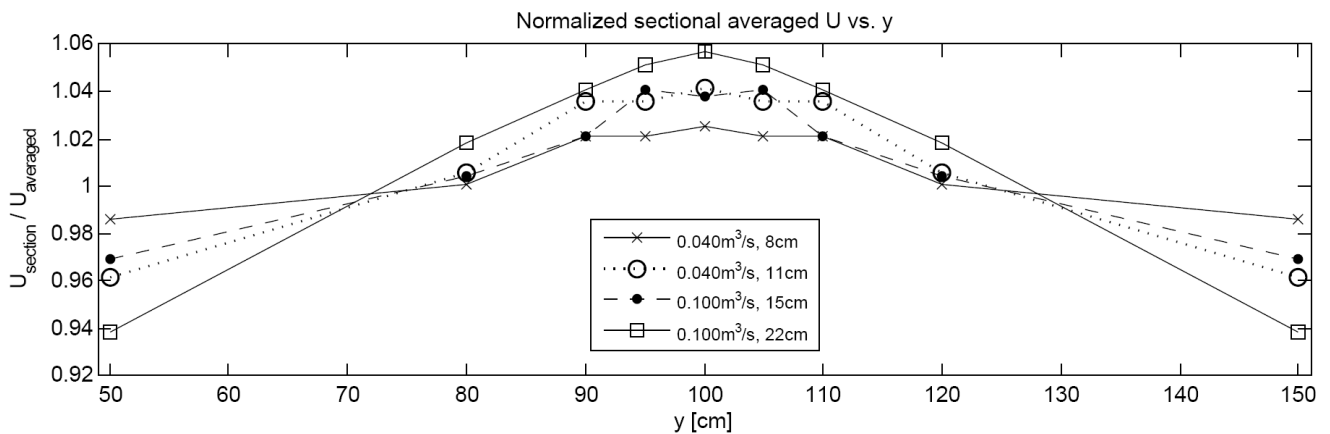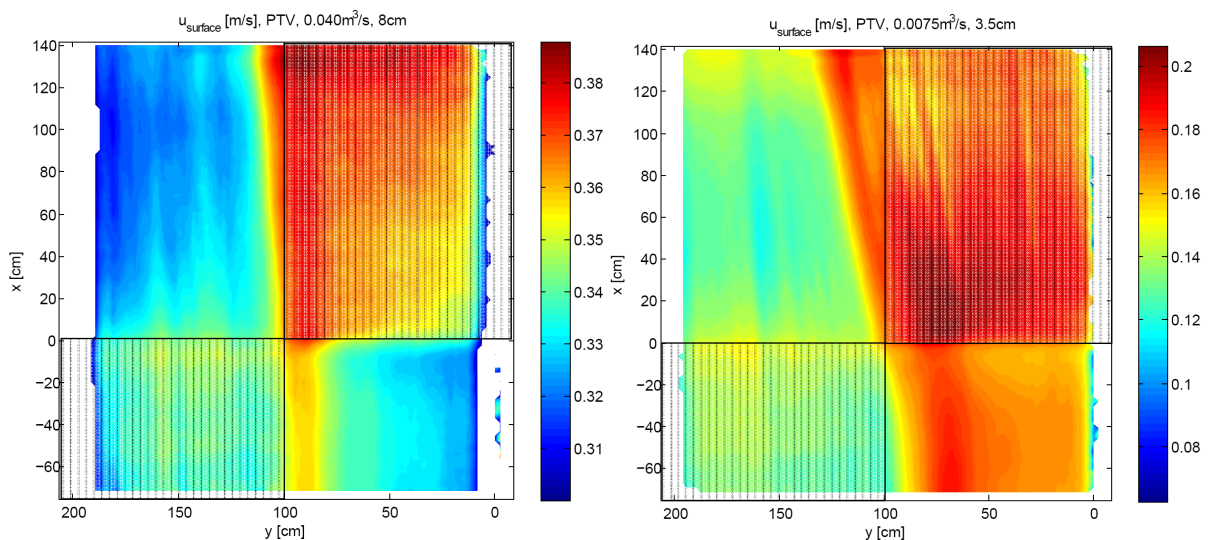

Figure 55: Transverse profiles of longitudinal velocity, averaged in depth and in longitudinal direction (=$U_{section}$), normalized to average (in all directions) velocities (=$U_{averaged}$).
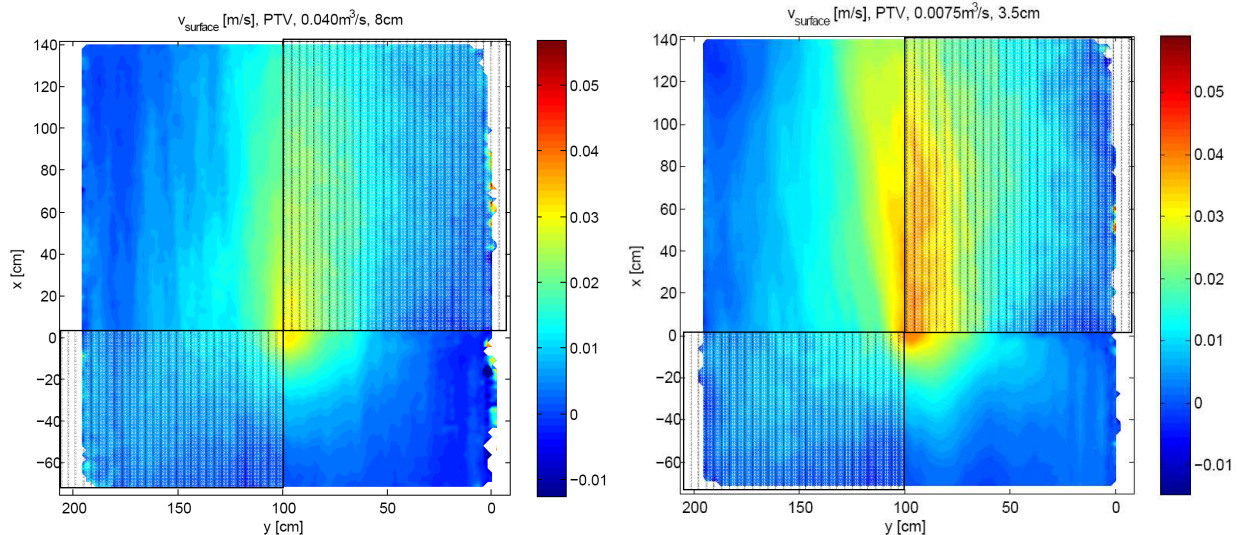

55

Figure 56: Velocity measurements at the surface deduced from PTV-technique, for longitudinal velocity (upper panels) and transverse velocity (lower panels), for the 8cm case (left panels) and 3.5cm case (right panels).The shaded areas indicate the rough beds.

Transverse velocity

The ADV-and LES-measurements show that the transverse velocity is at maximum above the smooth-rough reversion (x=0m, see figure 57) in accordance with the PTV-measurements in figure 56. The magnitude of the maximum transverse velocity is larger than those in the undeveloped situation (figure 47). The shift of the longitudinal velocity maximum gives reason for a higher (maximum) transverse velocity. However, the transverse volume transport is mainly limited to the first meter after a roughness reversion, so the total transverse volume transport is not significant larger in this configuration when compared to the developing flow (figure 47). A non-uniform (reverse) upstream condition would give reason for more transverse volume transport. This is not the case, so this illustrates once again that the flow over the checkerboard configuration is slower developing (within 4 meters) than in the start of a parallel flow from a uniform situation.
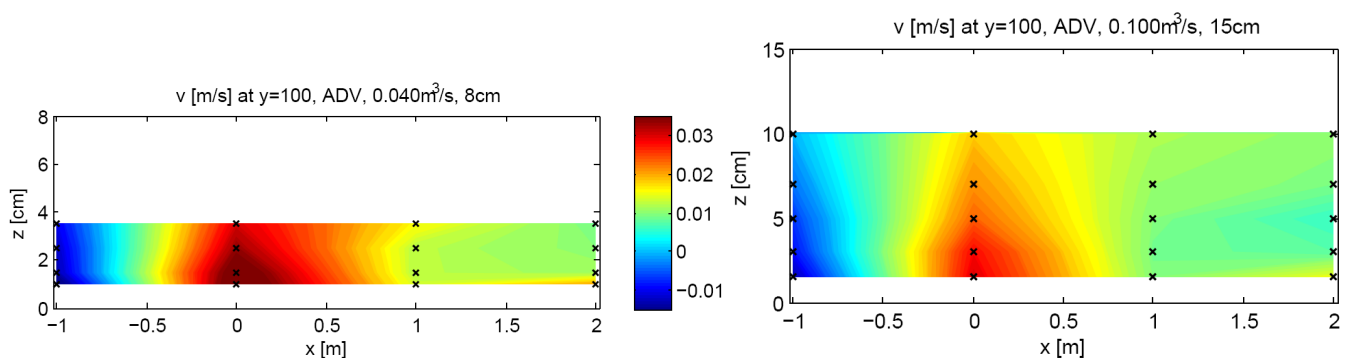
Figure 57: Transverse velocities at parallel interface (y=100cm), from ADV-measurements in two cases. The measurement positions are indicated by crosses.

Figure 58 shows the velocities in 4 subsequent cross sections, measured by using the ADV. The cross sectional velocities at x=-1m show a possible start of a secondary circulation, however no upward flow is measured. Upflow might occur in the region of 50<y<80, in that case a weak secondary circulation can be recognized at x=-1m. The circulation is

anyway much weaker than in the developed situation and even less clear than in the undeveloped flow after 4 meter (figure 46).

Figure 58 furthermore shows that, especially around x=0m, an upward flow is occurring above the serial smooth-rough change, whereas downward flow is present at the other side. This is in agreement with the acceleration at the surface velocity as was observed in figure 56.
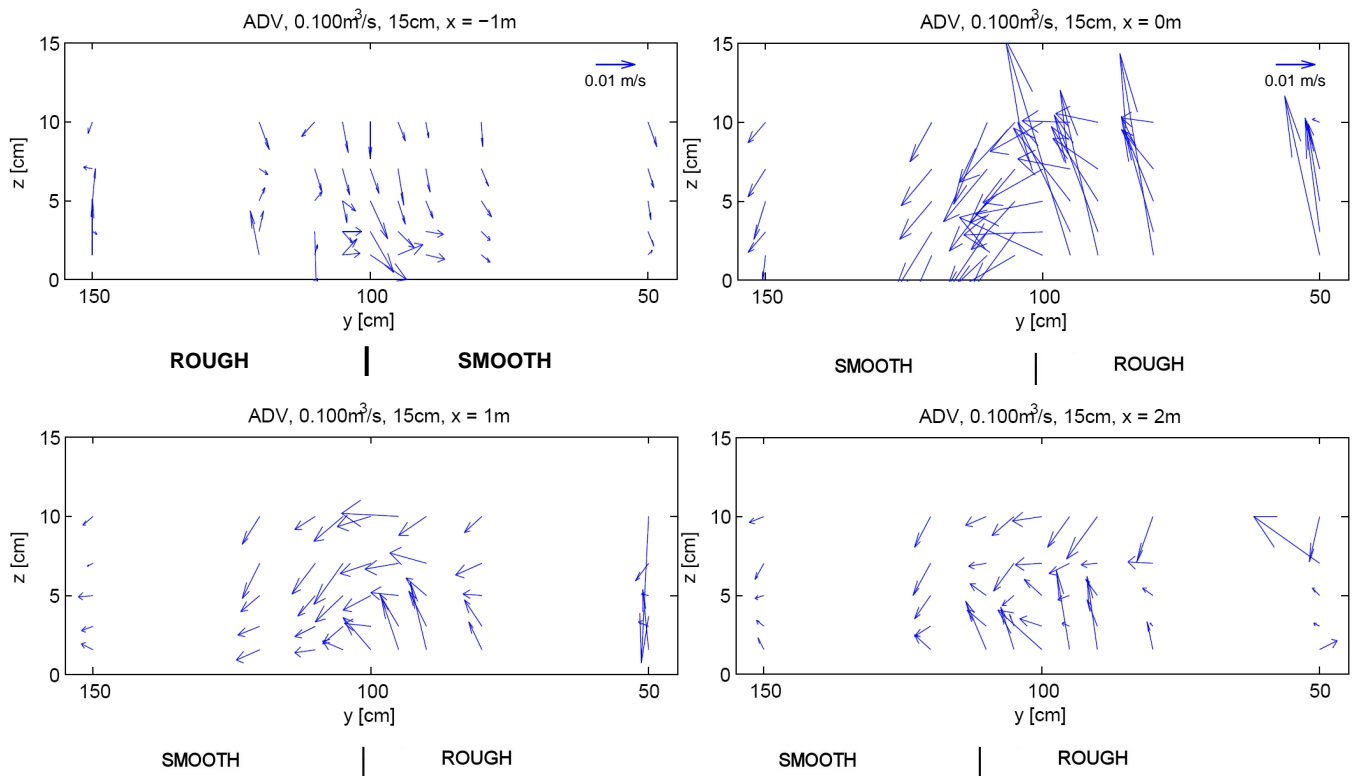

Figure 58: Velocities in cross plane (yz), at four cross sections. Data gathered by using an ADV, here for the 15cm-case. All vectors are equally scaled.

Momentum exchange

Just as in the undeveloped parallel flow, momentum exchange can be achieved by secondary circulation advection, turbulent mixing or depth averaged transverse mass transport. The last mechanism is not further elaborated due to its complex nature (due to its constantly chaning velocity profiles). Fortunately, the effect is assumed smaller than in the developing flow described in chapter 4 since the velocity profiles are less developed in a checkerboard configuration. Nevertheless, a further study on the momentum changes induced by depth averaged transverse flow is recommended for a full overview of the momentum exchanges in flow over a heterogeneous rough bottom.

The distribution of depth averaged turbulent mixing, from ADV- and LES-results, is shown in figure 59. This involves a very interesting phenomenon; the anti-clockwise eddies (in a top view) at x=-1m produce a positive $\overline{u'v'}$. At the roughness inversion at x=0m, these eddies are advected towards the left side, due to the volume transport to the smooth (left) side. Because the velocity gradient at the parallel interface changes sign after x=0m, eddies with an opposite direction ($\overline{u'v'}$<0) are produced around the interface. This

is exactly seen in figure 59. As a consequence the eddies of the last section are dominantly advected towards the downstream smooth side. If the checkerboard sections are rather short, these eddies are advected again towards the interface and can stimulate the momentum exchange in an early stage of a new roughness section.
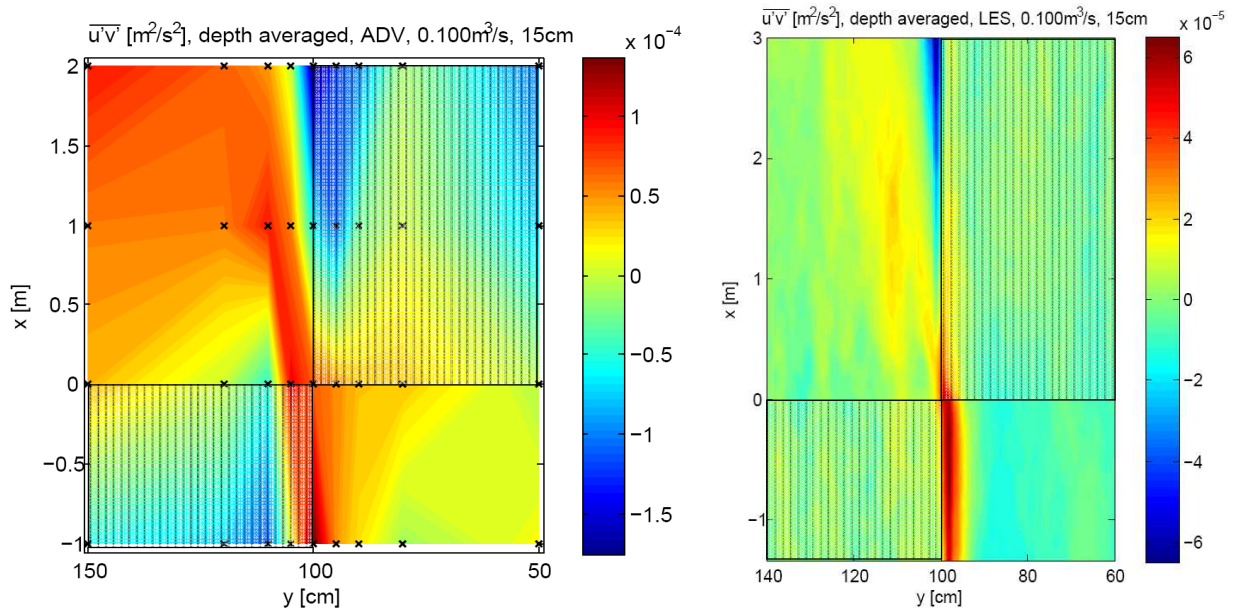

Figure 59: Covariance $\overline{u'\cdot v'}$, depth averaged, from ADV results (left panel) and LES (right panel). The bed roughness for the LES was set in checkerboard sections of 5 meter long; for the experiment (ADV) 4 meter long. The shaded areas indicate rough bed areas.

However, the advection of eddies is not very steady. An analysis of the vorticity in time based on LES-results (not shown) makes clear that eddies are irregularly shedded to the smooth side from x=0m. The distribution of $\overline{u'v'}$ in vertical cross sections agrees with this analysis (see figure 60); the areas of high covariance can not be linked directly in the sequence from x=0 to x=1 to x=2m. Figure 60 furthermore suggests that the advected eddies above the smooth side are slowly shifting towards the surface in their downstream follow-up.

The momentum exchange by advection is extremely irregular (since the – depth dependent – transverse volume transport is overwhelming the possible secondary circulation). Moreover, the secondary circulation was shown to be very weak or absent, so momentum exchange by this mechanism can be neglected. The momentum exchange by turbulent mixing (equation 17) as function of longitudinal distance is given by figure 61. The momentum transfer over the parallel interface by turbulent mixing is at maximum at x=0m. It takes about 1 meter after the roughness reversion until the shear stress has switched its sign. Although the magnitude of the momentum transfer between x=0 and x=1m is quite small, this transfer slightly supports the inversion of the velocity gradient at the interface.
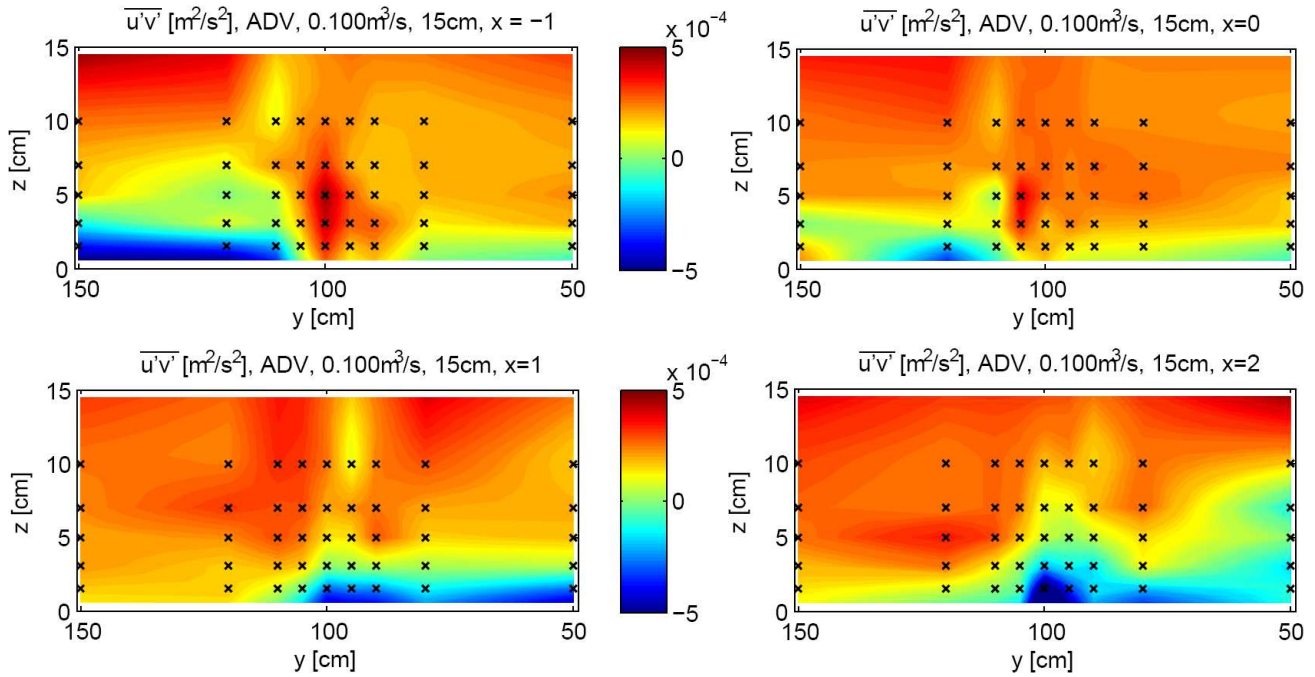
Figure 60: Covariance $\overline{u'\cdot v'}$, in depth and width for four cross sections. Locations of ADV-measurements are indicated by crosses. All plots have equal scales.
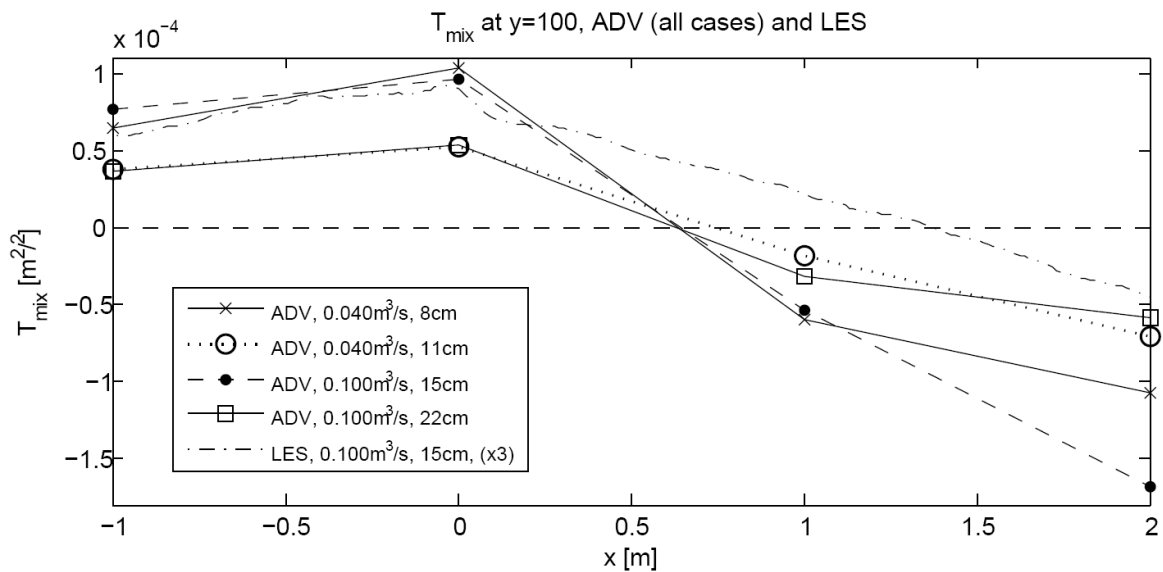
Figure 61: Depth averaged values for $\overline{u'\cdot v'}$ (i.e. T_{mix}), at the parallel interface (y=100cm), from ADV- and LES-results. The LES results are multiplied by 3 for a better scaling.

Bed shear stress

Figure 62 shows the bed shear stress in 4 consecutive cross sections, measured by using the ADV for two cases. The magnitude of the stress is somewhat larger above the rough side compared to the (un)developed flow. The bed shear stress above the smooth side is similar to the former configurations. Therefore the difference in stress between the smooth and rough side is larger; typical for an undeveloped (parallel) flow. It is also obvious that

the rough side has an even higher bed shear stress than in the undeveloped flow in chapter 4 since the upstream conditions are not uniform but inverting. A consequence of this bed shear stress pattern is that the checkerboard configuration induces extra bed friction and (alternately switching) transverse water level slopes.
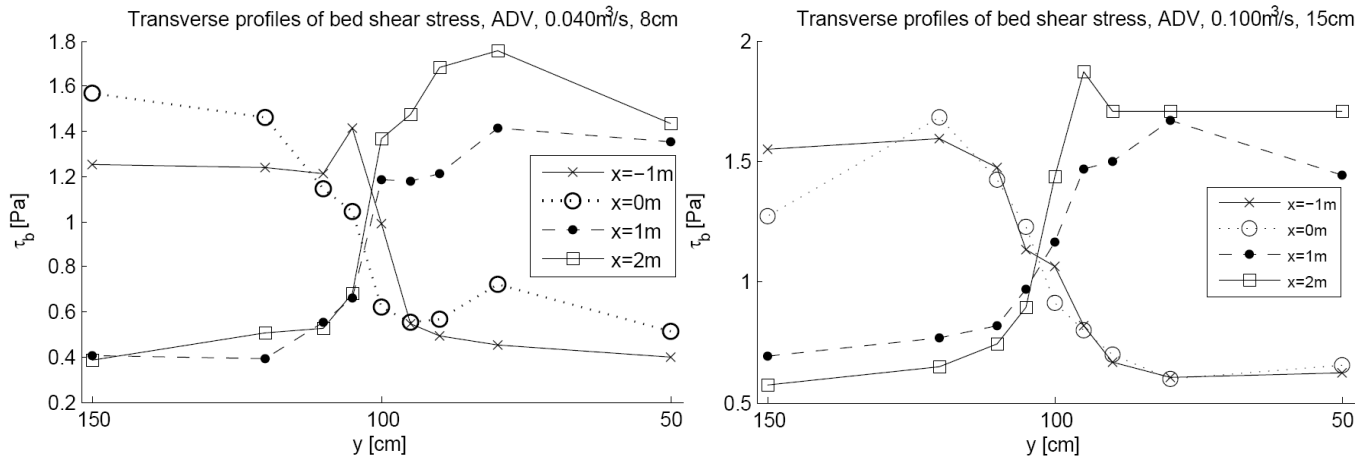
Figure 62: Bed shear stress, derived by fitting vertical profiles of $\overline{u'\cdot w'}$, obtained by using the ADV, for two depth cases.

Figure 63 shows that the bed shear stress has a subtle maximum just after a smooth-rough reversion when derived by fitting the logarithmic law of the wall. This is not clear by figure 62, probably because the profiles of $\overline{u'w'}$ are more sensitive to the non-uniform effects (non-linear vertical profiles) than the logarithmic law of the wall. Nevertheless, it can be said that a high bed shear stress is persistent for the full rough section. This is typical for a moderate development which was also seen in the time-averaged velocities. As a consequence, the (width averaged) friction coefficient is almost constant in longitudinal direction; see figure 64.

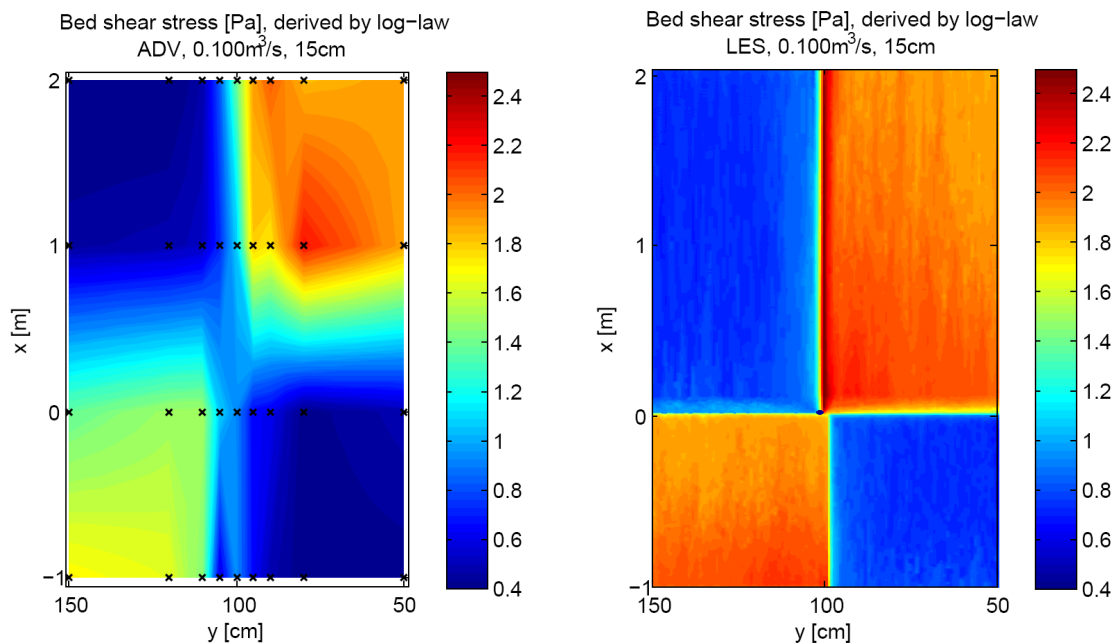*Figure 63: Bed shear stress in two dimensions, derived by fitting vertical profiles of $\overline{u'\cdot w'}$ from the LES.*
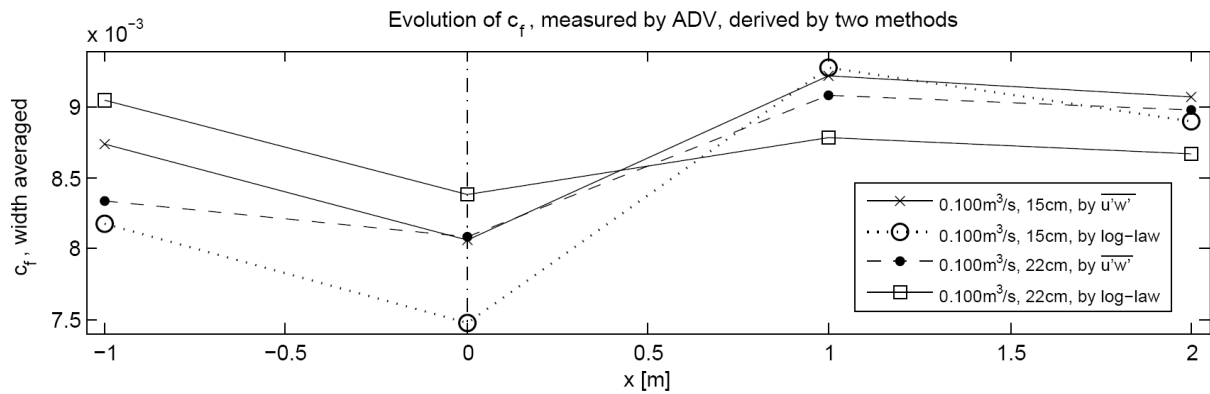
Figure 64: Friction coefficient c_f, as function of x along a checkerboard section. Only results for the 0.100m³/s cases are shown, derived from ADV-data. The values for c_f are calculated in two ways; by fitting the velocity profile to the logarithmic law and by fitting the $\overline{u' \cdot w'}$ profiles.

Effective friction

The water level profiles are shown in figure 65. Clearly visible are the shoulders in the water level at a roughness reversion, especially the one from smooth to rough (x=0m). Except for this backwater effect, the water levels are rather linear.
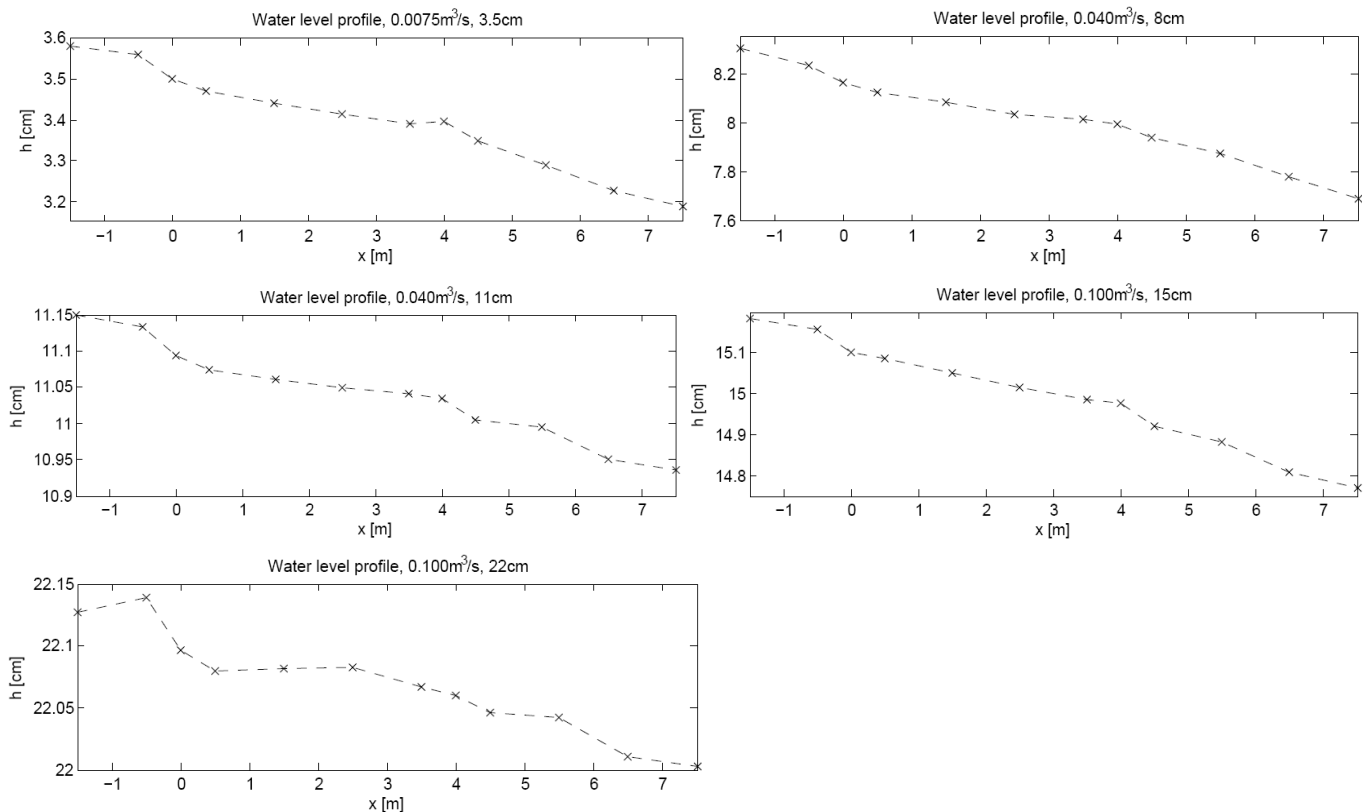
Figure 65: Water level profiles for all cases, measured by using the electronic gauge. The measurements are corrected for the carriage reference by using a still water measurement.

The water level slopes are calculated based on the water levels at x=-1.5 and x=6.5m, since these locations are both at the same position in a roughness section (both above a smooth bed, 2.5m after a reversion). Hence, the effective friction can be calculated again

from the water level slopes and compared to the preliminary (homogeneous case) theoretical equivalents. Table 5 shows that the effective friction factor is increased by about 40% compared to a theoretical parallel approach without interaction.

Table 5: Water level slopes and corresponding friction factors of checkerboard configuration.

Q (m³/s)	h (cm, at x=8m)	Theoretical values, based on individual sections				$f_{eff\ measured}$	$f_{eff,\ measured}$ / $f_{eff,\ theory}$
		$k_{s,\ ruw}$ (m)	f_{ruw}	f_{smooth}	$f_{eff,\ theory}$		
0.0075	3.5	0.018	0.139	0.042	0.070	0.103	1.47
0.040	8.0	0.015	0.078	0.027	0.043	0.060	1.42
0.040	11.0	0.014	0.066	0.027	0.040	0.058	1.46
0.100	15.0	0.011	0.055	0.022	0.033	0.043	1.33
0.100	22.0	0.008	0.042	0.022	0.029	0.040	1.36

The results from the LES show again smaller effective friction factors; the checkerboard configuration had 17% extra friction compared to the calculation of equation 8. For the same reasons as for the developed parallel situation, the actual results will be in between; the effective friction can best be estimated at about 30% extra with respect to the results of equation 8.

The higher friction compared to the developed parallel cases can be explained by the extra bed shear stress above the rough side (see figure 62). This serial roughness change causes significant extra bed friction. Although the transverse momentum exchange is small, the parallel roughness change has indirect also a large contribution to the effective friction factor. The parallel roughness change introduces a non-uniform upstream flow condition and a longer development length. So, the combination of these roughness changes is the most effective way to increase the effective bed friction.

Recommendations for 1D and 2D modelling

Again, a flow over a rough bed in checkerboard pattern might be approximated by a 1D or 2D model (in order to reduce calculation power and time). Some recommendations for such models can be given based on the experiments in this configuration. An exact checkerboard pattern in roughness will not occur often in practical situations. This checkerboard configuration is rather a typical example for roughness variations in serial and parallel direction. Different variants with combined serial and parallel roughness may give different quantitative results, but the principle is probably equal to this case.

A 1D model must account for the surplus in bed friction compared to the friction factor calculated by equation 8. The experiments on a checkerboard pattern with 4 meter sections showed that about 40% extra friction should be taken into account, in a range of $k_{s,\ rough}/h$ between 0.09 (22cm case) and 0.54 (3.5cm case). For the shallow flow (3.5cm case), the theoretical value appeared to be uncertain in the developed parallel flow (see table 4), so also for this configuration a larger uncertainty should be taken into account for this highest relative roughness.

A horizontal 2D (xy) model allows to impose the actual spatial roughness distribution. However, two effects are not taken into account for a depth averaged flow:

- the transverse interaction due to turbulent mixing layer vortices

- the extra roughness at a serial smooth-to-rough change due to a non-adapted velocity profile in vertical direction

The first effect was also involved in the developed parallel flow situation. An effective turbulent viscosity was rather effective there to mimic the measured velocity profiles. No secondary circulation occurs in this configuration, so the turbulent viscosity parameterizes only the turbulent mixing ($\overline{u'v'}$). Results in two dimensions based on ADV- and LES-data are shown in figure 66 (left and middle panel). Although the distributions of turbulent viscosity are peaky, the differences between the several depth cases are relatively small (not shown); all cases show a pattern with the highest values close to the parallel interface, and following the velocity maximum. Negative values can be found regularly in the middle above the rough side and is due to advection of eddies from the last section (while the velocity gradient already switched sign). The velocity and covariance magnitudes are small in this section, so this is only a minor effect. A physically based estimate, such as in equation 21, also shows the highest values for the turbulent viscosity around the parallel smooth-to-rough interface (figure 66, right panel). This motivates the hypothesis that the secondary circulation (in the developed parallel) was responsible for the different pattern in the effective turbulent viscosity. For this configuration, the pattern defined by equation 21 can be used for the effective turbulent viscosity in a 2D model, although the measured and simulated results differ considerably to the estimated values in some areas. The magnitude of the measured turbulent viscosity is still somewhat larger than compared to equation 21, especially around the parallel interface. This magnitude better matches the measured and simulated results (for this configuration) by modifying equation 21 to:

$$\nu_{turb} = \frac{\kappa}{2} \cdot \sqrt{c_f} \cdot U \cdot h + \beta^2 \cdot \delta^2 \cdot \left| \frac{\partial U}{\partial y} \right| \qquad \text{(equation 26)}$$
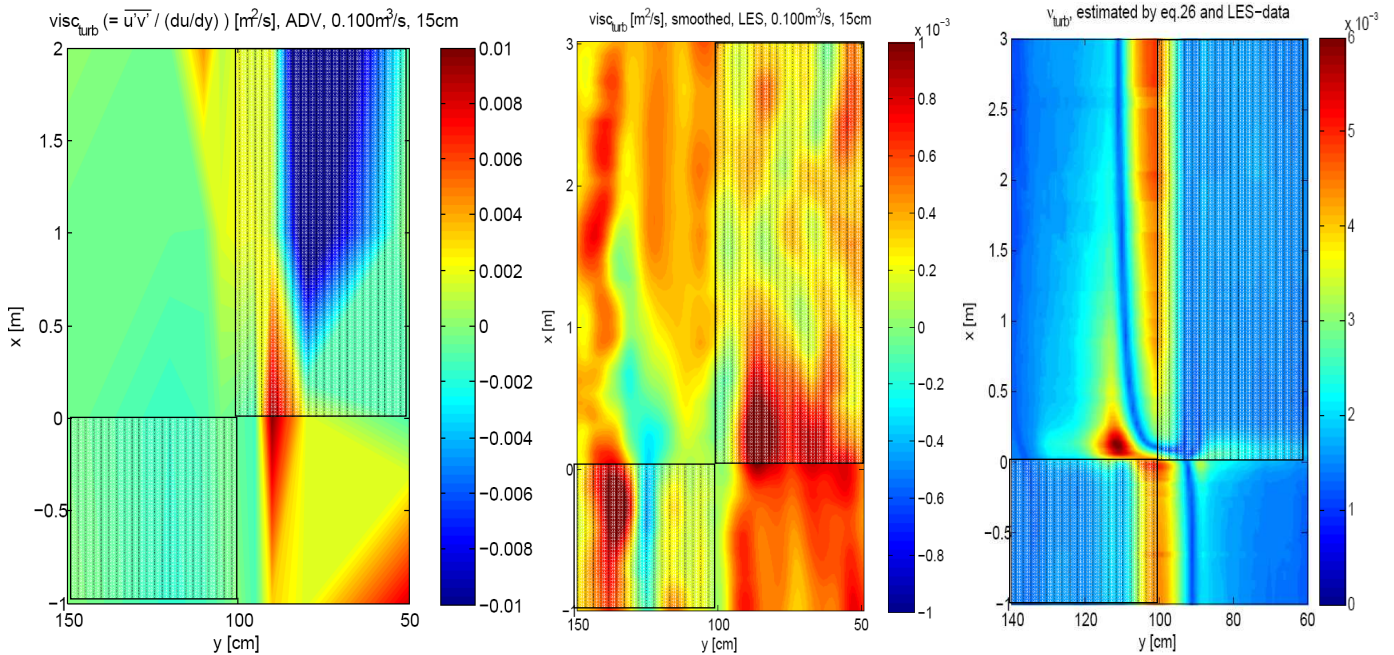
With β = 0.25 in stead of 0.1.

Figure 66: Distribution of turbulent viscosity for transverse direction. Left panel: based on ADV measurements. Middle panel: based on the LES results. Right panel: estimates from equation 26.

The second effect can be included in a model by an increase in the friction parameter. Since the flow develops very slowly in a checkerboard configuration, the friction parameter only slightly changes over a roughness section; see figure 67. The values for c_f are at maximum in the middle (in some cases at the beginning) of a rough section. Apparently the velocity adapts just as fast to the new bed roughness as the bed shear stress; possibly due to an upstream water level effect that influences the velocities already before the roughness reverses. A step function can be used to implement the bed roughness in a 2D model for a proper representation of a checkerboard pattern.
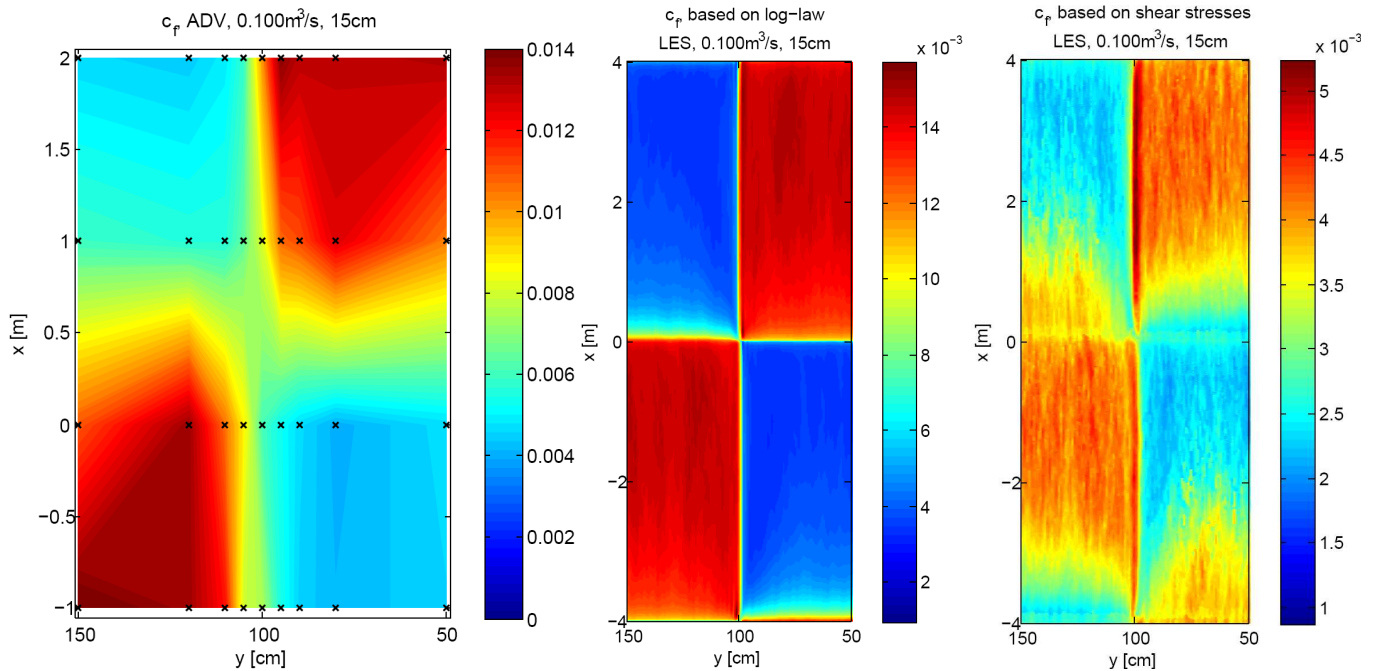

Figure 67: Distribution of friction coefficient over a checkerboard section. Left panel: based on shear stresses as measured by the ADV (crosses indicate measurement locations); right panel: based on the LES; shear stress and log-law.

Furthermore the total effective friction should be 40% higher than based on a parallel flow without any momentum exchange. Probably this is not achieved by the given distributions of c_f and υ_{turb} (just as in the parallel flow case). An additional shear stress is required in that case to achieve a 40% increase in effective friction. A check in a 2D model (such as WAQUA) is required to determine the value for the additional bed friction to reach 40% in comparison with the theoretical friction parameters.

Furthermore the development of the velocity profiles should be investigated in a 2D model. The development lengths as estimated in this research (50 water depths for a mixing layer with uniform upstream conditions, about 100 water depths with non-uniform upstream conditions) should be obeyed in a 2D model. Since a depth averaged model can not include the development of vertical profiles, the result can be unsatisfying by using the current spatial function of c_f. In that case, sectional averaged values can be used in a model with bed roughness in a checkerboard configuration; the resulting velocity profile should be equivalent to that in figure 55.

A final remark is that the spatial functions for c_f and the turbulent viscosity are rather uniform within a checkerboard section (figure 63, 64, 66 and 64). That suggests that this approach is also valid for shorter and longer longitudinal sections of parallel roughness.

6)   Conclusions

There is relatively little known about the practical effects of heterogeneous roughness. Many researches have been done to compound channel flow, some to transitions in serial roughness changes and some to secondary flow in parallel rough beds. This research adds to these previous ones values for the effective friction of flows over parallel rough beds, the corresponding length scales and explanation of the mixing layer processes. For that purpose a comprehensive set of measurements in a horizontal flume was done, with focus on the mixing layer, using an ADV, PTV and gauges. Furthermore a LES was used to simulate the flow under the same conditions.

The results from the developed parallel flow show an asymmetrical transverse profile of the longitudinal velocity; with a longer spanwise length to reach a constant velocity ($\partial u/\partial y \approx 0$) above the smooth side than above the rough side. The shown presence of a clear secondary circulation has a role in these. The centre of the secondary circulation was located above the smooth side, explained by analysing the turbulence kinetic energy balance.

The secondary circulation gives rise to momentum exchange in transverse direction, in addition to the turbulent mixing. The advective momentum exchange due to the secondary circulation appears to be in the same order of magnitude as (or little larger than) the direct turbulent momentum exchange. The results from the LES show that the relative contribution of advective momentum exchange becomes larger when the depth is larger (smaller relative roughness) or the velocity is lower.

Due to this mixing layer effects, the effective friction is increased by 15-20%. Therefore, in 1D or 2D models, an additional stress is required to account for this extra friction.

In the development of the flow over parallel roughness lanes, the transverse volume transport is initially most striking. This flow can be scaled on the width of the flume and is important in the first 4 meters (twice the width). The development length for the velocity profiles (vertical profiles above the rough lane, transverse profiles in the mixing layer) can be scaled mainly on the depth of the flow. The vertical profiles outside the mixing layer develop in about 25 times the water depth; the mixing layer at middle depth in about 50 water depths.

The transverse momentum transport due to a secondary circulation was according to the calculations also larger in the undeveloped flow than the transport by turbulent mixing. However, the momentum transport due to a secondary circulation is overestimated due to a contribution of transverse mass transport and can only be trusted after twice the width of the flume. Nevertheless, it shows that the advective momentum transport can be also an important mechanism in a developing mixing layer.

The depth averaged transverse mass transport plays another role in the momentum balance; this transverse mass transport causes acceleration and deceleration of the flow and hence a changing amount of advected momentum in longitudinal direction. Considering the flume over its total width, this effect demands extra momentum during the transition from a uniform to a parallel flow, which must be balanced by an increased water level slope. All three described mechanisms have a significant influence on the water level slope.

The water level slopes are locally affected by the start of a parallel rough bed. Furthermore, the effective friction will increase even more at this serial smooth-to-rough transition deduced from the bed shear stress profiles.

The flow over a bed roughness organised in an elongated checkerboard pattern (with 4 meter sections) has a remarkable different distribution. The maximum velocity remains close to the smooth-rough interface and develops only slowly towards a flow over parallel rough beds (about 100 water depths for velocities at middle depth), with as a consequence that the bed shear stress is even more pronounced at the rough side of the interface. No secondary flow is observed in this configuration. Turbulent mixing is neither very effective since the vortices are changing direction not before 1 meter after a roughness change. Although, the effective friction is seriously increased by this configuration; about 30% extra friction is observed in comparison with a developed parallel flow without transverse interaction. The combination of a serial and parallel roughness change, as is set in this checkerboard configuration, appears to give a large increase to the effective friction. This is again an important issue to implement in 1D and 2D models.

Further research is recommended in the line of modelling similar flows. The LES gave very good resemblance of the time averaged velocities, but failed to represent the shear stresses correctly. The bottom boundary conditions should be revised and more flow configurations can be tested. Besides that, from a practical point of view the implementation in 1D or 2D models can be described in more detail. By examining the possibilities of implementation in prevailing model packages, the effects of heterogeneous roughness can be optimal represented.

Literature

ANTONIA, R.A. AND R.E. LUXTON, 1971, *The response of a turbulent boundary layer to a step change in surface roughness – part 1: smooth to rough,* J. Fluid Mech., vol.48, 4, 721-761

ANTONIA, R.A. AND R.E. LUXTON, 1972*, The response of a turbulent boundary layer to a step change in surface roughness – part 2: rough to smooth,* J. Fluid Mech., vol.53, 4, 737-757

BOERSMA, B.J., 2007 (internet), *An introduction to LES/DNS simulation,* www.ahd.tudelft.nl/~bendiks/

BRAY, D.I., 1982, *Flow resistance in gravel-bed rivers,* Gravel-bed Rivers: fluvial processes, engineering and management, 109-133

CAMANEN, B., A. BAYRAM AND M. LARSON, 2006, *Equivalent roughness height for plane bed under steady flow,* J. of hydr. eng., 132, 11, 1146-1157

DOUGLAS, J.F., J.M. GASIOREK AND J.A. SWAFFIELD, 2001, *Fluid Mechanics,* 4th edition, Pearson, Essex, 911 p.

HINZE, J.O., 1967, *Secondary currents in wall turbulence,* The physics of fluids supplement - boundary layers and turbulence, vol.10, 9, S122-S125

JARQUÍN, M.F., 2007, *Experiments on the effects of heterogeneous roughness in open channel flows,* MSc thesis WSE-HERBD-07.16, UNESCO-IHE

KNIGHT, D.W. AND F.A. BROWN, 2001, *Resistance studies of overbank flow in rivers with sediment using the flood channel facility,* J. of hydraulic res., vol.39, 3, 283-301

MYERS, W.R.C., J.F. LYNESS AND J.CASSELS, 2001, *Influence of boundary roughness on velocity and discharge in compound river channels,* J. of hydraulic res., vol.39, 3, 311-319

NEZU, I. AND H. NAKAGAWA, 1991, *Response of velocity and shear stress to abrupt irregularity of bed roughness in streams,* 14th IAHR Congress, Madrid, A235-A242

NEZU, I. AND H. NAKAGAWA, 1993, *Turbulence in open-channel flows,* Balkema Rotterdam, 280 p.

NIEUWSTADT, F.T.M., 1998, *Turbulentie,* Epsilon, Utrecht, 211 p. (in Dutch)

NORTEK AS, 2004, *Vectrino velocimeter used guide October 2004 rev. C*, Nortek AS, Norway

POPE, S.B., 2000, *Turbulent flows,* Cambridge University Press, 771 p.

SIEBEN, J., 2006, *Ruwheidsformuleringen in waterbewegingsmodellen, verkenning,* Rijkswaterstaat – riza, werkdocument 2001.202x (in Dutch)

SMART, G.M., 1992, *Stage-discharge discontinuity in composite flood channels,* J. of hydraulic res., vol.30, 6, 817-833

SOFIALIDIS, D. AND P. PRINOS, 1999, *Numerical study of momentum exchange in compound open channel flow,* J. of hydr. eng., vol.125, 2, 152-165

STUDERUS, F.X., 1982, *Sekundärströmungen im offenen Gerinne über rauhen Längsstreifen,* Dissertation ETH Nr 7035, Eidgenössischen Technischen Hochschule, Zürich (in German)

TAYLOR, R.H., JR., 1961, *Exploratory studies of open-channel flow over boundaries of laterally varying roughness,* W.M. Keck Laboratory of Hydraulics and Water Resources, Pasadena, California, Report no. KH-R-4

TOMINAGA, A. AND I. NEZU, 1991A, *Turbulent structure in compound open-channel flows,* J. of hydr. eng., vol.117, 1, 21-41

TOMINAGA, A. AND I. NEZU, 1991B, *Turbulent structure of shear flow with spanwise roughness heterogeneity,* Environmental Hydraulics, Balkema Rotterdam, 415-420

TOWNSEND, A.A., 1966, *The flow in a turbulent boundary layer after a change in surface roughness,* J. of Fluid Mech., vol.26, 2, 255-266

UIJTTEWAAL, W.S.J, AND R. BOOIJ, 2000, *Effects of shallowness on the development of free-surface mixing layers,* physics of fluids, vol.12, 2, 392-402

VAN PROOIJEN, B. C., 2004, *Shallow mixing layers,* PhD thesis, TU Delft

VERMAAS, D.A., W.S.J. UIJTTEWAAL AND A.J.F. HOITINK, 2007, *Effect of heterogeneous bed roughness on the conveyance capacity of floodplains,* Proceedings NCR-days 2007

WANG, Z.Q. AND N.S. CHENG, 2006, *Time-mean structure of secondary flows in open channel with longitudinal bedforms,* Advances in water resources, vol.29, 1634-1649

Appendix A: List of used symbols

Greek symbols:

ε	Dissipation of turbulent kinetic energy trough the energy cascade
κ	Von Karman constant (=0.41)
θ	Angle of ADV beam
ρ	Water density
τ	Shear stress
τ_b	Bed shear stress (in longitudinal direction)
ν	Molecular kinematic viscosity
ν_{turb}	Turbulent viscosity

Latin symbols:

A	Cross sectional area
c_f	Friction coefficient (= f/8)
C_2, C_3	Coefficients correcting in momentum balance for non-uniformity
d_{50}	Median diameter of roughness elements
d_{90}	90% percentile diameter of roughness elements
f	Friction factor (Darcy)
f_{eff}	Effective friction factor
f_{rough}	Friction factor of rough bed
f_{smooth}	Friction factor of smooth bed
Fr	Froude number
g	Gravitational constant (=9.81 m/s^2)
h	Total water depth
k	Turbulent kinetic energy
k_s	Nikuradse roughness height
m	Mass of water volume
M_{damt}	Momentum flux in x direction, caused by depth averaged mass transport
R	Hydraulic radius
Re	Reynolds number
Q	Discharge
S	Water level slope
T_{adv}	Transverse momentum exchange by secondary circulation advection
T_{damt}	Momentum flux gradient due to depth averaged mass transport
T_{mix}	Transverse momentum exchange by turbulent mixing

u	Local velocity in longitudinal (x) direction
U	Depth averaged velocity in longitudinal (x) direction
$\mathbf{U_1, U_2, U_3}$	Depth averaged longitudinal velocities in a control volume
$\widetilde{\mathbf{U}}_2, \widetilde{\mathbf{U}}_3, \widetilde{\mathbf{V}}$	Normalized functions of U_1, U_2 and V
u*	Friction velocity
v	Local velocity in transverse (y) direction
V	Depth averaged transverse velocity
$\mathbf{v_x, v_y, v_z}$	Velocities in a Cartesian coordinate system relative to the ADV
$\mathbf{v_1, v_2, v_3, v_4}$	Velocities in the direction of respectively ADV beam 1, 2, 3 and 4
w	Local velocity in vertical (z) direction
x	Coordinate for longitudinal direction, increasing in downstream direction
y	Coordinate for transverse direction, increasing towards left side (with respect to x-direction)
z	Coordinate for longitudinal direction, increasing in upward direction

Appendix B: Quantitative differences in turbulence between ADV and LES results

The time-averaged velocities from the LES are in very good agreement with the ADV-measurements. The shear stresses and turbulence quantities however, appeared to be systematically lower. This appendix compares these values and its distribution.

Figure B.1 shows the shear stresses of ADV-measurements of the developed flow in case of 15cm depth. Figure B.2 shows the equivalents from the LES-results. The magnitude of the stresses in the LES-case is much smaller than in the ADV-measurements, respectively 4x, 3x and 10x smaller in the LES-results. However, the distributions of $\overline{u'v'}$ and $\overline{u'w'}$ are rather similar in the LES- and ADV-results.

Note that the lowest data grid cell has a very small value for $\overline{u'w'}$ in the LES, while the maximum value can be found in the ADV-data for this depth level.
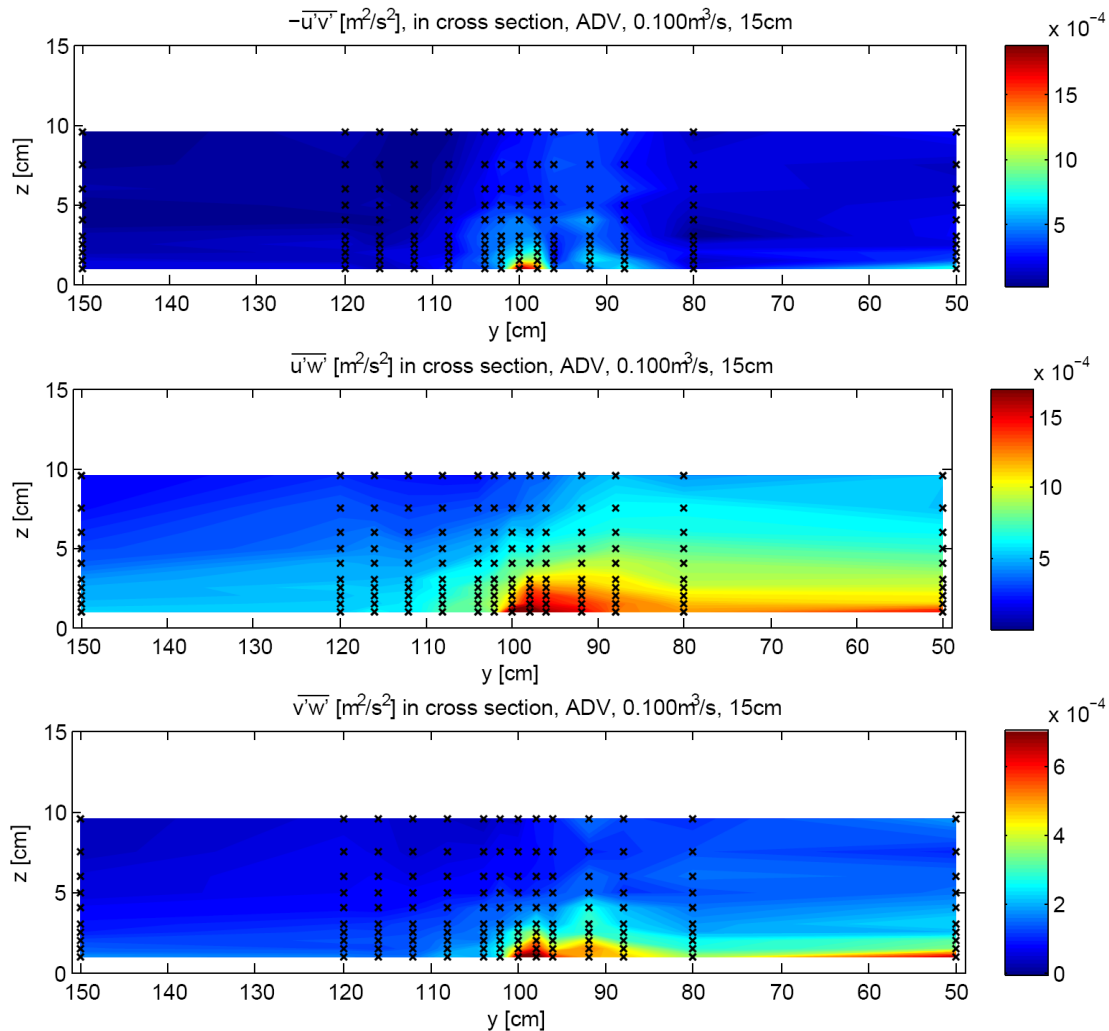

Figure B.1: Covariance terms $\overline{u'\cdot v'}$ (upper panel), $\overline{u'\cdot w'}$ (middle panel) and $\overline{v'\cdot w'}$ (lower panel) deduced from ADV-measurements. Measurement locations are indicated by crosses. Linear interpolation used. Scales are not equal.
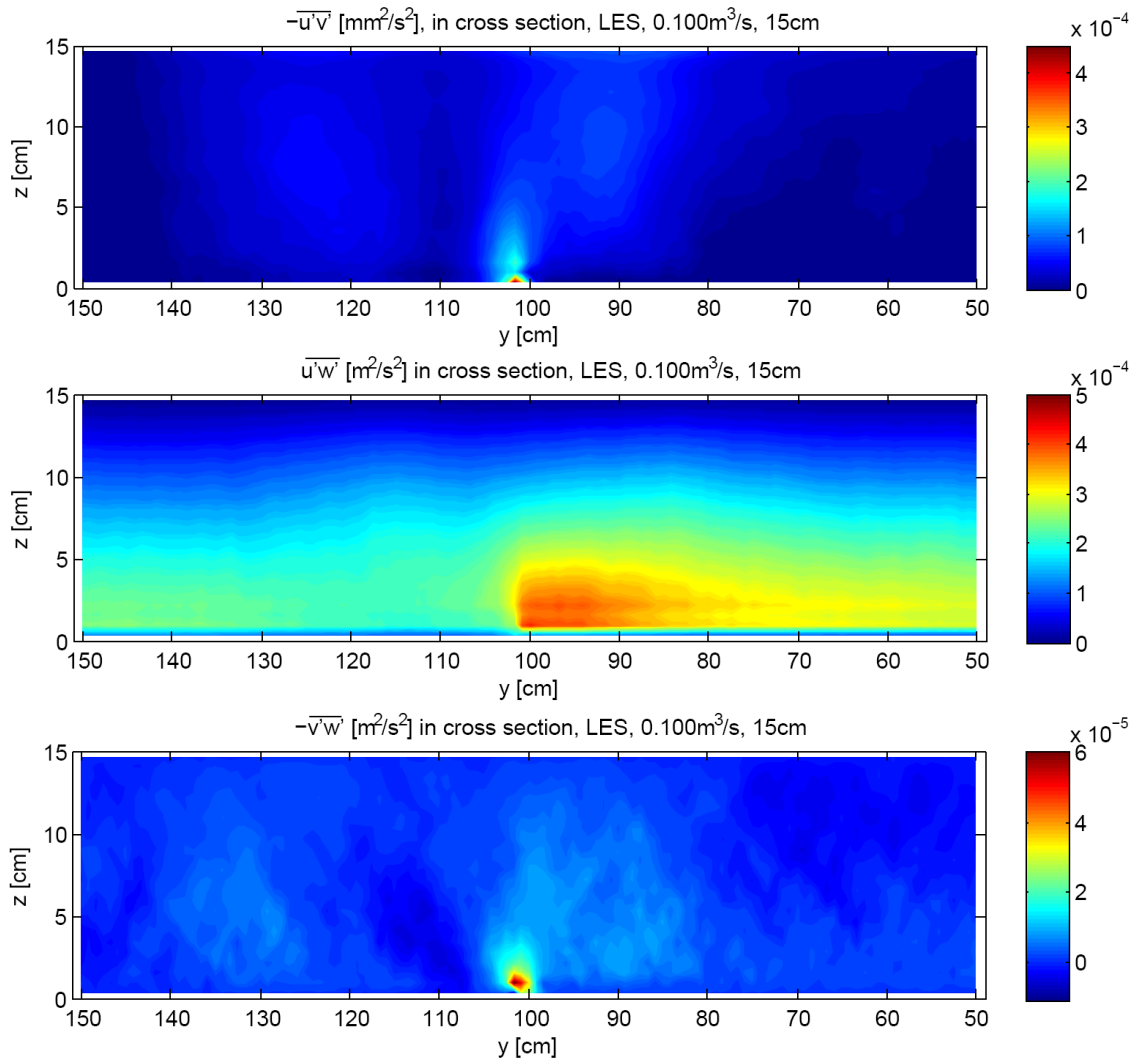
Figure B.2: Covariance terms $\overline{u' \cdot v'}$ (upper panel), $\overline{u' \cdot w'}$ (middle panel) and $\overline{v' \cdot w'}$ (lower panel) deduced from LES-results. Scales are not equal.

To decide whether the discrepancy in magnitude is due to the LES or the ADV-measurements, the local friction coefficients can be compared. Figure B.3 shows these transverse profiles. An overall friction coefficient could be deduced from the roughness height (using the Colebrook equation and $c_f = f/8$). This would lead to values of $c_f = 0.0067$ for the rough side and 0.0027 for the smooth side. The local values derived from the ADV are exceeding these overall values; the LES underestimates the local c_f. A similar discrepancy can be found for the 8cm and 11cm case. From this result can be concluded that the covariance term $\overline{u'w'}$ is measured too high in case of the ADV-measurements and estimated too low in the LES. This suggests that the actual shear stress is in between the values obtained by ADV-measurements and LES-results.

A possible explanation for the too high values in $\overline{u'w'}$ can be an aliasing effect or (non-independent) instrument noise in several velocity components. The noise can indeed be expected non-independent since (especially in a 3-beam solution) the instrument noise in one beam leads to a deviation in several Cartesian velocity components. An analysis on cross-spectra of the velocity data would give certainty of the aliasing effect; this is waived due to the limiting time of this research.
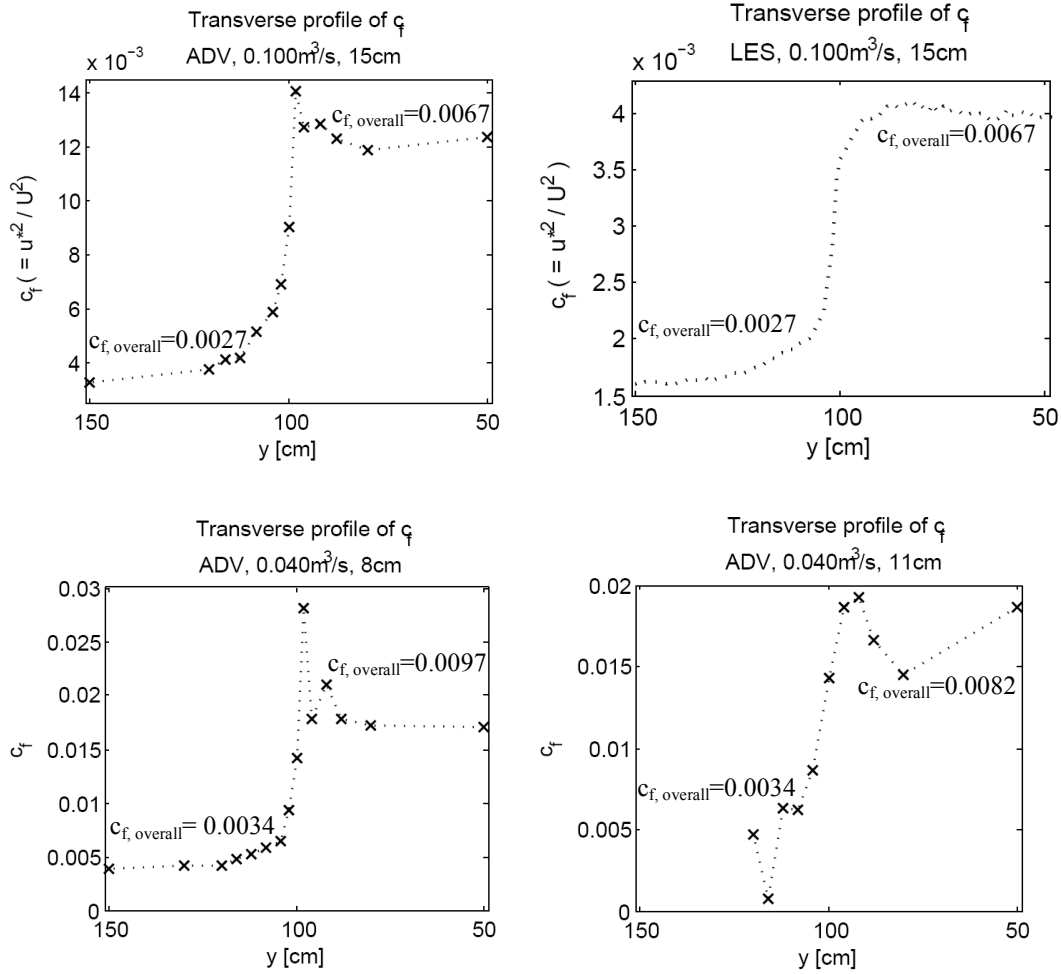

Figure B.3: Transverse profiles of friction coefficient, for ADV-measurements (upper left) and LES-results (upper right). Both derived from data of in the 15cm-case. Lower panels are for the 8cm case (left) and 11cm (right). Overall expected values (based on Colebrook equation) are indicated for all profiles,

To further investigate the origin of the differences between the LES- and ADV-results, the turbulent kinetic energy and turbulent fluctuations for individual components are studied. Figure B.4 shows the turbulent kinetic energy k. The distributions of k show again a similar pattern, but again the turbulent kinetic energy is larger in magnitude (3x) in the ADV-measurements with respect to the LES-results. The difference is some smaller above the smooth bed. It appears from this figure that the magnitude of turbulent fluctuations are

smaller in the LES-results (especially above the rough bed) and thus the correlation between u', v' and w' is similar in case of ADV- and LES-results. This can be understood by realizing that the LES does not include the roughness effects on the turbulent fluctuations (Nezu & Nakagawa, 1991, p.). The effect of roughness on the turbulent fluctuations of individual components is most markedly close to the bottom. This can explain the low value in k and $\overline{u'w'}$ close to the bottom.
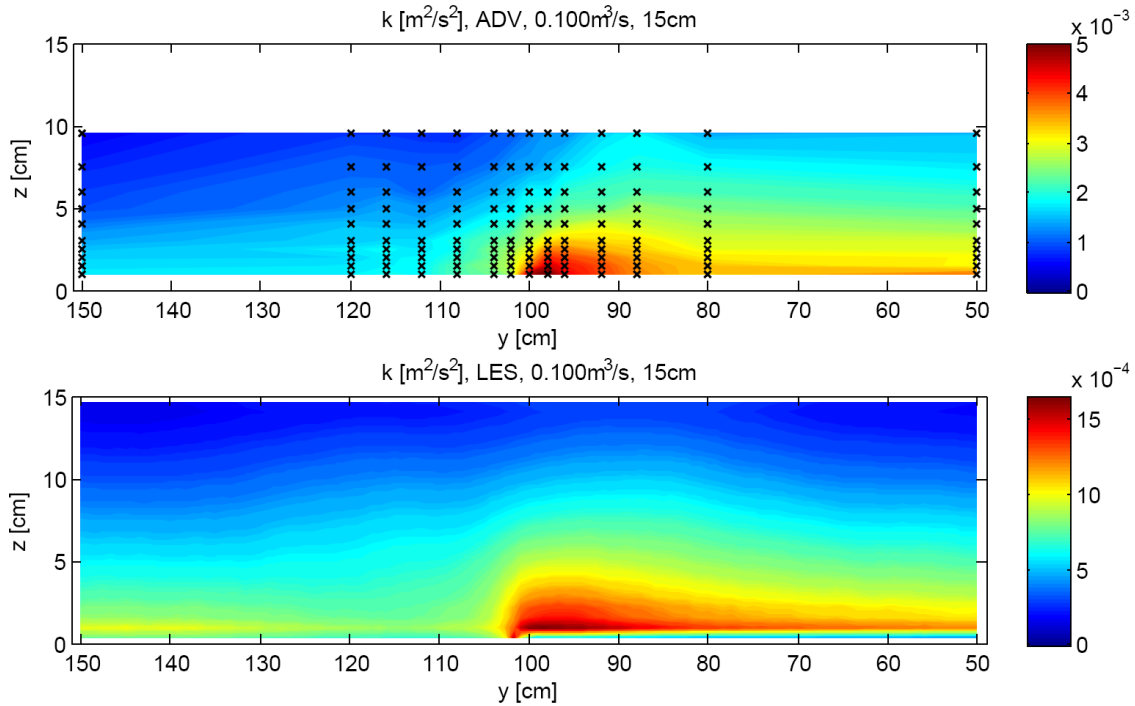

Figure B.4: Turbulent kinetic energy (k) deduced from ADV-measurements (upper panel) and LES (lower panel). Scales are not equal.

A last check to compare the distribution of turbulence quantities is given by figure B.5. These normalized profiles match moderately; in general the normalized turbulent fluctuations are some larger for the LES-results, except at low depth for the transverse and vertical direction. This is in accordance to literature results (Nezu & Nakagawa, 1993). This motivates the hypotheses that the turbulence intensities at the bottom are estimated too small in the LES, causing smaller turbulent stresses and smaller u*, but resulting in a similar distribution as measured by using the ADV. In conclusion, the turbulent shear stresses differ between the LES and ADV results. The ADV seriously overestimates the turbulent shear stresses, the LES underestimates is still a useful tool to understand flow processes, but the stress and turbulence magnitudes are not reliable. An improvement of the boundary condition at the bed in the LES is recommended for a follow-up research.
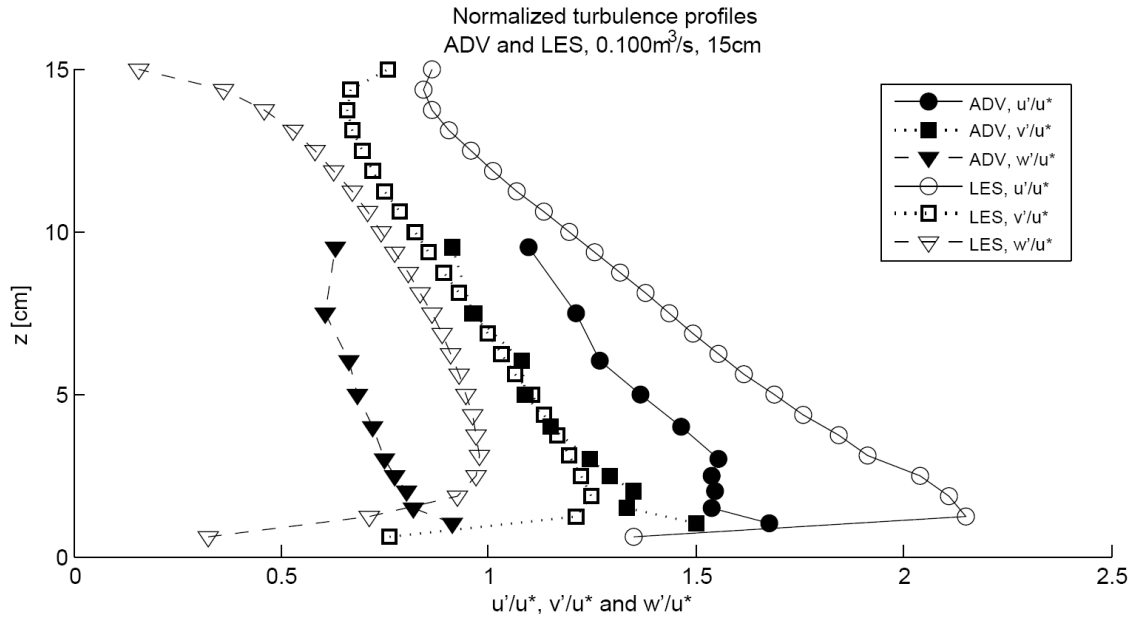
Figure B.5: Turbulent fluctuations of individual components, deduced from ADV-measurements and LES above the rough side (y=50). Profiles are normalized on (local) friction velocity. Profiles at different width coordinates are very similar.

Appendix C: Determination of individual roughness heights

To calculate a theoretical effective friction in a parallel rough flow situation, the roughness parameters for the individual (rough) bed compositions are required. The Darcy friction factor is not convenient for this purpose, since this parameter is dependent on the depth and Reynolds number. The Nikuradse roughness height (k_s) is better applicable, since this parameter is only a property of the bed composition. The derivation of the Nikuradse roughness height for respectively the rough and smooth bed is shown below.

Homogeneous rough case

Measurements over a homogeneous rough bed were done by Jarquín (2007). The bed was covered over the complete width with the same stones used for the parallel cases. In the longitudinal direction, the rough section spanned over 7 meter. The water level slope was calculated only based on the middle part of this rough section, since the edges had a non-linear water level course (figure C.6)
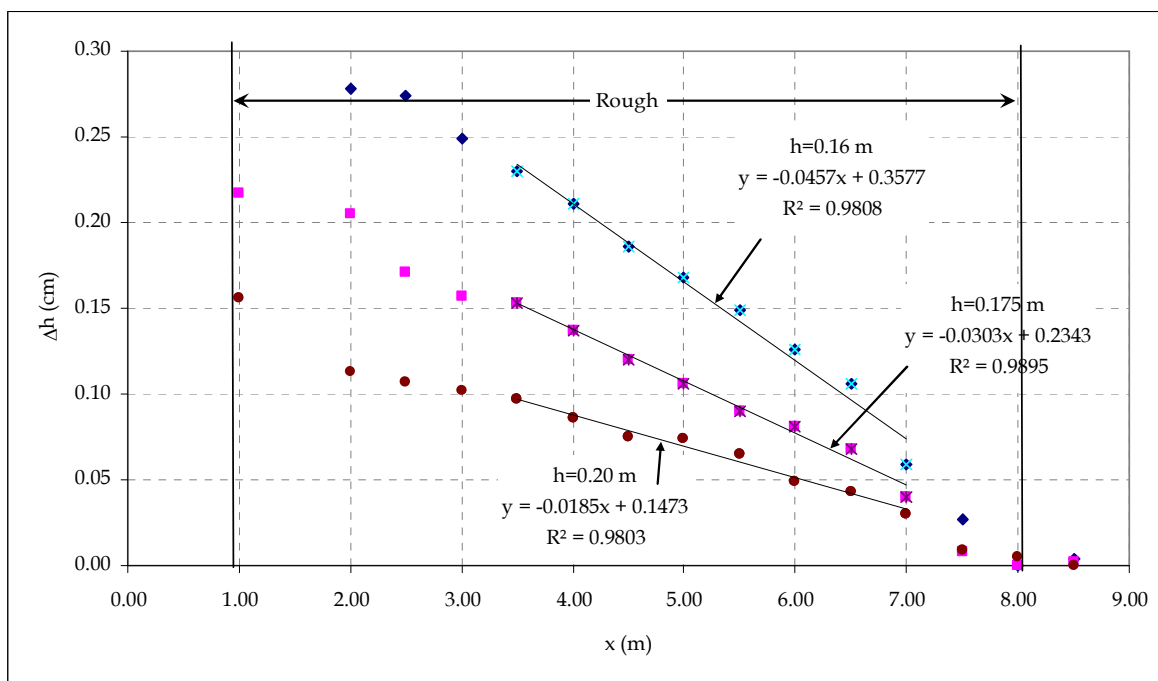

Figure C.6: Water level course for three depth cases, total discharge of 0.120m3/s, measured by electronic gauge. From: Jarquín (2007).

However, Jarquín (2007) neglected the slope in the reference level of the gauge; the moving carriage had a slight slope in longitudinal direction (figure C.7). The magnitude of the change in reference level is larger than 10% of the water level slope itself, so a correction was

actually required. Based on figure C.7, the water level slopes as measured by Jarquin (2007) are increased by 0.00014 m/m.
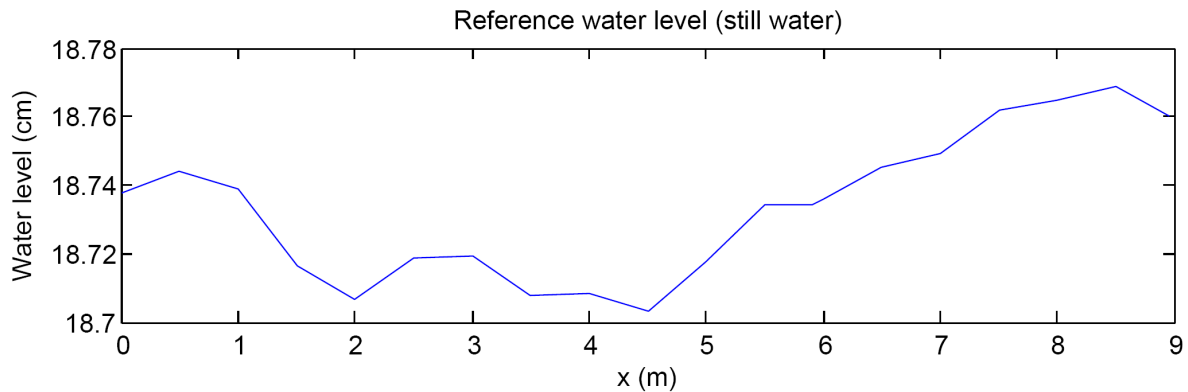

Figure C.7: Reference water level course, based on (almost) still water, twice up and forth, measured by electronic gauge.

Based on the corrected water level slopes, the friction factors could be calculated by using the Darcy-Weisbach formula. Hence, the Nikuradse roughness height can be calculated by using the Colebrook-White formula:

$$\frac{1}{\sqrt{f}} = -c \cdot \log\left(\frac{k_s}{a \cdot R} + \frac{b}{Re\sqrt{f}}\right)$$ (equation C.1)

For the values of the parameters a, b and c, several sets of values are used, listed in table C.1:

Table C.1, parameters values for equation C.1, copied from by McGahey (2006).

Published by:	a	b	c
Colebrook (1937), for pipe flow	14.83	2.52	2.00
Keulegan (1938), for rough beds	12.62	2.98	2.00
Rouse (1946), for wide channels	10.95	1.70	2.03
Graf (1971), for wide channels	12.90	2.77	2.00

The resulting Nikuradse height as function of the hydraulic radius is shown in figure C.8. The Nikuradse height is decreasing with larger hydraulic radius, explained by the higher relative importance of the (smooth) side walls. A trendline for the data using the parameters of Graf (1971) reads the equation:

$$k_s = -0.0733 \cdot R + 0.0209$$ (equation C.2)

This relation between k_s and R was used for a calculation of the theoretical effective friction factor. This result compares well with the Nikuradse height that was based on the stone diameter (k_s = 19 mm based on 2·d_{90}).
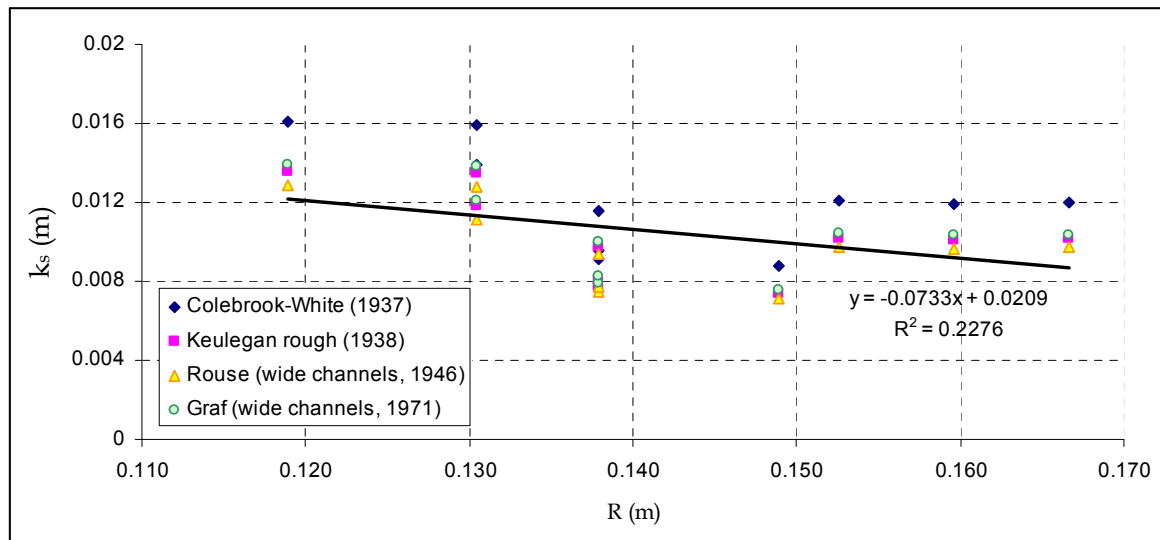

Figure C.8: Nikuradse roughness height for a homogeneous rough bed as function of hydraulic radius. Water level slopes measured by Jarquin (2007), and treated as explained in text.

Homogeneous smooth case

A hydraulically smooth wall should obey the same Colebrook-White formula with a value for k_s=0. This could be validated by water level slope measurements. In contrast to the rough case, there was no homogeneous smooth case to validate this assumption. The longest section that could be used for determining the Nikuradse roughness height for the smooth bed was prior to configuration 1a (used to investigate the developing parallel flow). In this case, the bed was smooth for 6.5 meter in front of the smooth-rough split (see figure 4 of main report). The difference between the gauges at x=-5.3 and x=-1.5 could be used to calculate the water level slope and hence the corresponding Nikuradse roughness height.

However measurement errors seems to have a large influence in this case (since the water level slopes over this smooth part were very small and only two measurement points were possible), the results are scattered around k_s=0 with an outlier for the 22cm case. The water level measurements in this 22cm case have relatively the largest errors of all cases, so this outlier is held to be a measurement error. In conclusion, these measurement give no reason to reject the assumption of k_s=0 for the smooth section.
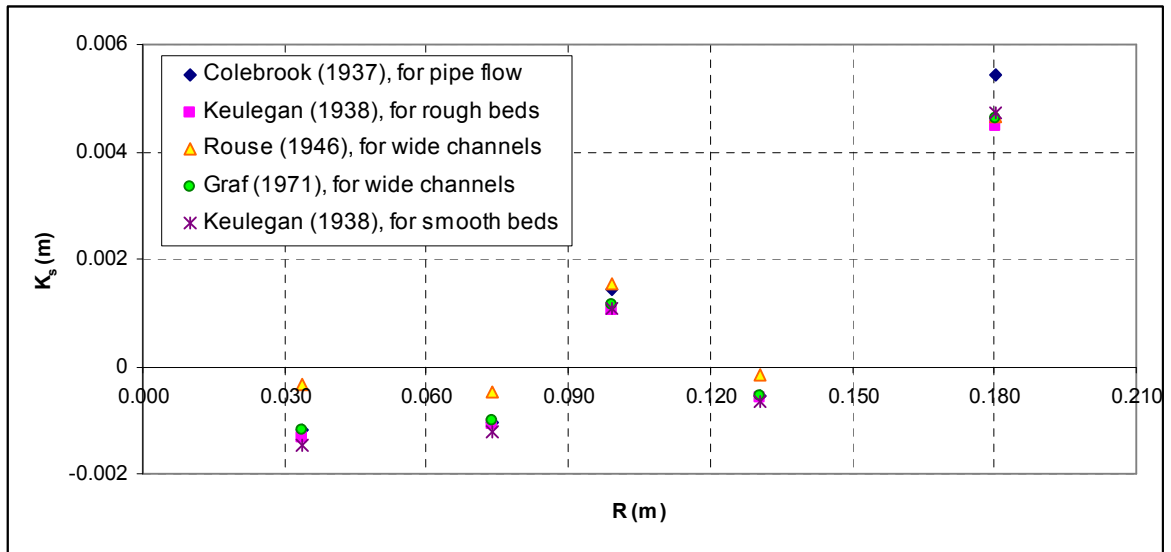
Figure C.9: Nikuradse roughness height for a homogeneous smooth bed as function of the hydraulic radius. Water level slopes measured in from of configuration 1a.

Appendix D: Momentum changes due to depth averaged mass transport

A depth-averaged transverse mass transport brings momentum as well as mass from one to another side. The transverse mass transport causes acceleration of the (depth-averaged) flow on one side and deceleration of the flow on the other side of the flume. Therefore not only the velocities at the interface must be studied, but an approach with considering a control volume is required.
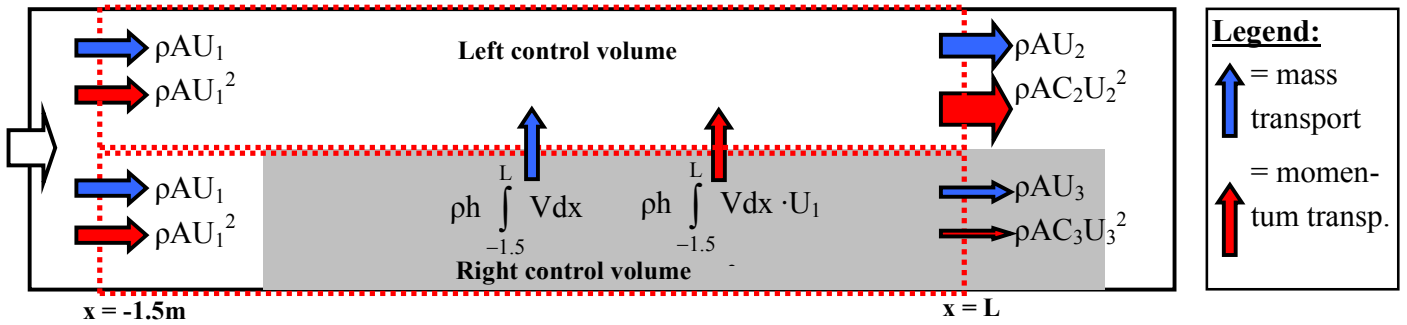

Figure D.1: Definition of two control volumes in top view. The corresponding mass and momentum fluxes are assigned.

Figure D.1 shows the control volumes that were defined in the main text. The value for the (depth- and width-averaged) velocity u_1 is accurately known, since this equals the discharge divided by the cross sectional area. The values for U_2 and U_3 are less well known, since the velocity profiles next to the side walls are relatively unknown. The transverse velocity is monitored in a denser grid, which enables us to calculate the (depth- and width-averaged) U_2 and U_3 based on the transverse velocity and a mass balance. This mass balance reads:

$$A_{\text{left}} \cdot U_2 = A_{\text{left}} \cdot U_1 + h \cdot \int_{-\infty}^{L} V dx \qquad \text{(equation D.1)}$$

$$A_{\text{right}} \cdot U_3 = A_{\text{right}} \cdot U_1 - h \cdot \int_{-\infty}^{L} V dx \qquad \text{(equation D.2)}$$

in which

> L is the x-coordinate of the downstream end of the control volume.

> A_{left} and A_{right} are the cross-sectional areas of the left and right control volume (=b·h)

The net transverse velocity is zero in a uniform flow, which is the case at a large distance of the roughness split. At x=-1.5, the transverse flow was close to zero. Therefore, the integrals in equation D.1 and D.2 can be started from x=1.5m in stead of -∞. Then the measured profile of V in x-direction can be used to calculate u_2 and u_3.

Initially, consider a situation in which the velocity profiles U_1, U_2 and U_3 are uniform. The momentum advected by the water can simply be calculated by the mass times the velocity. This results for the left control volume in:

$$M_{left,in} = \rho \cdot A \cdot U_1 \cdot U_1 + \rho \cdot h \int\limits_{-1.5}^{L} Vdx \cdot U_1 \qquad \text{(equation D.3)}$$

$$M_{left,out} = \rho \cdot A \cdot U_2 \cdot U_2 = \rho \cdot b \cdot h \cdot \left(U_1 + \frac{1}{b} \int\limits_{-1.5}^{L} Vdx \right)^2 \qquad \text{(equation D.4)}$$

in which b is the width of one control volume (i.e. 1 meter).

Note that the transverse momentum flux (last term in equation D.3) makes use of the velocity U_1 since the longitudinal velocity at the interface is approximately equal to the average velocity U_1. The last equation can be rewritten by normalizing the function for V: $V(x) = U_1 \cdot \widetilde{V}(x)$, in which $\widetilde{V}(x)$ is a normalized function for V as is shown in figure 38 of the main text, copied in figure D.2.
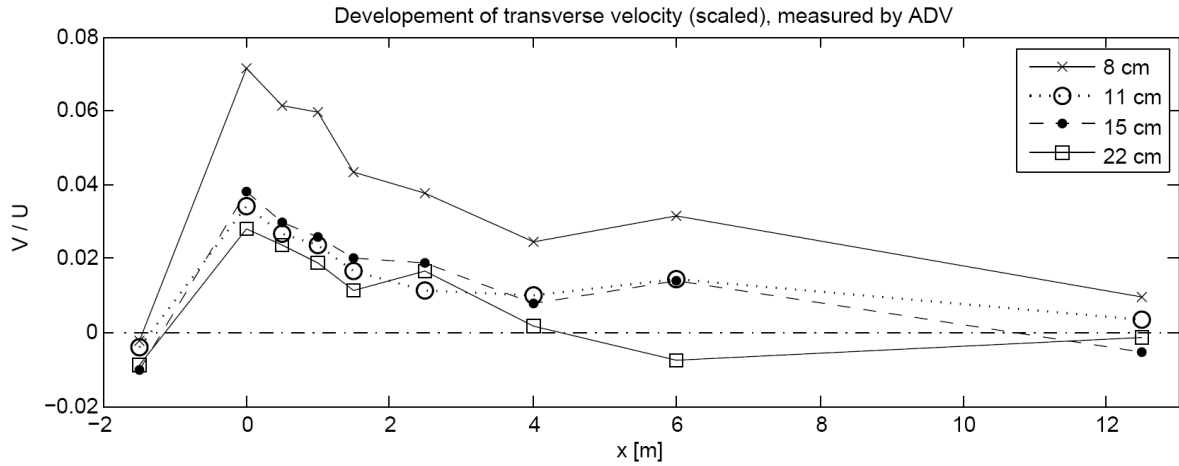

Figure D.2: Depth averaged transverse velocity (V) at y=100cm, normalised on the average longitudinal velocity (U_1)

The change in advected momentum for the left control volume can now be written as:

$$\Delta M_{left} = \rho \cdot h \cdot U_1^2 \left(b + \int\limits_{-1.5}^{L} \widetilde{V}dx \right) - \rho \cdot b \cdot h \cdot U_1^2 \left(1 + \frac{1}{b} \int\limits_{-1.5}^{L} \widetilde{V}dx \right)^2$$

$$= \rho \cdot b \cdot h \cdot U_1^2 \left(K - K^2 \right) \qquad \text{(equation D.5)}$$

in which

$$K = 1 + \frac{1}{b} \int\limits_{-1.5}^{L} \widetilde{V}dx \qquad \text{(equation D.6)}$$

A similar derivation can be made for the right control, resulting in:

$$\Delta M_{right} = \rho \cdot b \cdot h \cdot U_1^2 \cdot \left(N - N^2 \right)$$
(equation D.7)

in which

$$N = 1 - \frac{1}{b} \int_{-1.5}^{L} \widetilde{V} dx$$
(equation D.8)

Since K>1 and N<1, it follows that ΔM_{left} < 0 and ΔM_{right} > 0. Therefore the pressure gradients are increased at the left side and reduced at the right side by this effect. However, these quantities are not exactly compensating each other. The total change in advected momentum equals:

$$\Delta M_{damt} = \rho \cdot b \cdot h \cdot U_1^2 \cdot \left(K - K^2 + N - N^2 \right)$$

$$= \rho \cdot b \cdot h \cdot U_1^2 \cdot \left(1 + I_v - 1 - \left(I_v \right)^2 - 2I_v + 1 - I_v - 1 - \left(I_v \right)^2 + 2I_v \right)$$

$$= -2\rho \cdot b \cdot h \cdot U_1^2 \cdot I_v^2$$
(equation D.9)

in which

$$I_v = \frac{1}{b} \int_{-1.5}^{L} \widetilde{V} dx$$
(equation D.10)

The depth dependency is not evident since I_v appeared to be larger in smaller depth cases (due to the higher relative roughness, shown in the main text). The dependency on the transverse velocity (note: $U_1^2 \cdot I_v^2 = \frac{1}{b^2} \int V^2 dx$) is undisputed. This underlines the importance of accurate (transverse) velocity measurements.

For the contribution on the pressure gradient, the change advected momentum per unit area must be analyzed, i.e. the gradient of equation D.9. The derivative of equation D.9 to x (and using in b=1) reads:

$$T_{damt} = \frac{\partial \left(-2\rho \cdot h \cdot U_1^2 \cdot I_v^2 \right)}{\partial x} = -2\rho \cdot h \cdot U_1^2 \cdot \frac{\partial \left(I_v^2 \right)}{\partial x} = -4\rho \cdot h \cdot U_1^2 \cdot \widetilde{V} \cdot I_v$$

$$= -4\rho \cdot h \cdot U_1^2 \cdot \widetilde{V} \cdot \int_{-1.5}^{L} \widetilde{V} dx$$
(equation D.11)

This clearly shows that transverse mass transport at the end of the undeveloped region causes much more momentum deficit than an equal mass transport at the start of the transition (due

to the integral part). This can be understood by realising that the momentum flux is dependent on the longitudinal velocity squared; for example an increase in U from 0.2 to 0.3 m/s creates less change in momentum than an increase from 0.3 to 0.4 m/s.

An important assumption for this derivation was that the velocity fields U_1, U_2 and U_3 are individually uniform. This is not the case for three reasons:
- bottom friction leads to a vertical changing velocity
- side wall friction leads to a boundary layer close to the side walls
- a distinct velocity above the rough and the smooth side creates a mixing layer with a gradually changing velocity profile

The first and second effect occur before the influence of the parallel rough bottom as well as in the developed flow. Although these effects might cause a change in advected momentum (due to the changing bottom roughness and velocity magnitudes), the changes for the momentum are expected to be minor compared to ΔM_{damt}. The last effect only occurs at the (partly) developed flow. Therefore a correction must be applied to account for the non-uniformity of the velocity in the mixing layer. That can be done by normalising U_2 and U_3 to its average values, i.e. $U_2(x) = \overline{U_2} \cdot \widetilde{U}_2(x)$ and $U_3(x) = \overline{U_3} \cdot \widetilde{U}_3(x)$, in which $\widetilde{U}_2(x)$ and $\widetilde{U}_3(x)$ are dimensionless velocity profiles with an average value of 1. Now, the average value for the velocity squared can be given by:

$$\overline{U_2^2} = \overline{U_2}^2 \cdot \overline{\widetilde{U}_2^2} = \overline{U_2}^2 \cdot C_2 \qquad \text{(equation D.12)}$$

$$\overline{U_3^2} = \overline{U_3}^2 \cdot \overline{\widetilde{U}_3^2} = \overline{U_3}^2 \cdot C_3 \qquad \text{(equation D.13)}$$

The parameters C_2 and C_3 are slightly larger than 1 since the average values of $\widetilde{U}_2(x)$ and $\widetilde{U}_3(x)$ are by definition exactly 1 (and every non-uniformity gives an increase for the average squared value). Measured data from the developed situation (x=12.5m) reveal that $C_2 \approx 1.01$ and $C_3 \approx 1.001$. C_2 is larger than C_3 since the mixing layer is wider above the smooth side than above the rough side. Finally, the momentum change and its gradients can be written by:

$$\Delta M_{damt} = \rho \cdot h \cdot \overline{U_1}^2 \cdot \left(2 - C_2 \cdot (1 + I_v)^2 - C_3 \cdot (1 - I_v)^2\right) \qquad \text{(equation D.14)}$$

$$T_{damt,left} = -2\rho \cdot h \cdot \overline{U_1}^2 \cdot \widetilde{V} \cdot \left(C_2 - \frac{1}{2} + C_2 \int_{-1.5}^{L} \widetilde{V} dx\right) \qquad \text{(equation D.15)}$$

$$T_{damt,right} = -2\rho \cdot h \cdot \overline{U_1}^2 \cdot \widetilde{V} \cdot \left(-C_3 + \frac{1}{2} + C_3 \int_{-1.5}^{L} \widetilde{V} dx\right) \qquad \text{(equation D.16)}$$

$$T_{damt} = 2\rho \cdot h \cdot \overline{U_1}^2 \cdot \tilde{V} \cdot \left(C_3 - C_2 - (C_2 + C_3) \cdot \int_{-1.5}^{L} \tilde{V}dx \right) \qquad \text{(equation D.17)}$$

Applying the measured transverse velocities, the profiles of T_{damt} along the x-coordinate can be calculated. Figure D.3 and D.4 shows the result.
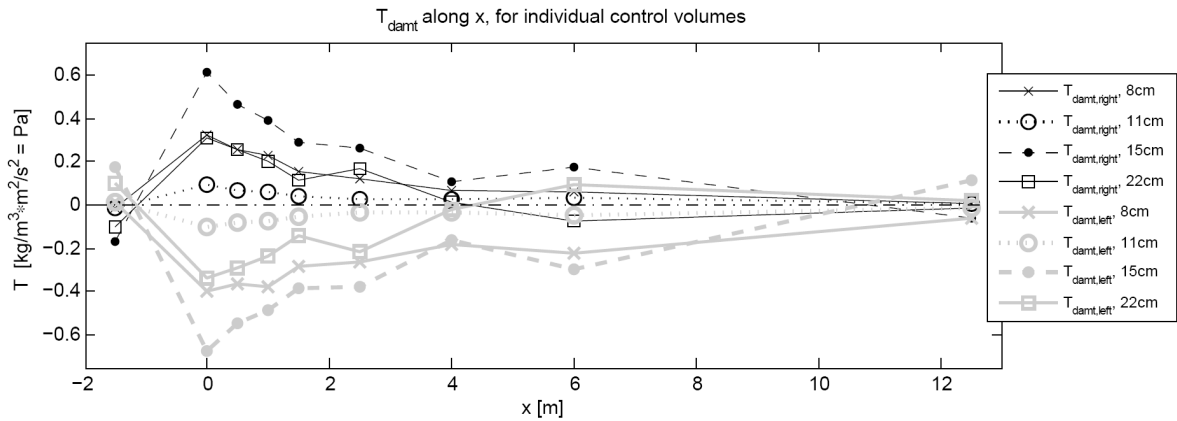

Figure D.3: T_{damt} for individual (left and right) control volumes against x, based on measured transverse velocities applying equations D.15 and D.16
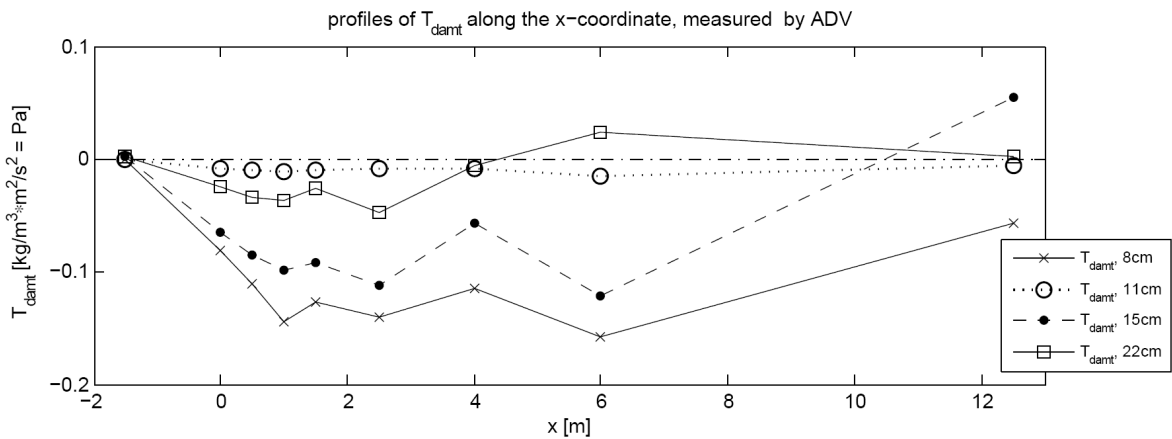

Figure D.4: T_{damt} against x, based on measured transverse velocities applying equations D.17. This result can be derived by summing the graphs of the individual control volume (figure D.3)